

UC Davis

UC Davis Previously Published Works

Title

A Night-Time Edge Site Intermediate in the Cyanobacterial Circadian Clock Identified by EPR Spectroscopy

Permalink

<https://escholarship.org/uc/item/3qh0q56c>

Journal

Journal of the American Chemical Society, 144(1)

ISSN

0002-7863

Authors

Chow, Gary K

Chavan, Archana G

Heisler, Joel

et al.

Publication Date

2022-01-12

DOI

10.1021/jacs.1c08103

Peer reviewed

# A Night-Time Edge Site Intermediate in the Cyanobacterial Circadian Clock Identified by EPR Spectroscopy

Gary K. Chow, Archana G. Chavan, Joel Heisler, Yong-Gang Chang, Ning Zhang, Andy LiWang,\* and R. David Britt\*



Cite This: *J. Am. Chem. Soc.* 2022, 144, 184–194



Read Online

ACCESS |



Metrics & More

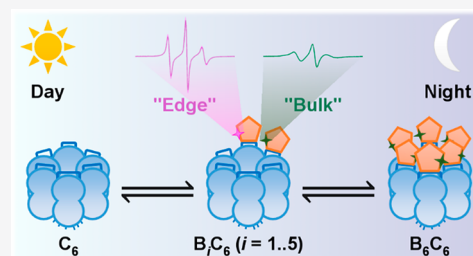


Article Recommendations



Supporting Information

**ABSTRACT:** As the only circadian oscillator that can be reconstituted *in vitro* with its constituent proteins KaiA, KaiB, and KaiC using ATP as an energy source, the cyanobacterial circadian oscillator serves as a model system for detailed mechanistic studies of day–night transitions of circadian clocks in general. The day-to-night transition occurs when KaiB forms a night-time complex with KaiC to sequester KaiA, the latter of which interacts with KaiC during the day to promote KaiC autophosphorylation. However, how KaiB forms the complex with KaiC remains poorly understood, despite the available structures of KaiB bound to hexameric KaiC. It has been postulated that KaiB–KaiC binding is regulated by inter-KaiB cooperativity. Here, using spin labeling continuous-wave electron paramagnetic resonance spectroscopy, we identified and quantified two subpopulations of KaiC-bound KaiB, corresponding to the “bulk” and “edge” KaiBC sites in stoichiometric and substoichiometric KaiB<sub>*i*</sub>C<sub>6</sub> complexes (*i* = 1–5). We provide kinetic evidence to support the intermediacy of the “edge” KaiBC sites as bridges and nucleation sites between free KaiB and the “bulk” KaiBC sites. Furthermore, we show that the relative abundance of “edge” and “bulk” sites is dependent on both KaiC phosphostate and KaiA, supporting the notion of phosphorylation-state controlled inter-KaiB cooperativity. Finally, we demonstrate that the interconversion between the two subpopulations of KaiC-bound KaiB is intimately linked to the KaiC phosphorylation cycle. These findings enrich our mechanistic understanding of the cyanobacterial clock and demonstrate the utility of EPR in elucidating circadian clock mechanisms.



## INTRODUCTION

Circadian clocks are endogenous biochemical oscillators that align diverse organisms' physiology with periodic day–night cycles,<sup>1</sup> thereby improving their survivability.<sup>2</sup> To study the molecular mechanisms governing circadian clocks, we turned to the cyanobacterial clock expressed by *Synechococcus elongatus* (PCC 7942) as its oscillator is entirely post-translational and can be reconstituted *in vitro*<sup>3</sup> in the absence of transcription or translation.<sup>4</sup> The circadian oscillator in *S. elongatus* consists of three proteins, KaiA, KaiB, and KaiC (Figure 1a), that when combined with ATP, generate a circadian rhythm in serine 431 (S431) and threonine 432 (T432) phosphorylations in KaiC via the cyclic sequence S;T → S;pT → pS;pT → pS;T → S;T → ... (p: phosphorylated)<sup>5,6</sup> (Figure 1a). During the day, KaiA acts as a nucleotide exchange factor of KaiC<sup>7,8</sup> by binding KaiC at the C-terminal loop region (A-loops)<sup>9</sup> and facilitating KaiC autokinase activity. At night, S431 phosphorylation in KaiC leads to changes in the flexibility of the C-terminal domain of KaiC (CII) and subsequent CII–CI ring–ring stacking (CI, N-terminal domain of KaiC).<sup>10,11</sup> This stacking interaction, along with ADP binding in CI enabled by CI ATPase activity,<sup>12,13</sup> biases KaiC toward an alternative conformation that is KaiB-binding competent<sup>10,14</sup> at the loop region of the N-terminal

domain (B-loops).<sup>15</sup> This KaiB-binding competent KaiC state stabilizes a fold-switched conformer of KaiB (fs-KaiB)<sup>16</sup> that is capable of sequestering KaiA into a ternary KaiABC complex.<sup>10,17</sup> The fs-KaiB-bound KaiA adopts an autoinhibited conformation that is incapable of binding to the KaiC A-loops,<sup>17</sup> thus inhibiting KaiC autokinase activity and allowing the autophosphatase activity to dominate. The oscillator returns to the dawn state once hyperphosphorylated KaiC dephosphorylates and KaiA and KaiB are released from KaiABC complexes.

The KaiB–KaiC binding event is key to closing the negative feedback loop<sup>13</sup> to the rhythmic oscillation of the Kai system by deactivating KaiA.<sup>17</sup> Furthermore, KaiB provides temporal regulation of the phosphorylation levels of RpaA, the master transcription regulator,<sup>18</sup> through two cognate histidine kinases, SasA<sup>19</sup> and CikA<sup>20</sup> (Figure 1b). At dusk, SasA is activated on binding to KaiC<sub>pSpT</sub> and autophosphorylates at

Received: August 3, 2021

Published: January 3, 2022



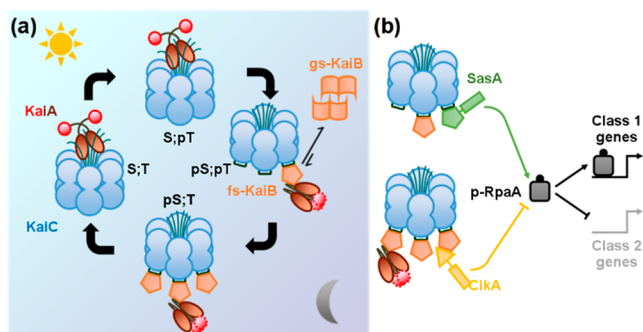


**Figure 1.** Model of the cyanobacterial circadian clock (Kai clock). (a) Interactions among the three core proteins, KaiA (red/brown), KaiB (orange), and KaiC (cyan) as represented by their cartoon depictions. The phosphostate of the KaiC phosphosites, serine 431 (S431) and threonine 432 (T432), cycles through the sequence S;T → S<sub>p</sub>T → pS;pT → pS;T → S;T (p: phosphorylated). gs-KaiB and fs-KaiB represent the ground state and fold-switched state of KaiB, respectively. (b) Coupling of the core proteins with SasA (green) and CikA (yellow) to regulate RpaA phosphorylation (phosphorylated RpaA: p-RpaA), which in turn upregulates class 1 genes and downregulates class 2 genes.

SasA-H161,<sup>21</sup> followed by phosphotransfer to aspartyl residue 53 of RpaA and upregulation of class 1 (dusk-peaking) gene expression.<sup>18</sup> As the night progresses, KaiB-KaiC interactions replace that of SasA-KaiC as KaiC<sub>pS;pT</sub> dephosphorylates to KaiC<sub>pS;T</sub>, deactivating SasA. Concurrent to sequestration of KaiA, KaiC-bound KaiB recruits CikA and activates its phosphatase activity toward RpaA.<sup>20</sup> At dawn, KaiB-KaiC complexes dissociate on KaiC<sub>pS;T</sub> dephosphorylation to KaiC<sub>S;T</sub>, releasing KaiB-associated CikA (and KaiA) and completing an RpaA activation–deactivation cycle. On the structural level, although the N-terminal domains of SasA and KaiB share the KaiC B-loops as their binding sites,<sup>15,16</sup> their differential temporal associations with KaiC gate RpaA activation via (i) the faster SasA-KaiC<sub>pS;pT</sub> versus KaiB-KaiC<sub>pS;pT</sub> binding kinetics due to KaiB fold-switching<sup>16</sup> and (ii) SasA-facilitated KaiB-KaiC<sub>pS;pT</sub> binding as a result of heterotropic cooperativity.<sup>22</sup> Conversely, the gating of RpaA deactivation is accomplished via cooperative CikA-KaiB-KaiC binding, with the β2 motif of fs-KaiB<sup>17</sup> (Figure 1b) capable of binding to either CikA or KaiA. This competition underlies the observations that CikA shortens oscillation period<sup>16</sup> and compensates for low levels of KaiA.<sup>22,23</sup> Given the pivotal role of KaiB-KaiC binding-dissociation to clock input and output, understanding the regulation of KaiB-KaiC binding at the molecular level is of prime interest to elucidating cyanobacterial circadian rhythms in general.

It has been postulated that inter-KaiB cooperativity is fundamental to regulating KaiB-KaiC binding.<sup>17,24,25</sup> Previous native mass spectrometry only detected KaiC<sub>6</sub>, B<sub>1</sub>C<sub>6</sub>, and B<sub>6</sub>C<sub>6</sub>,<sup>24</sup> hinting at cooperativity while leaving open the question of existence of other stepwise B<sub>i</sub>C<sub>6</sub> intermediates,  $i = 2, 3, 4, \text{ or } 5$ . More recently, crystal structures of the KaiB-KaiC complex revealed that the KaiB-KaiB interface contains a salt bridge between individual KaiB protomers facilitated by R22,<sup>17</sup> a residue that when mutated to alanine in the *Anabaena* analogue weakened KaiB-KaiC interactions.<sup>26</sup> However, questions remain as to the importance of cooperativity from a kinetic standpoint as well as the strength of contributions from nearby charged residues that were not well resolved in either crystal or cryo-EM structures.<sup>17,27</sup> In this study, we

investigate the role of cooperativity in KaiB-KaiC binding by site-directed spin labeling (SDSL) of KaiB at K25. We show that KaiB-KaiC binding is a multistep process, resulting in two spectroscopically distinct populations of KaiC-bound KaiB. One population corresponds to KaiC-bound KaiB that has an adjacent KaiB on its α1 interface (“bulk sites”, B<sub>+</sub>), whereas the other corresponds to KaiC-bound KaiB with adjacent KaiC sites unoccupied (“edge sites”, B<sub>-</sub>). We demonstrate that edge sites are intermediate states capable of recruiting KaiB for cooperative KaiB-KaiC binding, thereby reducing edge and increasing bulk sites, and that antagonization of KaiB-KaiC interactions increases edge and decreases bulk sites. We further show that the bulk ⇌ edge equilibrium is tuned via KaiC phosphorylation status and KaiA. The implications of these results are discussed in the context of the full oscillator.

## RESULTS

**Spin Labeling Reveals Two Subpopulations of KaiC-Bound KaiB.** Wild-type KaiB does not possess native cysteines and is therefore amenable to site-directed mutagenesis to cysteine followed by spin labeling. To investigate inter-KaiB cooperativity, we spin-labeled KaiB at K25, a residue that is solvent exposed in tetrameric ground-state KaiB (gs-KaiB, Figure 2a)<sup>28</sup> but contributes to the KaiB-KaiB interface in KaiB<sub>6</sub>C<sub>6</sub> (Figure 2b),<sup>17,27</sup> to give KaiB-K25C-3IAP (K25C<sub>3IAP</sub> hereafter; 3IAP: 3-iodoacetamido-PROXYL). K25C<sub>3IAP</sub> was determined to be fully labeled by intact mass spectrometry (Figure S1), and it served as a functional surrogate of WT-KaiB for the reconstitution of the *in vitro* KaiABC oscillator and for the binding kinetics of KaiC-KaiB, as indicated by fluorescence anisotropy (Figure S2) and native-PAGE (Figure S3), respectively.

The continuous-wave electron paramagnetic resonance (cw-EPR) spectrum of K25C<sub>3IAP</sub> alone displayed at least two motional dynamics states and could be simulated as such (Figures 2c and S4). Both motional components possessed isotropic rotational correlation times (Table S1) faster than twice the predicted value derived from the Stokes–Einstein relation,<sup>29,30</sup> suggesting that the observed motions are due to local dynamics. Plausible explanations to multiple nitroxide motional components with differing mobilities at a single labeling site include intrahelical interactions<sup>31</sup> and diastereomeric spectroscopic resolution.<sup>32</sup>

K25C<sub>3IAP</sub> responded spectroscopically to KaiC<sub>S431E,T432E</sub> (KaiC<sub>EE</sub>), a phosphomimetic that mimics the dusk state (Figure 2c), suggesting local environment perturbation around the nitroxide moiety on binding KaiC<sub>EE</sub>. Curiously, stoichiometric KaiC<sub>EE</sub> (as monomer:monomer ratio) resulted in a decrease in  $h_0$  transition intensity (~329 mT), whereas its intensity was partly restored with excess KaiC<sub>EE</sub> (Figure 2c). Further analysis revealed that the spectra of free K25C<sub>3IAP</sub>, with stoichiometric or 10-fold KaiC<sub>EE</sub>, were linearly independent (Figure S5). Such linear independence behavior was not observed when KaiC<sub>EE</sub> was substituted with a monomeric KaiCI construct (Figure S6)<sup>10</sup> or in our previous work with N19C<sub>3IAP</sub>.<sup>29</sup> The formation of nonequivalent spectra upon adding differing ratios of KaiC<sub>EE</sub> to K25C<sub>3IAP</sub> implies the formation of KaiBC<sub>EE</sub> complexes of differing stoichiometries and the existence of substoichiometric KaiB<sub>i</sub>C<sub>6</sub>,  $i < 6$ . This conclusion is qualitatively consistent with previous native mass spectrometric results which suggested that KaiB could bind to KaiC as B<sub>1</sub>C<sub>6</sub> or B<sub>6</sub>C<sub>6</sub> complexes,<sup>24</sup> with stoichiometric KaiC<sub>EE</sub> favoring B<sub>6</sub>C<sub>6</sub>, whereas excess KaiC<sub>EE</sub> favoring B<sub>1</sub>C<sub>6</sub> instead.

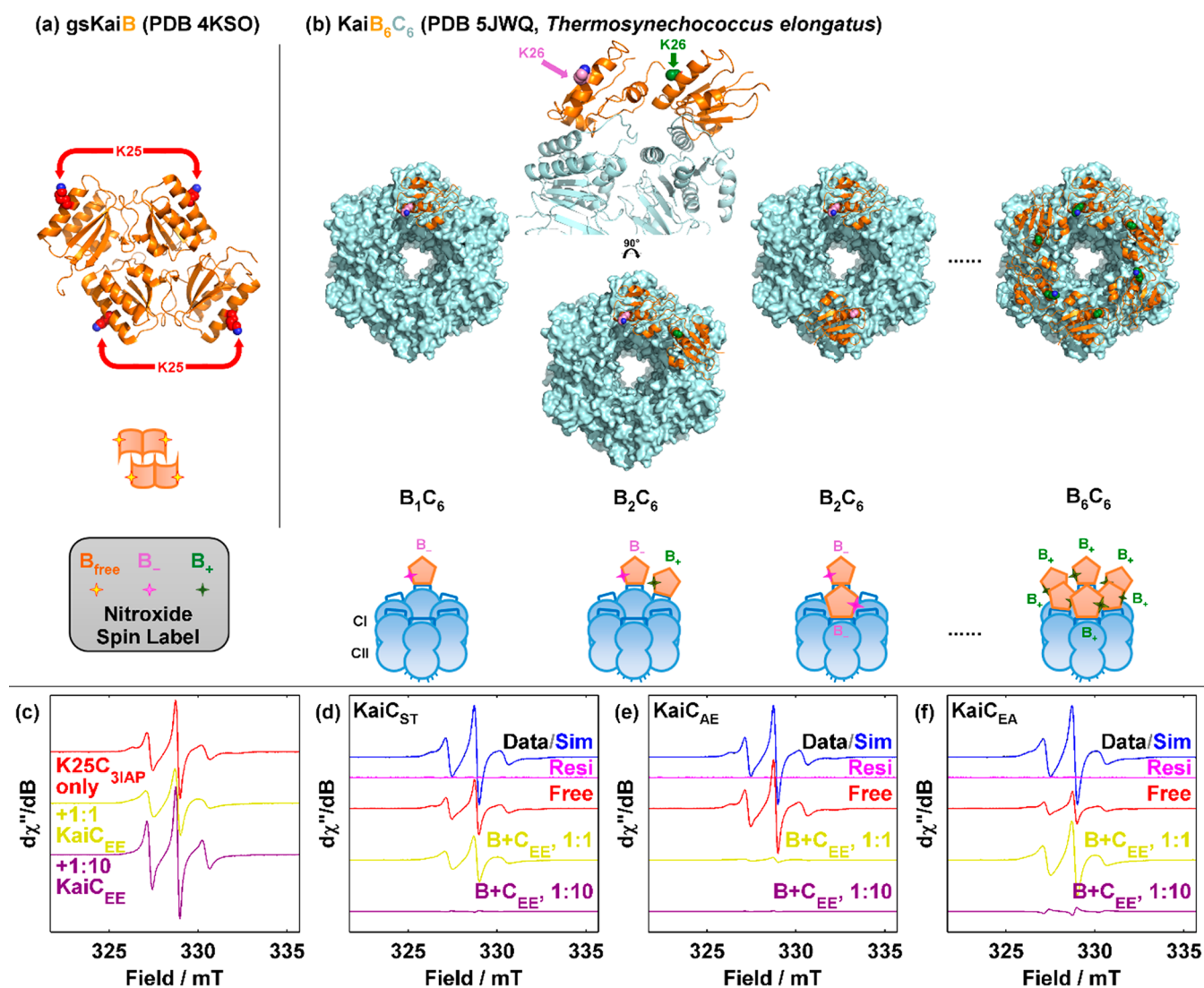


**Figure 2.** Site design for probing the role of cooperativity in the Kai oscillator. (a) Free KaiB (bright orange) with the side chain of labeling position K25C<sub>3IAP</sub> shown in red. (b) KaiB<sub>6</sub>C<sub>6</sub> and presumed substoichiometric KaiBC intermediates prior to KaiB<sub>6</sub>C<sub>6</sub> formation. KaiC is shown as a light blue surface. The two types of KaiBC sites, “bulk” (B<sub>+</sub>) and “edge” (B<sub>-</sub>), are shown in green and light purple, respectively. Part of the side chain in chain B, K26 of the crystal structure of KaiB<sub>6</sub>C<sub>6</sub>, is missing. For (a) and (b), the side chain atoms of K25 (K26 in *T. elongatus*) are shown as spheres with lysyl nitrogen atoms shown in blue. Cartoon models are shown along the bottom. Bottom left box shows legend for spin labels and their corresponding spectroscopic classification. (c) Comparison of spectra of K25C<sub>3IAP</sub> alone (red) versus incubation with stoichiometric (dark yellow) and 10-fold excess (purple) KaiC<sub>EE</sub>. (d–f) Reproduction of K25C<sub>3IAP</sub>-KaiC<sub>ST</sub> (d), KaiC<sub>AE</sub> (e), and KaiC<sub>EA</sub> (f) reaction spectra (black) using a linear combination of free K25C<sub>3IAP</sub> and K25C<sub>3IAP</sub>-KaiC<sub>EE</sub> spectra in (c) (blue). For (c–f), reaction spectra shown are averaged between  $t = 15$ – $18$  h after reaction initiation, and the residual from the fit are shown in magenta.

Furthermore, the spectra of K25C<sub>3IAP</sub> in the presence of stoichiometric unphosphorylated KaiC (KaiC<sub>ST</sub>, Figure 2d), and KaiC<sub>S431A,T432E</sub> (KaiC<sub>AE</sub>, Figure 2e) and KaiC<sub>S431E,T432A</sub> (KaiC<sub>EA</sub>, Figure 2f), two constructs mimicking, respectively, the dominant phosphostates KaiC<sub>SpT</sub> and KaiC<sub>pST</sub> during the day and at night,<sup>5</sup> could all be fit by linear combinations of free KaiB, 1:1, and 1:10 KaiB:KaiC<sub>EE</sub> spectra. Like N19C<sub>3IAP</sub>,<sup>29</sup> K25C<sub>3IAP</sub> did not show a cw-EPR spectral response at physiological ratios of KaiB to KaiA (Figure S7).<sup>33,34</sup> Combined, these results suggest that K25C<sub>3IAP</sub> serves as a probe for cooperative KaiB-KaiB interactions by distinguishing free KaiB from two subpopulations of KaiC-bound KaiB. These subpopulations are assigned as arising from contributions from “neighbored” (B<sub>+</sub>) and “neighborless” (B<sub>-</sub>) fs-KaiB, analogous to bulk and edge sites found in materials (Figure 2b). Under this assignment, B<sub>+</sub> corresponds to fs-KaiB that is

bound to KaiC and has an adjacent fs-KaiB on KaiC on the  $\alpha 1$  interface (green pentagons in Figure 2b), whereas B<sub>-</sub> is bound to KaiC and has no adjacent fs-KaiB on the  $\alpha 1$  interface (light purple pentagons in Figure 2b). Thus, our EPR results suggest that there are two distinctly different KaiB populations when bound to KaiC, B<sub>+</sub> and B<sub>-</sub>.

**Stepwise Assembly of the KaiBC Complex.** A long-standing question concerns the steps involved in the assembly of the dodecameric KaiB<sub>6</sub>C<sub>6</sub> complex starting from hexameric KaiC and tetrameric KaiB. To facilitate modeling of the binding kinetics and comparison of multiple kinetic models, we estimated the spectra of B<sub>+</sub> and B<sub>-</sub> via spectral simulations (see SI text 1.1 and Figure S8–18). We focused on KaiC<sub>ST</sub> and KaiC phosphomimetics (Figures 3 and 4) in the absence of KaiA to preclude changes in KaiC phosphostate from contributing to any observed KaiB-KaiC binding kinetics.

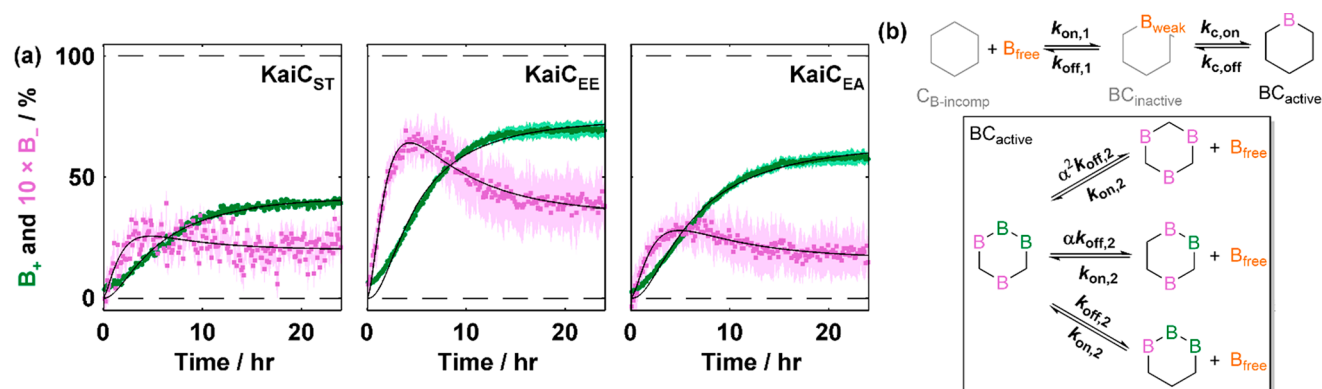


**Figure 3.** Stepwise assembly of KaiB-KaiC complexes as revealed by  $B_+$  and  $B_-$  kinetics. (a) cw-EPR derived KaiB-KaiC<sub>ST/EE/EA</sub> kinetics using K25C<sub>3IAP</sub> as a probe. Black solid lines show fits to model (SI Appendix, Table S13). Green circles and light purple squares correspond to the percentages of  $B_+$  and  $B_-$ , respectively. Shaded areas: 95% CI (KaiC<sub>ST</sub>, signal-to-noise,  $n = 1$ ; KaiC<sub>EE/EA</sub>, inter-replicate,  $n = 6$ ). (b) Scheme for modeling. KaiC is assumed to adopt two conformations, inactive (gray) and active (black). Free KaiB ( $B_{\text{free}}$ , orange) forms an encounter complex with inactive KaiC as a weak complex ( $B_{\text{weak}}$ ) that possesses identical cw-EPR spectrum as  $B_{\text{free}}$ . The encounter complex can either dissociate or change conformation to give a stably bound  $B_1C_6$  complex in which KaiC is activated and KaiB is fold switched, giving rise to  $B_-$  (light pink). Further, KaiB binding occurs in a fashion described by Koda and Saito and give rise to  $B_+$  (green).

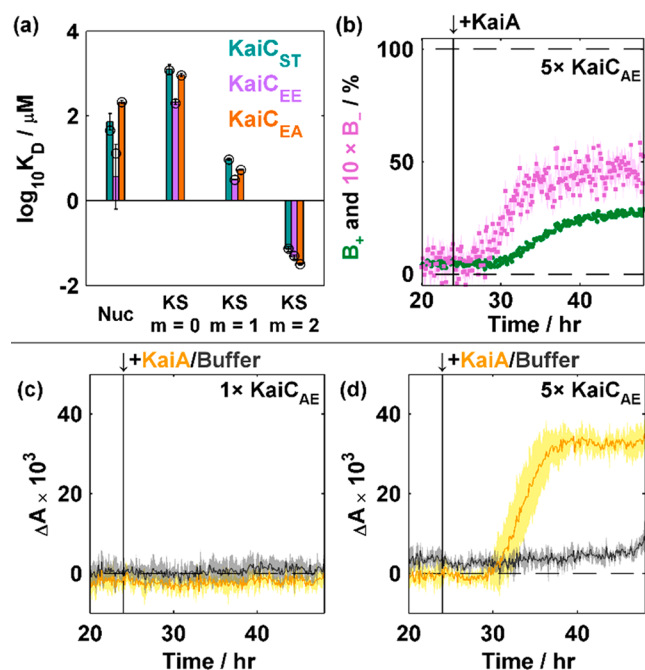


**Figure 4.** KaiC<sub>PSPT</sub>, not KaiC<sub>SPPT</sub>, seeds KaiB-KaiC interactions in the day-to-night transition. (a) The effective dissociation constants for each step in KaiB-KaiC binding in the encounter complex-stepwise binding model are plotted as bar graphs for KaiC<sub>ST</sub> (turquoise), KaiC<sub>EE</sub> (purple), and KaiC<sub>EA</sub> (orange). Error bars show standard deviation estimated by bootstrap resampling the original data set 20 times (see Table S14). Best fit results are shown as black open circles. (b) cw-EPR-derived kinetics of KaiB-KaiC<sub>AE</sub> binding with KaiA spiking at  $t = 24$  h. Green circles and light purple squares correspond to the percentages of  $B_+$  and  $B_-$ , respectively. Shaded areas: 95% CI (signal-to-noise,  $n = 1$ ). (c) and (d) Fluorescence anisotropy-based KaiB-KaiC<sub>AE</sub> binding assays under (c) 1 $\times$  and (d) 5 $\times$  KaiC protein concentrations with full-length KaiA (yellow) or buffer (gray) spiking at  $t = 24$  h (black line in all panels) using 50 nM KaiB-K25C-6IAF as fluorescence probe. In both panels, basal anisotropy based on KaiB alone were subtracted. Shaded areas show inter-replicate 95% CI ( $n = 3$ ).

KaiB was capable of binding to KaiC<sub>ST</sub>, KaiC<sub>EE</sub>, or KaiC<sub>EA</sub> in the absence of KaiA (Figure 3a). Here,  $B_+$  was observed as the

dominant steady-state species, whereas  $B_-$  was only present in small quantities (<10%), with the latter reaching maximum concentration at approximately  $t = 4$  h after initiation (Figures S19 and 20). Whereas initial  $B_-$  formation could be described by a pseudo-first-order reaction, the formation of  $B_+$  displayed sigmoidal kinetics, consistent with native PAGE data (Figure S3) as well as N19C<sub>3IAP</sub>-KaiC<sub>EE</sub> binding data.<sup>29</sup> Furthermore, our data support the intermediacy of  $B_-$  as a precursor to  $B_+$  as apparent from overlay plots of  $d[B_+]/dt$  and  $[B_-]$  showing similar time dependencies (Figure S19).

To evaluate the mechanism of KaiB-KaiC binding, we considered the model employed by Koda and Saito<sup>35</sup> as a starting point due to its explicit treatment of hexameric KaiC with each possessing varying amounts of KaiC-bound KaiB (Figure S21a). Briefly, this model assumes a fixed KaiB-KaiC binding rate  $k_{\text{on}}$ , but the dissociation rate  $k_{\text{off},0}$  is suppressed by adjacent KaiB subunits  $m$  ( $= 0, 1, \text{ or } 2$ ) in any KaiC-bound KaiB by a factor  $\alpha^m$ . Although the sigmoidal shape of the  $B_+$  kinetics observed in our experiments were recovered (Figure S21b,c, Table S7), their model also produced “burst-phase” behavior in  $B_-$  formation at  $t = 0.1$  h and failed to approach steady-state by  $t = 15$  h. To address this discrepancy, we first considered four additional models that couple with the Koda–Saito model with previously known phenomena typically associated with conformational selection, namely KaiB fold-switching,<sup>16</sup> KaiB tetramer-monomer equilibria,<sup>24</sup> and CI ATPase activity<sup>13,14</sup> or combinations thereof (see SI text 1.2, Figures S22–25, and Tables S8–S11). However, these models resulted in fits that overestimated the initial  $B_-$  formation in the time window  $t = 0–3$  h.

As incorporation of previously known phenomena into the Koda–Saito model failed to explain the observed kinetics, alternative models were sought. As a first attempt, we assumed that the initial KaiB-KaiC nucleation event ( $B_{\text{free}} + C_6 \rightleftharpoons B_1C_6$ ) possessed different rate constants from subsequent binding (Figure S26, Table S12). In effect, this nucleation event “primes” KaiC and locks KaiC into some KaiB-binding-compatible state. Curiously, this model reduced the overestimation of initial  $B_-$  formation as compared to conformational selection-based models. To expand upon this observation, we considered the formation of an encounter complex

between KaiB and KaiC followed by induced fitting for the nucleation event (Figure 3b, Table S13), with subsequent binding kinetics following that described by Koda and Saito.<sup>35</sup> In this model, KaiC initially exists in an inactive state that is unable to bind to KaiB strongly (gray in Figure 3b), presumably due to slow ATP hydrolysis in CI.<sup>13,14</sup> However, this inactive KaiC can form a weak encounter complex with KaiB (BC<sub>inactive</sub> in Figure 3b) in which the K25C<sub>3IAP</sub> spectral signature is identical to that of free KaiB. This weak encounter complex then establishes an equilibrium with the KaiB binding-competent state (BC<sub>active</sub>, black in Figure 3b), a process in which B<sub>-</sub> (light purple in Figure 3) is generated. This B<sub>1</sub>C<sub>active</sub> complex acts as a nucleation site to allow further KaiB-KaiC interactions in a manner described by Koda and Saito.<sup>35</sup> Such a model could satisfactorily reproduce the experimental KaiB-KaiC<sub>ST/EE/EA</sub> binding kinetics for both B<sub>+</sub> and B<sub>-</sub> (Figure 3a, Table S13). Thus, apart from confirming the stepwise nature of KaiB-KaiC complex formation from C<sub>6</sub> to B<sub>6</sub>C<sub>6</sub> via intermediates B<sub>i</sub>C<sub>6</sub> (*i* = 2, 3, 4, or 5), our data also hint at the existence of an encounter complex, with its nature to be examined in the future (see Discussion section).

**KaiC<sub>pSpT</sub>, not KaiC<sub>SpT</sub>, Promotes KaiB-KaiC Interactions in the Day-to-Night Transition.** The day-to-night transition is characterized by KaiC S431 phosphorylation and an increase in KaiB-KaiC interactions.<sup>36</sup> To determine which of the KaiC phosphostate, pS;pT or pS;T, is most responsible for nucleating KaiB-KaiC interactions, we quantified the effective equilibrium constants for KaiC<sub>ST/EE/EA</sub> by defining either  $K_{D,nuc} = \frac{k_{off,1}}{k_{on,1}} \times \frac{k_{c,off}}{k_{c,on}}$  (nucleation event in induced fit model, see derivation in text associated with Figure S27) or  $K_{D,KS,m} = \frac{\alpha^m k_{off,2}}{k_{on,2}}$  (Koda-Saito steps, *m* = 0, 1, or 2). In all models considered, KaiC<sub>EE</sub> possessed the smallest initial dissociation constants  $K_{D,nuc}$  and/or  $K_{D,KS,m=0}$  among KaiC<sub>ST</sub>, KaiC<sub>EE</sub>, and KaiC<sub>EA</sub> (Figure 4a, Figure S27a, and Table S14).

As KaiC<sub>SpT</sub> precedes KaiC<sub>pSpT</sub> in the KaiC phosphorylation cycle,<sup>5,6</sup> we also investigated the potential contribution of KaiC<sub>SpT</sub> in seeding KaiB-KaiC interactions by reacting K25C<sub>3IAP</sub> with KaiC<sub>AE</sub>. Unlike in the cases of KaiC<sub>ST/EE/EA</sub>, K25C<sub>3IAP</sub> alone was incapable of binding to KaiC<sub>AE</sub> (Figure S28), consistent with immunoprecipitation<sup>14</sup> and fluorescence anisotropy results.<sup>37</sup> To mimic midday conditions in which KaiC<sub>SpT</sub> associates with KaiA, KaiA was added to the KaiB-KaiC<sub>AE</sub> reaction mixture. Inclusion of KaiA led to a sigmoidal increase in B<sub>-</sub> and B<sub>+</sub> concentrations (Figure 4b), an observation that was paralleled by the analogous N19C<sub>3IAP</sub>-KaiC<sub>AE</sub> (Figure S29a) and fluorescence experiments carried out at 5× Kai protein concentrations but not at the standard 1× concentration (1.2 μM KaiA, 3.5 μM KaiB, and 3.5 μM KaiC, Figure 4c,d, Figure S29b). The cw-EPR formation kinetics of B<sub>-</sub> preceded that of B<sub>+</sub> in the ternary KaiA-KaiB-KaiC<sub>AE</sub> system, as revealed by the nonlinear correlation between them (Figure S28c), reinforcing the intermediate status of B<sub>-</sub> as a bridge between free KaiB and B<sub>+</sub>. The C-terminal domain of KaiA (KaiA<sub>181–284</sub>) henceforth referred to as C-KaiA), a KaiA construct devoid of the KaiB-binding motif, is less effective at driving KaiB-KaiC<sub>AE</sub> binding (Figure S29a), hinting at the role of ternary complex formation<sup>15,17</sup> in stabilizing KaiB-KaiC<sub>AE</sub> interactions. However, parallel real-time ATPase assays<sup>22</sup> (Figure S29c) and fluorescence assays at reduced ATP/ADP ratios (Figure S29b) suggest that KaiA-promoted KaiC ATPase activity<sup>7,8,38</sup> and consequent ATP

depletion at the 5× concentration contributed to the observed KaiB-KaiC<sub>AE</sub> interactions. Since the  $[ATP]/([ATP] + [ADP])$  levels in cyanobacterial cultures have been estimated to fall to a minimum of 40% even in prolonged darkness,<sup>39</sup> this cooperative KaiA-KaiB-KaiC<sub>AE</sub> binding is unlikely to be the main pathway in seeding KaiB-KaiC interactions during the day-to-night transition *in vivo*. Combined, our data imply that KaiC<sub>pSpT</sub> is the most competent KaiC phosphostate in initializing KaiB-KaiC interactions by stabilizing KaiBC nucleation sites.

**Freed KaiA Enhances Night-to-Day Transition by Promoting Dissociation of KaiB from KaiC<sub>pSpT</sub>.** Apart from KaiC dephosphorylation, the night-to-day transition of the Kai oscillator is also characterized by a reduction in KaiB-KaiC interactions and KaiBC-sequestered KaiA.<sup>36</sup> To examine the role of KaiA during the night phase, we subjected equilibrated K25C<sub>3IAP</sub>-KaiC<sub>EE/EA</sub> mixtures to KaiA spiking (Figures 5a, S30, and S31). Although previous KaiA-induced transient antagonization of KaiB-KaiC<sub>EE</sub> interactions<sup>29</sup> was successfully reproduced with K25C<sub>3IAP</sub> (Figures 5a, S30, and S31), this antagonization was far more pronounced in analogous KaiC<sub>EA</sub> experiments (Figure 5b). Notably, preformed B<sub>+</sub> diminished over 8 h with concurrent generation of B<sub>-</sub> (Figures 5b and S30). The correlation between the decrease in B<sub>+</sub> and the increase in B<sub>-</sub> (Figure S32), suggests that B<sub>-</sub> is a product of B<sub>+</sub> when KaiB-KaiC interactions are antagonized. Hence, our data establish B<sub>-</sub> as an intermediate between free KaiB and B<sub>+</sub> in both reaction directions.

To dissect the molecular basis of this antagonization, we subjected pre-equilibrated K25C<sub>3IAP</sub>-KaiC<sub>EA</sub> mixtures to the N- and C-terminal domains of KaiA (N-KaiA: KaiA<sub>1–135</sub>; C-KaiA as above; Figure 5c). While N-KaiA was incapable of antagonizing KaiB-KaiC<sub>EA</sub> interactions, the C-terminal domain of KaiA was found to be more effective than full-length KaiA (Figure S33). As C-KaiA contains an α-helical bundle capable of binding to KaiC CII A-loops<sup>9,40</sup> but lacks the KaiB-binding linker in the ternary KaiABC structure,<sup>17</sup> the enhancement in antagonization of KaiBC interactions by C-KaiA relative to full-length KaiA suggests an allosteric mechanism involving KaiA-CII interactions, possibly through CII-CI coupled nucleotide exchange.<sup>8</sup> Thus, contrary to previous assumptions of inactivation through ternary KaiABC complex formation,<sup>15</sup> our data suggest that nonsequestered KaiA released during stochastic dephosphorylation of KaiC<sub>pSpT</sub> facilitates the night-to-day transition by interacting with the CII-A loops in night-state KaiABC<sub>pSpT</sub> complexes.

**Bulk ↔ Edge Interconversion in the Core Oscillator.** It has been illustrated above that the B<sub>+</sub> and B<sub>-</sub> subpopulations of KaiC-bound KaiB (Figure 2b) possess different reactivities. The bulk KaiC-bound KaiB (B<sub>+</sub>) is the preferred steady-state species formed when pS431 phosphomimetics mimicking the dusk and night states or, to a lesser extent, unphosphorylated KaiC, KaiC<sub>ST</sub>, are present (Figure 3a). On the other hand, the edge KaiC-bound-KaiB (B<sub>-</sub>) is preferentially formed when KaiB-KaiC interactions are initiated (Figures 3a and 4b) or antagonized by KaiA (Figure 5b). To study the roles of the two populations in the Kai oscillator, we measured variations in B<sub>+</sub> and B<sub>-</sub> concentrations in real time in the reconstituted oscillator (Figure 6a) and compared their rhythms against the previously known sequential KaiC phosphorylation program<sup>5,6</sup> (Figure 5b). The cw-EPR spectra oscillated as evidenced by the periodic variation in the central transition intensity (Figure S34). When the spectra were quantitatively interpreted (Figure

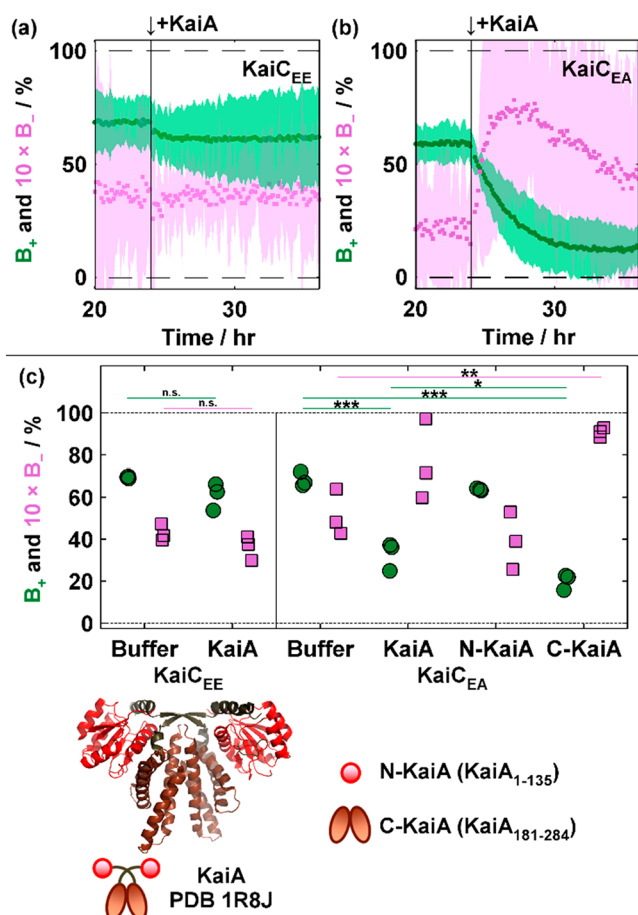


**Figure 5.** Nonsequestered KaiA triggers the night-to-day transition in KaiC<sub>pST</sub>. (a) and (b) cw-EPR derived kinetics of (a) KaiB-KaiC<sub>EE</sub> and (b) KaiB-KaiC<sub>EA</sub> binding with KaiA spiking at  $t = 24$  h. Green circles and light purple squares correspond to the percentages of B<sub>+</sub> and B<sub>-</sub>, respectively. Shaded areas: 95% CI (inter-replicate,  $n = 3$ ). (c) Efficacy of KaiA and its domains in antagonizing KaiB-KaiC<sub>EE/EA</sub> interactions. The KaiB-KaiC<sub>EE/EA</sub> reaction mixtures were incubated for 24 h and then spiked with buffer, full-length KaiA (KaiA), KaiA<sub>1-135</sub> (N-KaiA), or KaiA<sub>181-284</sub> (C-KaiA). Spectra were then collected within the 3.5–4 h window after spiking, and the results were binned. Top subpanel shows Tukey's HSD test ( $n = 3$ ): n.s., not significant; \*,  $p < 0.05$ ; \*\*,  $p < 0.01$ ; \*\*\*,  $p < 0.001$ . Each green circle and light purple square were derived by taking the mean of spectral modeling of individual spectra. Refer to SI Appendix, Figure S30 for representative spectra. The crystal structure of full-length KaiA (PDB 1R8J) and cartoon depiction of domains tested (N-terminal domain, red; C-terminal domain, brown; linker segment, brownish-olive) are shown below.

5a), the highly reproducible dynamics (Figure S35) could be divided into an initialization phase ( $t = 0-12$  h) and oscillation phase ( $t = 12-72$  h, Figure S36). During initialization, sigmoidal B<sub>+</sub> binding was observed, with B<sub>-</sub> concentration peaking at about 6 h and coinciding with the time at maximum B<sub>+</sub> rate of formation. This initialization behavior is similar to the dynamics observed in K25C<sub>3IAP</sub>-KaiC<sub>ST/EE/EA</sub> binding (Figure 4a) and consistent with our model that B<sub>-</sub> serves as a nucleation site. Once the reaction enters oscillation phase, however, B<sub>+</sub> and B<sub>-</sub> are essentially out of phase as verified by fitting both traces to sum of cosines (Figure S37 and Table S15).

To gain further insight into the inner workings of the Kai oscillator and relate these findings to clock output, the real-

time cw-EPR dynamics of KaiB were converted to phase angles to enable comparison with a previous KaiC-phosphorylation-derived model with implicit KaiB treatment by Rust et al. (Figure 6b).<sup>5</sup> Alignment of the phases with respect to maximal KaiB-KaiC interactions was performed under the assumption that KaiB-KaiC binding was completely described by B<sub>+</sub> and B<sub>-</sub> (Figure 5b). Under this assumption, the interconversion of B<sub>+</sub> to B<sub>-</sub> between  $\phi = 0^\circ$  to  $180^\circ$  occurs concurrently with KaiC<sub>pST</sub> dephosphorylation to KaiC<sub>ST</sub> and subsequent phosphorylation to KaiC<sub>SpT</sub>. As KaiB-KaiC<sub>EA</sub> interactions can be antagonized by KaiA to produce B<sub>-</sub> (Figure 5b), concurrent B<sub>+</sub> decomposition and B<sub>-</sub> formation observed during this phase imply that KaiA is involved in promoting this phase of the clock. Our phosphomimetic data also indicated that KaiC<sub>pSpT</sub> promotes KaiB-KaiC interactions. pST  $\rightarrow$  ST  $\rightarrow$  SpT events thus ensure that sequestered KaiA can be released for the next cycle while freeing up KaiC B-loops for eventual SasA binding.<sup>22</sup> The buildup of B<sub>-</sub> is facilitated by (i) a reduction in the initial  $K_{D,eff}$  ( $m = 0$ ) in KaiC<sub>pSpT</sub> relative to KaiC<sub>ST</sub> or KaiC<sub>pST</sub> (Figure S27) and to a lesser extent (ii) cooperative ternary KaiABC<sub>(p)SpT</sub> complex formation.<sup>15</sup> B<sub>-</sub> eventually reaches a maximum at about  $\phi = 180^\circ$ . As demonstrated in KaiC<sub>EE/EA</sub> phosphomimetic experiments and kinetic modeling (Figure 4a,b), B<sub>-</sub> is capable of recruiting B<sub>+</sub> and is responsible for the sigmoidal kinetics in those experiments. Thus, it is inferred that the buildup of B<sub>-</sub> aids in promoting KaiB-KaiC<sub>pSpT/pST</sub> binding by acting as nucleation sites for further KaiB binding during the day-to-night transition between  $\phi = 180^\circ$  and  $360^\circ$ . Furthermore, KaiB-KaiC<sub>EE</sub> interactions are not as susceptible to KaiA-induced antagonization as is KaiC<sub>EA</sub> (Figure 5c). Hence, the pSpT  $\rightarrow$  pST dephosphorylation event gates the clock toward the dawn state and allows sufficient time for CikA to interact with KaiC-bound KaiB.<sup>17,22</sup>

## DISCUSSION

As KaiB-KaiC binding indirectly regulates gene expression *in vivo* via controlling the activity of two cognate histidine kinases, SasA and CikA,<sup>20,22</sup> that modulate the activity of RpaA, a master transcription factor (Figure 1b), the ability of the core oscillator in regulating KaiB-KaiC interactions, is of fundamental interest. We have demonstrated that differentiating the roles of “bulk” versus “edge” KaiC-bound KaiB sites is an important mechanism for regulating KaiB-KaiC interactions. The concept of differing reactivities between “bulk” and “edge” sites is a kinetic manifestation to cooperativity that has been characterized in the Kai system.<sup>14,22</sup> From a functional perspective, the autocatalytic nature of KaiB-KaiC binding creates a temporal delay between maximal rate of binding and maximal binding (i.e., KaiB<sub>6</sub>C<sub>6</sub> ring completion). Such delay is likely to be important for ensuring a proper activation window for the output histidine kinase SasA, the latter of which preferentially binds to KaiC<sub>EE</sub> than KaiC<sub>EA</sub>.<sup>22</sup> establishes steady-state binding to KaiC<sub>EA</sub> in approximately 5 h,<sup>16</sup> and shares a thioredoxin fold domain with fs-KaiB.<sup>16</sup> Unlike KaiB which exhibits edge nucleation effects, SasA displays little inter-SasA homocooperativity<sup>25</sup> and fails to occupy all six binding sites on the KaiC hexamer.<sup>22</sup> Thus, our results suggest that, in addition to fold switching between its inactive stable tetrameric fold to the active but unstable thioredoxin fold, KaiB-KaiC cooperativity provides an extra layer to regulate KaiB-KaiC binding in generating such delay.<sup>16</sup>

**Gaps in Knowledge in How KaiB-KaiC Complexes Assemble.** Our KaiB-KaiC binding data can be explained by

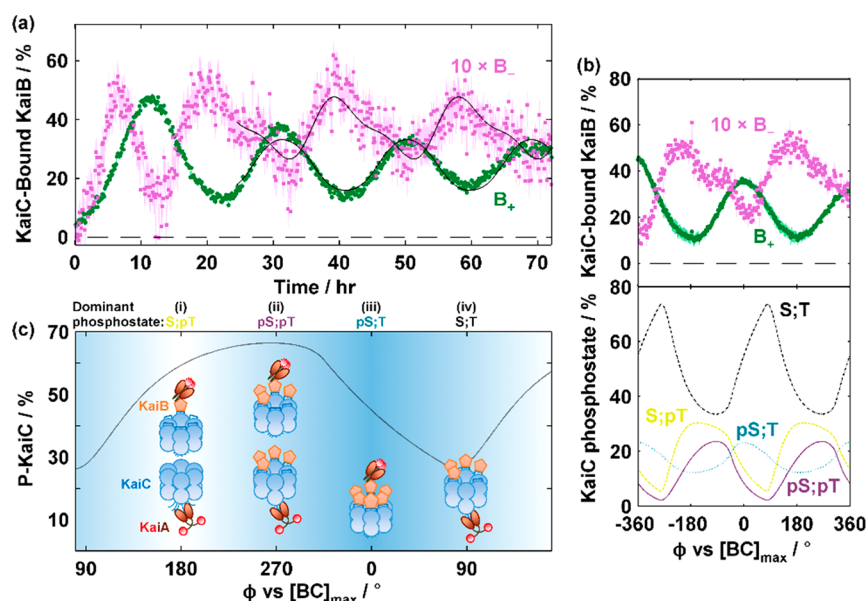


**Figure 6.** Dynamics of KaiC-bound KaiB subpopulations in the reconstituted Kai oscillator. (a) cw-EPR-based kinetics of B<sub>+</sub> and B<sub>-</sub> as a function of time. Shaded areas represent 95% CI due to imperfect signal-to-noise. Fit to sum of cosines is overlaid as solid black lines (See SI Appendix, Table S14). (b) Stacked plot of phase relationships. The KaiC-bound KaiB populations are B<sub>+</sub> (green circles) and B<sub>-</sub> (light purple squares). The KaiC phosphostates are KaiC<sub>ST</sub> (black dash-dot line), KaiC<sub>SPT</sub> (dark yellow dashed line), KaiC<sub>pSpT</sub> (purple solid line), and KaiC<sub>pST</sub> (turquoise dotted line). The SEM ( $n = 3$ ) shown as shaded areas is visible at higher magnification. (c) Model of events governing KaiB-KaiC binding in the Kai oscillator. (i) During the day, KaiC (blue) is predominantly in the KaiC<sub>SPT</sub> state with gradual buildup in KaiC<sub>pSpT</sub>. The former can bind to KaiB (orange) only in ATP-depleted conditions, whereas the latter can bind to KaiB unaided. This constitutes the nucleation event in KaiB-KaiC binding. (ii) As time progresses, KaiC<sub>pSpT</sub> builds up. Pre-existing KaiC-bound KaiB recruits further KaiB binding which provides additional fs-KaiB for sequestering KaiA (red/brown). (iii) The KaiB<sub>6</sub>C<sub>6</sub> ring completes. With KaiA sequestered, KaiC autophosphatase activity dominates. (iv) Unlike KaiC<sub>pSpT</sub>, KaiB-KaiC<sub>pST</sub> binding is sensitive to antagonization by KaiA. KaiA triggers the release of fs-KaiB from KaiC, creating nucleation sites for the next cycle.

complementing the Koda–Saito model with an encounter complex formation step (Figure 3b). Further experiments will be necessary to confirm the existence of the encounter complex and elucidate its nature. Nevertheless, our data further reinforce the notion that inter-KaiB cooperativity plays a critical role in KaiB-KaiC interactions. We point out that the induced-fit model introduced in this work is distinct from either the conformational selection model presented in our previous work, where KaiB and KaiC were assumed to establish individual equilibria to form active states prior combining to form the KaiBC complex,<sup>16</sup> or the two-site cooperative binding model, where KaiC was assumed to have two types of sites, with occupation of the first site by either fs-KaiB or N-SasA facilitating further KaiB-KaiC binding.<sup>22</sup> The necessity to use different models to explain the data may lie in the concentrations of the proteins used, with low KaiB concentrations (50 nM) obscuring intrinsic inter-KaiB cooperativity while promoting monomeric KaiB formation.<sup>24</sup> It is plausible that monomeric KaiB might be prone to fold-switching and could bind to KaiC without forming an encounter complex. Indeed, while the oligomeric distribution between monomeric, dimeric, and tetrameric KaiB have been estimated by native mass spectrometry,<sup>24</sup> the distribution between ground-state versus fold-switched KaiB has only been estimated via fitting of burst-phase KaiB-KaiC binding kinetics,<sup>16</sup> but not directly observed. Furthermore, conformational selection and induced fit pathways are not mutually exclusive and can depend critically on protein concentrations.<sup>41</sup> Despite these shortcomings in our model, the use of K25C<sub>31AP</sub> in quantifying two subpopulations of KaiC-bound

KaiB improves upon previous implicit treatments<sup>5,14</sup> and shall complement previous KaiC-phosphostate based assays.

The ability to quantify trace amounts of B<sub>-</sub> via cw-EPR provides the first kinetic data to support inter-KaiB cooperativity. This was accomplished through detection of intermediate substoichiometric KaiBC complexes that were invisible to previous native mass spectrometry approaches.<sup>24,25</sup> Specifically, under all reaction conditions with typical KaiB-to-KaiC ratios considered, B<sub>-</sub> never exceeded 10% of total KaiB. Using the augmented Koda–Saito model (Figure 3b), we estimated the fractional concentrations of strongly bound substoichiometric KaiB<sub>*i*</sub>C<sub>6</sub> complexes ( $i = 1, 2, 3, 4, \text{ or } 5$ ) to be <10% of total KaiC (Figure S27b). Similar results were obtained when the encounter complex was neglected or when conformational selection models were assumed instead (Figure S27b). The low fractional concentrations of these substoichiometric complexes coupled with limited mass resolution in the original experiments by Snijder et al.<sup>24</sup> might have prevented their direct detection. These experiments should be revisited in the future as technological advances in native mass spectrometry are made.

**KaiC Phosphostate-Mediated Affinity and Cooperativity Tuning.** Cooperativity within KaiC hexamers was demonstrated by Lin et al.,<sup>14</sup> where mixtures of KaiC<sub>pST</sub> and KaiC<sub>SPT</sub> phosphomimetics were combined and assayed for their resultant KaiB binding affinities. In this study, apart from establishing the importance of inter-KaiB cooperativity in controlling KaiB-KaiC binding, we also observed phosphostate-dependent KaiB-KaiC binding in the order of KaiC<sub>AE</sub> ≪ KaiC<sub>ST</sub> < KaiC<sub>EE/EA</sub>. Furthermore, the presence of KaiA attenuates the relative populations of B<sub>+</sub> and B<sub>-</sub>. These



observations imply that both KaiA and the phosphostate in CII can modulate inter-KaiB cooperativity in CI tens of angstroms away.

The computed  $K_{D,eff}$  is lowest in KaiC<sub>EE</sub> for the nucleation step ( $B_{free} + C_6 \rightarrow B_1C_6$ ) in all models considered (Figure S27a), suggesting that KaiC<sub>pST</sub> is more effective at KaiB-KaiC binding nucleation than KaiC<sub>ST</sub>. This conclusion is distinct from that drawn from fluorescence anisotropy using 50 nM fluorescently labeled KaiB and variable KaiC concentrations in that the  $K_D$  between KaiB and KaiC<sub>EE</sub> versus KaiC<sub>EA</sub> were similar.<sup>22</sup> We speculate that this difference originates from the low concentration of KaiB used in fluorescence anisotropy experiments that might bias KaiB toward its monomeric state while precluding the observation of intrinsic inter-KaiB cooperativity, as discussed above. On the other hand, NMR spectroscopy demonstrated that KaiB-KaiC binding is enabled by an increase in CII rigidity<sup>11</sup> and subsequent stacking on CI,<sup>10</sup> which stabilizes the posthydrolysis state of CI. As T432 phosphorylation reduces CII rigidity, an explanation for the counterintuitive observation that KaiC<sub>pST</sub> has comparable or potentially higher KaiB-KaiC affinity than KaiC<sub>ST</sub> does (Figure 3a) is warranted but awaits more detailed studies. The  $B_6C_6^{EA}$  complex has previously been crystallized,<sup>17</sup> whereas  $B_6C_6^{EE}$  has not. Additional experiments will be necessary to determine the structural basis of these observations.

As KaiC is a member of the AAA+ ATPase family,<sup>42</sup> many of which are hexameric but capable of breaking their  $C_6$  symmetry by means of differential nucleotide incorporation,<sup>43</sup> inter-KaiB cooperativity is likely tuned by KaiC phosphostate distribution within individual KaiC hexamers. Asymmetry in KaiC can then be introduced by intrinsic ATPase activity of CI<sup>12</sup> and/or nucleotide exchange in CII,<sup>8</sup> both of which are modulated by KaiC phosphostate.<sup>38</sup> Nucleotide exchange in CII has recently been modeled by molecular dynamics simulations to result in a split washer structure, with this asymmetry propagating toward CI.<sup>8</sup> Experimental verification of this symmetry breaking and its impact on inter-KaiB cooperativity shall be addressed in the future.

**The Function of KaiA during Night-to-Day Transition and Plausible Mechanisms.** Our KaiA-spiking experiments suggest that KaiA is not a passive player during the night state that is solely inactivated from promoting nucleotide exchange in KaiC.<sup>7,8</sup> Rather, KaiA plays an active role in antagonizing KaiB-KaiC<sub>pST</sub> interactions (Figure 5c). Furthermore, a reduction in KaiB-KaiC<sub>pST</sub> interactions implies a reduction in available fs-KaiB for sequestering KaiA in the form of ternary KaiABC complexes.<sup>17,27</sup> Consequently, a single KaiA dimer may trigger an autocatalytic cascade of KaiA release and further antagonization of KaiB-KaiC<sub>pST</sub> interactions by creating a positive feedback loop, a model to be tested. In the context of the full oscillator, this cascade is likely initiated by and enhanced during stochastic KaiC<sub>pST</sub> dephosphorylation to KaiC<sub>ST</sub> (Figure 6b), a phosphostate that is a poorer binding partner to KaiB than KaiC<sub>pST</sub> (Figures 3a and 4a).

The dissociation of KaiBC complexes is a possible prerequisite to providing functional output of the oscillator by regenerating CI sites for SasA binding<sup>20</sup> during the next cycle. As SasA and fs-KaiB compete for overlapping binding sites with CI,<sup>15</sup> the ability for SasA activation by binding to KaiC depends on CI availability. KaiA-induced KaiBC<sub>pST</sub> antagonization provides an avenue to generate open CI sites. Coupled with the delayed KaiB-KaiC<sub>pST</sub> binding kinetics

(Figure 4a) as compared to N-SasA,<sup>16</sup> a robust SasA activation rhythm can be generated.<sup>22</sup>

The molecular origin of KaiA-induced KaiBC<sub>pST</sub> antagonization has yet to be discovered. However, our data that C-KaiA is sufficient to antagonize KaiB-KaiC interactions (Figure 5c) lend support toward an allosteric pathway involving the interactions between KaiC CII A loops and the C-terminal domain of KaiA. We thus propose an antagonization pathway where (1) KaiA interacts with CII A-loops, resulting in (2) nucleotide exchange in CI, the former of which is the direct cause of dissociation of KaiBC complexes. In the first step, KaiA is presented with two potential sites for binding to binary KaiBC<sub>pST</sub> complexes. While most of KaiA is sequestered by fs-KaiB, a small fraction binds to the C-terminal A-loop and tail residues of KaiC instead.<sup>40,44</sup> This binding occurs as a consequence of weak but nonzero intrinsic A-loop exposure in KaiC<sub>pST</sub> and is enhanced on stochastic S431 dephosphorylation to unphosphorylated KaiC<sub>ST</sub>.<sup>15</sup> Whether KaiA-induced antagonization is more potent in KaiC<sub>pST</sub> or KaiC<sub>ST</sub> is unknown at the moment due to the inability to perform analogous antagonization experiments on KaiC<sub>ST</sub> without reconstituting the oscillator, but this question may be irrelevant given the mixed-phosphostate nature of KaiC hexamers in the oscillator.<sup>14</sup> In the second step, the KaiA-CII A-loop and tail interaction promotes nucleotide exchange in CII<sup>7</sup> and weakens KaiB-KaiC interactions through two mechanisms. First, KaiA-A loop interactions loosen the hexameric CII ring, which disrupts the stacking between CII and CI<sup>11</sup> and breaks the symmetry within KaiC.<sup>8</sup> Unstacking of the rings leads to withdrawal of KaiB-binding sites in KaiC, which weakens KaiB-KaiC interactions and hence inter-KaiB cooperativity. Second, the CI-CII linker has been hypothesized to behave as a nucleotide exchange factor for CI, analogous to the A-loop and tail residues to CII.<sup>8</sup> As stable KaiB-KaiC<sub>pST</sub> interactions require B-loop exposure in CI which in turn depends on CI to be in a posthydrolysis state,<sup>17</sup> coupled CII-CI nucleotide exchange leads to KaiBC<sub>pST</sub> antagonization.

Our work supports the idea that the CI and CII rings of KaiC are coupled such that KaiA-CII interactions and KaiB-CI interactions are mutually exclusive – A-loops are maximally hidden when B-loops are maximally exposed and vice versa. Thus, KaiC might have evolved to separate daytime and nighttime activities through this long-range coupling. Furthermore, our model explains the relative strengths of various KaiA constructs in antagonizing KaiB-KaiC<sub>EA</sub> interactions (Figure 5c) that C-KaiA > KaiA ≫ N-KaiA ~ control. Full-length KaiA consists of N- and C-terminal domains that are joined by a linker segment.<sup>45</sup> In the ternary KaiABC crystal structure, a truncated KaiA construct missing the N-terminal domain was found to be in an autoinhibited state in which the KaiA- $\alpha 5$  helix is bound to the C-terminal helix bundle,<sup>17</sup> the site implicated in KaiA-CII A-loops + tail interactions.<sup>40,46</sup> As this helix bundle is the active site for antagonizing KaiB-KaiC interactions, simultaneous removal of KaiA- $\alpha 5$  and the N-terminal domain results in the C-KaiA construct (Figure 5c) that is incapable of binding to and consequently uninhibited by fs-KaiB. This results in a constitutively active KaiA construct that is more effective at antagonizing KaiB-KaiC<sub>EA</sub> interactions relative to full-length KaiA. On the contrary, the N-terminal pseudo-receiver domain is capable of redox state sensing<sup>47</sup> but otherwise unable to regulate KaiB-KaiC interactions when isolated. Instead, its paradoxical role in full-length KaiA may lie in its ability to activate the nucleotide exchange factor activity

of C-terminal domain of KaiA<sup>40,46</sup> by competing for KaiA- $\alpha$ 5 and exposing the C-terminal helix bundle to KaiC A-loop + tail binding.

**Evolutionary Adaptations in KaiA Confer Fitness in Diverse Environments.** Although the loss of KaiA results in arrhythmia in *S. elongatus*<sup>37</sup> and consequently a loss in fitness in light–dark cycles, its absence in *Prochlorococcus marinus* MED4<sup>48</sup> or truncation in strains such as *Nodularis spumigena* CCY9414<sup>49</sup> suggests evolutionary advantages to such modifications.<sup>50</sup> How fitness is conferred by the loss of KaiA in *P. marinus* has recently been addressed by Chew et al.<sup>33</sup> – the marine environment might provide a higher regularity of cues to *P. marinus*, whereas its smaller cellular volume renders the Kai oscillator susceptible to stochastic noise. These factors result in a KaiA-less timing mechanism that behaves as an hourglass rather than a clock.<sup>51</sup> In vivo, *P. marinus* KaiC (ProKaiC) might be able to directly respond to cellular ATP concentrations without an external nucleotide exchange factor as evidenced by its hyper- and hypophosphorylation when *P. marinus* is subjected to constant light or darkness, respectively.<sup>33</sup> This is possibly achieved by ProKaiC's intrinsically higher autokinase activity compared to KaiC in *S. elongatus*.<sup>51</sup> Does the elevated autokinase activity imply an increased intrinsic CI nucleotide exchange rate in ProKaiC that prevents ProKaiB-ProKaiC binding even in hyperphosphorylated ProKaiC except in ATP depleted conditions during nighttime? If so, the loss of ProKaiB-ProKaiC interactions during the night-to-day transition in *P. marinus* would be entirely dictated by photosynthetic ATP influx. Analogous ProKaiB-ProKaiC experiments are necessary in understanding the diversity in clock mechanisms within cyanobacteria. On the other hand, the biofilm-forming *N. spumigena* is found in brackish water and possesses a truncated KaiA (NodKaiA)<sup>50</sup> that is homologous to the C-terminal KaiA<sub>181–284</sub> (C-KaiA) used in our experiments (Figure 5c). The lack of the N-terminal pseudoreceiver domain as well as the fs-KaiB-binding motifs likely lead to constant activation of NodKaiA as a nucleotide exchange factor for KaiC as well as weakened KaiB-KaiC interactions. Does this truncation lead to enhanced ATP sensitivity in *N. spumigena* and render it an hourglass, not unlike *P. marinus*? Further experiments will be necessary to understand the evolutionary advantages conferred by these modifications.

## CONCLUSIONS

First, by spin labeling at KaiB-K25 via site-directed mutagenesis, we demonstrated the existence of B<sub>-</sub> and B<sub>+</sub>, two subpopulations of KaiC-bound KaiB corresponding to edge and bulk sites, respectively. The intermediacy of B<sub>-</sub> between free KaiB and B<sub>+</sub> was verified by reacting K25C<sub>31AP</sub> with KaiC phosphomimetics. Second, we showed that KaiBC complexes assembled via a stepwise fashion, with hyperphosphorylated KaiC<sub>pSP<sub>T</sub></sub> being the most effective at initiating KaiBC complex formation. We showed that the binding kinetics could be fitted to an induced-fit model involving an encounter complex. Third, we demonstrated the role of KaiA in antagonizing KaiB-KaiC<sub>pSP<sub>T</sub></sub> interactions and facilitating the night-to-day transition. The ability of a truncated KaiA construct to antagonize KaiB-KaiC interactions suggested long-range allosteric coupling to be a contributing mechanism. Lastly, we developed a multiobjective optimization approach to extracting kinetics from experimental cw-EPR data by coupling spectral simulations with physicality constraints. This approach extends

the applicability of cw-EPR as a bioanalytical technique to interrogate biochemical systems.

## ASSOCIATED CONTENT

### Supporting Information

The Supporting Information is available free of charge at <https://pubs.acs.org/doi/10.1021/jacs.1c08103>.

Experimental details and additional characterization data (PDF)

### Accession Codes

*S. elongatus* (PCC 7942) KaiC, UnitProt entry Q79PF4; *S. elongatus* (PCC 7942) KaiB, UnitProt entry Q79PF5; *S. elongatus* (PCC 7942) KaiA, UnitProt entry Q79PF6.

## AUTHOR INFORMATION

### Corresponding Authors

Andy LiWang – School of Natural Sciences, Chemistry and Biochemistry, Health Sciences Research Institute, and Center for Cellular and Biomolecular Machines, University of California, Merced, California 95343, United States; Center for Circadian Biology, University of California, San Diego, La Jolla, California 92093, United States; Email: [aliwang@ucmerced.edu](mailto:aliwang@ucmerced.edu)

R. David Britt – Department of Chemistry, University of California, Davis, California 95616, United States; [orcid.org/0000-0003-0889-8436](https://orcid.org/0000-0003-0889-8436); Email: [rdbritt@ucdavis.edu](mailto:rdbritt@ucdavis.edu)

### Authors

Gary K. Chow – Department of Chemistry, University of California, Davis, California 95616, United States; Present Address: Department of Entomology and Nematology, University of California, Davis, California 95616, United States; [orcid.org/0000-0001-9200-0857](https://orcid.org/0000-0001-9200-0857)

Archana G. Chavan – School of Natural Sciences, University of California, Merced, California 95343, United States; Present Address: Genentech, San Francisco, California 94080, United States

Joel Heisler – Chemistry and Chemical Biology, University of California, Merced, California 95343, United States; Present Address: Genentech, San Francisco, California 94080, United States

Yong-Gang Chang – School of Natural Sciences, University of California, Merced, California 95343, United States; Present Address: Monash Biomedicine Discovery Institute, Monash University, Clayton, Victoria 3800, Australia

Ning Zhang – School of Natural Sciences, University of California, Merced, California 95343, United States

Complete contact information is available at: <https://pubs.acs.org/10.1021/jacs.1c08103>

### Notes

The authors declare no competing financial interest.

## ACKNOWLEDGMENTS

We thank Drs. William Jewell and Armann Andaya for their help in acquiring LCMS data. We thank Professors Adam Moule and Carrie L. Partch and Dr. Lu Hong for valuable insights. This work was supported by grants from the U.S. National Science Foundation (NSF-MCB-1615752 to R.D.B.; NSF-HRD-1547848 to CREST: Center for Cellular and Biomolecular Machines at UC Merced), National Institutes

of Health (GM107521 to A.L.), and Army Research Office (W911NF-17-1-0434 to A.L.).

## REFERENCES

- (1) Dunlap, J. C. Molecular Bases for Circadian Clocks. *Cell* **1999**, *96* (2), 271–290.
- (2) Lambert, G.; Chew, J.; Rust, M. J. Costs of Clock-Environment Misalignment in Individual Cyanobacterial Cells. *Biophys. J.* **2016**, *111* (4), 883–891. Ouyang, Y.; Andersson, C. R.; Kondo, T.; Golden, S. S.; Johnson, C. H. Resonating circadian clocks enhance fitness in cyanobacteria. *Proc. Natl. Acad. Sci. U. S. A.* **1998**, *95* (15), 8660–8664.
- (3) Nakajima, M.; Imai, K.; Ito, H.; Nishiwaki, T.; Murayama, Y.; Iwasaki, H.; Oyama, T.; Kondo, T. Reconstitution of circadian oscillation of cyanobacterial KaiC phosphorylation in vitro. *Science* **2005**, *308* (5720), 414–415.
- (4) Tomita, J.; Nakajima, M.; Kondo, T.; Iwasaki, H. No transcription-translation feedback in circadian rhythm of KaiC phosphorylation. *Science* **2005**, *307* (5707), 251–254.
- (5) Rust, M. J.; Markson, J. S.; Lane, W. S.; Fisher, D. S.; O’Shea, E. K. Ordered phosphorylation governs oscillation of a three-protein circadian clock. *Science* **2007**, *318* (5851), 809–812.
- (6) Nishiwaki, T.; Satomi, Y.; Kitayama, Y.; Terauchi, K.; Kiyohara, R.; Takao, T.; Kondo, T. A sequential program of dual phosphorylation of KaiC as a basis for circadian rhythm in cyanobacteria. *EMBO J.* **2007**, *26* (17), 4029–4037.
- (7) Nishiwaki-Ohkawa, T.; Kitayama, Y.; Ochiai, E.; Kondo, T. Exchange of ADP with ATP in the CII ATPase domain promotes autophosphorylation of cyanobacterial clock protein KaiC. *Proc. Natl. Acad. Sci. U. S. A.* **2014**, *111* (12), 4455–4460.
- (8) Hong, L.; Vani, B. P.; Thiede, E. H.; Rust, M. J.; Dinner, A. R. Molecular dynamics simulations of nucleotide release from the circadian clock protein KaiC reveal atomic-resolution functional insights. *Proc. Natl. Acad. Sci. U. S. A.* **2018**, *115* (49), E11475–E11484.
- (9) Kim, Y. I.; Dong, G.; Carruthers, C. W.; Golden, S. S.; LiWang, A. The day/night switch in KaiC, a central oscillator component of the circadian clock of cyanobacteria. *Proc. Natl. Acad. Sci. U. S. A.* **2008**, *105* (35), 12825–12830.
- (10) Chang, Y. G.; Tseng, R.; Kuo, N. W.; LiWang, A. Rhythmic ring-ring stacking drives the circadian oscillator clockwise. *Proc. Natl. Acad. Sci. U. S. A.* **2012**, *109* (42), 16847–16851.
- (11) Chang, Y. G.; Kuo, N. W.; Tseng, R.; LiWang, A. Flexibility of the C-terminal, or CII, ring of KaiC governs the rhythm of the circadian clock of cyanobacteria. *Proc. Natl. Acad. Sci. U. S. A.* **2011**, *108* (35), 14431–14436.
- (12) Abe, J.; Hiyama, T.; Mukaiyama, A.; Son, S.; Mori, T.; Saito, S.; Osako, M.; Wolanin, J.; Yamashita, E.; Kondo, T.; et al. Atomic-scale origins of slowness in the cyanobacterial circadian clock. *Science* **2015**, *349* (6245), 312–316.
- (13) Phong, C.; Markson, J. S.; Wilhoite, C. M.; Rust, M. J. Robust and tunable circadian rhythms from differentially sensitive catalytic domains. *Proc. Natl. Acad. Sci. U. S. A.* **2013**, *110* (3), 1124–1129.
- (14) Lin, J.; Chew, J.; Chockanathan, U.; Rust, M. J. Mixtures of opposing phosphorylations within hexamers precisely time feedback in the cyanobacterial circadian clock. *Proc. Natl. Acad. Sci. U. S. A.* **2014**, *111* (37), E3937–E3945.
- (15) Tseng, R.; Chang, Y. G.; Bravo, I.; Latham, R.; Chaudhary, A.; Kuo, N. W.; LiWang, A. Cooperative KaiA-KaiB-KaiC interactions affect KaiB/SasA competition in the circadian clock of cyanobacteria. *J. Mol. Biol.* **2014**, *426* (2), 389–402.
- (16) Chang, Y. G.; Cohen, S. E.; Phong, C.; Myers, W. K.; Kim, Y. I.; Tseng, R.; Lin, J.; Zhang, L.; Boyd, J. S.; Lee, Y.; et al. A protein fold switch joins the circadian oscillator to clock output in cyanobacteria. *Science* **2015**, *349* (6245), 324–328.
- (17) Tseng, R.; Goularte, N. F.; Chavan, A.; Luu, J.; Cohen, S. E.; Chang, Y. G.; Heisler, J.; Li, S.; Michael, A. K.; Tripathi, S.; et al. Structural basis of the day-night transition in a bacterial circadian clock. *Science* **2017**, *355* (6330), 1174–1180.
- (18) Markson, J. S.; Piechura, J. R.; Puszyńska, A. M.; O’Shea, E. K. Circadian control of global gene expression by the cyanobacterial master regulator RpaA. *Cell* **2013**, *155* (6), 1396–1408.
- (19) Takai, N.; Nakajima, M.; Oyama, T.; Kito, R.; Sugita, C.; Sugita, M.; Kondo, T.; Iwasaki, H. A KaiC-associating SasA-RpaA two-component regulatory system as a major circadian timing mediator in cyanobacteria. *Proc. Natl. Acad. Sci. U. S. A.* **2006**, *103* (32), 12109–12114.
- (20) Gutu, A.; O’Shea, E. K. Two antagonistic clock-regulated histidine kinases time the activation of circadian gene expression. *Mol. Cell* **2013**, *50* (2), 288–294.
- (21) Valencia, S. J.; Bitou, K.; Ishii, K.; Murakami, R.; Morishita, M.; Onai, K.; Furukawa, Y.; Imada, K.; Namba, K.; Ishiura, M. Phase-dependent generation and transmission of time information by the KaiABC circadian clock oscillator through SasA-KaiC interaction in cyanobacteria. *Genes Cells* **2012**, *17* (5), 398–419.
- (22) Chavan, A. G.; Swan, J. A.; Heisler, J.; Sancar, C.; Ernst, D. C.; Fang, M.; Palacios, J. G.; Spangler, R. K.; Bagshaw, C. R.; Tripathi, S.; et al. Reconstitution of an intact clock reveals mechanisms of circadian timekeeping. *Science* **2021**, *374* (6564), eabd4453.
- (23) Kaur, M.; Ng, A.; Kim, P.; Diekman, C.; Kim, Y.-I. CikA Modulates the Effect of KaiA on the Period of the Circadian Oscillation in KaiC Phosphorylation. *J. Biol. Rhythms* **2019**, *34* (2), 218–223.
- (24) Snijder, J.; Burnley, R. J.; Wiegard, A.; Melquiond, A. S. J.; Bonvin, A. M. J. J.; Axmann, I. M.; Heck, A. J. R. Insight into cyanobacterial circadian timing from structural details of the KaiB-KaiC interaction. *Proc. Natl. Acad. Sci. U. S. A.* **2014**, *111* (4), 1379–1384.
- (25) Murakami, R.; Yunoki, Y.; Ishii, K.; Terauchi, K.; Uchiyama, S.; Yagi, H.; Kato, K. Cooperative Binding of KaiB to the KaiC Hexamer Ensures Accurate Circadian Clock Oscillation in Cyanobacteria. *Int. J. Mol. Sci.* **2019**, *20*, 4550.
- (26) Garces, R. G.; Wu, N.; Gillon, W.; Pai, E. F. Anabaena circadian clock proteins KaiA and KaiB reveal a potential common binding site to their partner KaiC. *EMBO J.* **2004**, *23* (8), 1688–1698.
- (27) Snijder, J.; Schuller, J.; Wiegard, A.; Lossl, P.; Schmelling, N.; Axmann, I.; Plitzko, J.; Forster, F.; Heck, A. Structures of the cyanobacterial circadian oscillator frozen in a fully assembled state. *Science* **2017**, *355* (6330), 1181–1184.
- (28) Villarreal, S. A.; Pattanayek, R.; Williams, D. R.; Mori, T.; Qin, X. M.; Johnson, C. H.; Egli, M.; Stewart, P. L. CryoEM and Molecular Dynamics of the Circadian KaiB-KaiC Complex Indicates That KaiB Monomers Interact with KaiC and Block ATP Binding Clefs. *J. Mol. Biol.* **2013**, *425* (18), 3311–3324. Hitomi, K.; Oyama, T.; Han, S.; Arvai, A. S.; Getzoff, E. D. Tetrameric architecture of the circadian clock protein KaiB. A novel interface for intermolecular interactions and its impact on the circadian rhythm. *J. Biol. Chem.* **2005**, *280* (19), 19127–19135.
- (29) Chow, G. K.; Chavan, A. G.; Heisler, J. C.; Chang, Y.-G.; LiWang, A.; Britt, R. D. Monitoring Protein-Protein Interactions in the Cyanobacterial Circadian Clock in Real Time via Electron Paramagnetic Resonance Spectroscopy. *Biochemistry* **2020**, *59* (26), 2387–2400.
- (30) Halle, B.; Davidovic, M. Biomolecular hydration: from water dynamics to hydrodynamics. *Proc. Natl. Acad. Sci. U. S. A.* **2003**, *100* (21), 12135–12140.
- (31) Guo, Z.; Cascio, D.; Hideg, K.; Hubbell, W. L. Structural determinants of nitroxide motion in spin-labeled proteins: solvent-exposed sites in helix B of T4 lysozyme. *Protein Sci.* **2008**, *17* (2), 228–239.
- (32) Wong, L.T.L.; Piette, L.H.; Little, J.R.; Hsia, J.C. Stereospecificity of murine myeloma protein-315 to enantiomeric spin labeled dinitrophenyl hapten. *Immunochemistry* **1974**, *11* (7), 377–379.
- (33) Chew, J.; Leypunskiy, E.; Lin, J.; Murugan, A.; Rust, M. J. High protein copy number is required to suppress stochasticity in the cyanobacterial circadian clock. *Nat. Commun.* **2018**, *9* (1), 3004.

(34) Kitayama, Y.; Iwasaki, H.; Nishiwaki, T.; Kondo, T. KaiB functions as an attenuator of KaiC phosphorylation in the cyanobacterial circadian clock system. *EMBO J.* **2003**, *22* (9), 2127–2134.

(35) Koda, S. I.; Saito, S. An alternative interpretation of the slow KaiB-KaiC binding of the cyanobacterial clock proteins. *Sci. Rep.* **2020**, *10* (1), 10439.

(36) Kageyama, H.; Nishiwaki, T.; Nakajima, M.; Iwasaki, H.; Oyama, T.; Kondo, T. Cyanobacterial circadian pacemaker: Kai protein complex dynamics in the KaiC phosphorylation cycle in vitro. *Mol. Cell* **2006**, *23* (2), 161–171.

(37) Welkie, D. G.; Rubin, B. E.; Chang, Y. G.; Diamond, S.; Rifkin, S. A.; LiWang, A.; Golden, S. S. Genome-wide fitness assessment during diurnal growth reveals an expanded role of the cyanobacterial circadian clock protein KaiA. *Proc. Natl. Acad. Sci. U. S. A.* **2018**, *115* (30), E7174–E7183.

(38) Terauchi, K.; Kitayama, Y.; Nishiwaki, T.; Miwa, K.; Murayama, Y.; Oyama, T.; Kondo, T. ATPase activity of KaiC determines the basic timing for circadian clock of cyanobacteria. *Proc. Natl. Acad. Sci. U. S. A.* **2007**, *104* (41), 16377–16381.

(39) Rust, M. J.; Golden, S. S.; O'Shea, E. K. Light-driven changes in energy metabolism directly entrain the cyanobacterial circadian oscillator. *Science* **2011**, *331* (6014), 220–223.

(40) Egli, M.; Pattanayek, R.; Sheehan, J. H.; Xu, Y.; Mori, T.; Smith, J. A.; Johnson, C. H. Loop-Loop Interactions Regulate KaiA-Stimulated KaiC Phosphorylation in the Cyanobacterial KaiABC Circadian Clock. *Biochemistry* **2013**, *52* (7), 1208–1220.

(41) Hammes, G. G.; Chang, Y.-C.; Oas, T. G. Conformational selection or induced fit: A flux description of reaction mechanism. *Proc. Natl. Acad. Sci. U. S. A.* **2009**, *106* (33), 13737–13741.

(42) Wang, J. Nucleotide-dependent domain motions within rings of the RecA/AAA(+) superfamily. *J. Struct. Biol.* **2004**, *148* (3), 259–267.

(43) Sysoeva, T. A. Assessing heterogeneity in oligomeric AAA+ machines. *Cell. Mol. Life Sci.* **2017**, *74* (6), 1001–1018.

(44) Vakonakis, I.; Sun, J.; Wu, T.; Holzenburg, A.; Golden, S. S.; LiWang, A. C. NMR structure of the KaiC-interacting C-terminal domain of KaiA, a circadian clock protein: implications for KaiA-KaiC interaction. *Proc. Natl. Acad. Sci. U. S. A.* **2004**, *101* (6), 1479–1484.

(45) Ye, S.; Vakonakis, I.; Ioerger, T. R.; LiWang, A. C.; Sacchettini, J. C. Crystal structure of circadian clock protein KaiA from *Synechococcus elongatus*. *J. Biol. Chem.* **2004**, *279* (19), 20511–20518.

(46) Vakonakis, I.; LiWang, A. C. Structure of the C-terminal domain of the clock protein KaiA in complex with a KaiC-derived peptide: implications for KaiC regulation. *Proc. Natl. Acad. Sci. U. S. A.* **2004**, *101* (30), 10925–10930.

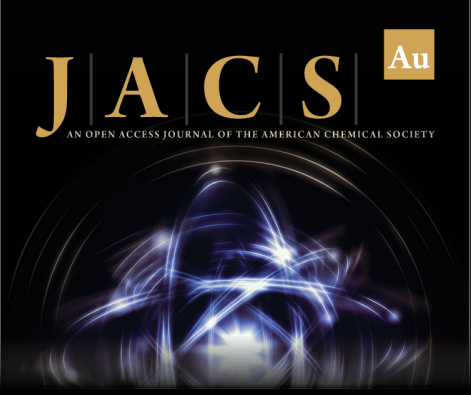
(47) Wood, T. L.; Bridwell-Rabb, J.; Kim, Y. I.; Gao, T.; Chang, Y. G.; LiWang, A.; Barondeau, D. P.; Golden, S. S. The KaiA protein of the cyanobacterial circadian oscillator is modulated by a redox-active cofactor. *Proc. Natl. Acad. Sci. U. S. A.* **2010**, *107* (13), 5804–5809.

(48) Holtzendorff, J.; Partensky, F.; Mella, D.; Lennon, J. F.; Hess, W. R.; Garczarek, L. Genome streamlining results in loss of robustness of the circadian clock in the marine cyanobacterium *Prochlorococcus marinus* PCC 9511. *J. Biol. Rhythms* **2008**, *23* (3), 187–199.


(49) Voss, B.; Bolhuis, H.; Fewer, D. P.; Kopf, M.; Möke, F.; Haas, F.; El-Shehawey, R.; Hayes, P.; Bergman, B.; Sivonen, K.; et al. Insights into the physiology and ecology of the brackish-water-adapted Cyanobacterium *Nodularia spumigena* CCY9414 based on a genome-transcriptome analysis. *PLoS One* **2013**, *8* (3), e60224.


(50) Axmann, I. M.; Hertel, S.; Wiegand, A.; Dörrich, A. K.; Wilde, A. Diversity of KaiC-based timing systems in marine Cyanobacteria. *Mar. Genomics* **2014**, *14*, 3–16.


(51) Axmann, I. M.; Dühring, U.; Seeliger, L.; Arnold, A.; Vanselow, J. T.; Kramer, A.; Wilde, A. Biochemical evidence for a timing mechanism in *prochlorococcus*. *J. Bacteriol.* **2009**, *191* (17), 5342–5347.



**JACS** Au  
AN OPEN ACCESS JOURNAL OF THE AMERICAN CHEMICAL SOCIETY

 Editor-in-Chief  
**Prof. Christopher W. Jones**  
Georgia Institute of Technology, USA

**Open for Submissions** 

pubs.acs.org/jacsau   
ACS Publications  
Most Trusted. Most Cited. Most Read.

## Supporting Information for

A Nighttime Edge Site Intermediate in the Cyanobacterial Circadian Clock Identified by  
EPR Spectroscopy

Gary K. Chow,<sup>1</sup> Archana G. Chavan,<sup>2</sup> Joel C. Heisler,<sup>3</sup> Yong-Gang Chang,<sup>2</sup> Ning Zhang,<sup>2</sup>  
Andy LiWang,<sup>3,4,5,6,\*</sup> R. David Britt<sup>1,\*</sup>

<sup>1</sup>Department of Chemistry, University of California, Davis, CA 95616

<sup>2</sup>School of Natural Sciences, <sup>3</sup>Chemistry and Chemical Biology, <sup>4</sup>Health Sciences  
Research Institute, and <sup>5</sup>Center for Cellular and Biomolecular Machines, University of  
California, Merced, CA 95343

<sup>6</sup>Center for Circadian Biology, University of California, San Diego, La Jolla, CA 92093.

\*To whom correspondence should be addressed.

**Email:** A.L.: [aliwang@ucmerced.edu](mailto:aliwang@ucmerced.edu). R.D.B.: [rdbritt@ucdavis.edu](mailto:rdbritt@ucdavis.edu)

## Contents

1	Supporting Text .....	5
1.1	Estimation of the spectra of $B_+$ and $B_-$ .....	5
1.2	Evaluation of the mechanism of KaiB-KaiC binding .....	6
2	Methods .....	7
2.1	Cloning, protein expression, purification, and fluorescence / spin labeling .....	7
2.2	Protein characterization .....	7
2.3	In vitro Kai protein reactions sample preparations .....	7
2.4	$^1\text{H-NMR}$ based ATPase assays .....	7
2.5	cw-EPR spectroscopy .....	8
2.6	cw EPR data preprocessing .....	8
2.7	Quantitative cw EPR via change-of-basis from surrogate basis .....	9
2.7.1	(I) Spectral model .....	9
2.7.2	(II) Spectral model with nonnegativity constraint .....	10
2.7.3	Solutions to multiobjective optimization .....	10
2.8	Fitting of kinetic data to models .....	11
3	Supplementary Figures and Tables .....	12
3.1	$\text{K25C}_{3\text{IAP}}$ is a functional surrogate of WT-KaiB .....	12
	<b>Fig. S1.</b> Intact LCMS of $\text{K25C}_{3\text{IAP}}$ shows complete spin labeling .....	12
	<b>Fig. S2.</b> Fluorescence anisotropy assay on functionality of $\text{K25C}_{3\text{IAP}}$ in the in vitro oscillator. ....	13
	<b>Fig. S3.</b> Native-PAGE analysis of WT-KaiB and $\text{K25C}_{3\text{IAP}}$ binding to KaiC <sub>EE</sub> . ....	14
3.2	cw-EPR of $\text{K25C}_{3\text{IAP}}$ distinguishes two populations of KaiC-bound KaiB .....	15
	<b>Fig. S4.</b> $\text{K25C}_{3\text{IAP}}$ displays at least two motional dynamics state. ....	15
	<b>Table S1.</b> Summary of best fit motional parameters for free $\text{K25C}_{3\text{IAP}}$ . ....	16
	<b>Fig. S5.</b> Two components are insufficient to explain $\text{K25C}_{3\text{IAP}}$ -KaiC <sub>EE</sub> reaction spectra. ....	17
	<b>Fig. S6.</b> $\text{K25C}_{3\text{IAP}}$ -KaiCI reaction spectra at stoichiometric and 1:10 excess KaiC <sub>EE</sub> ratios. ....	18
	<b>Table S2.</b> Estimation of KaiB-CI direct binding dissociation constant. ....	19
	<b>Fig. S7.</b> $\text{K25C}_{3\text{IAP}}$ is insensitive to direct KaiA-KaiB interactions. ....	20
3.3	Estimation of cw-EPR spectra of $B_+$ and $B_-$ .....	21
	<b>Fig. S8.</b> Surrogate basis spectra ( $B^*$ ) and their respective proxy weights/concentrations ( $w^*$ ). ....	21
	<b>Fig. S9.</b> Unconstrained single-component fitting of $\text{K25C}_{3\text{IAP}}$ -KaiC <sub>EE</sub> reaction spectra. ....	22
	<b>Fig. S10.</b> Unconstrained two-component fitting of $\text{K25C}_{3\text{IAP}}$ -KaiC <sub>EE</sub> reaction spectra. ....	23
	<b>Table S3.</b> Summary of single-objective best fit motional parameters for $B_+$ and $B_-$ . ....	24
	<b>Fig. S11.</b> Multiobjective optimization-based determination of change-of-basis matrix $R$ using a single nitroxide mobility component per species: $\lambda$ dependence. ....	26
	<b>Table S4.</b> Summary of $\lambda$ -dependent best fit motional parameters using a single nitroxide mobility component per species derived from one replicate dataset. ....	26
	<b>Fig. S12.</b> Multiobjective optimization-based determination of change-of-basis matrix $R$ using two nitroxide mobility components per species: $\lambda$ dependence. ....	28

<b>Table S5.</b> Summary of $\lambda$ -dependent best fit motional parameters using two nitroxide mobility component per species derived from one replicate dataset. ....	28
<b>Fig. S13.</b> Multiobjective optimization-based determination of change-of-basis matrix $R$ using one nitroxide mobility component per species in second technical replicate. ....	29
<b>Fig. S14.</b> Multiobjective optimization-based determination of change-of-basis matrix $R$ using two nitroxide mobility components per species in second technical replicate. ....	30
<b>Fig. S15.</b> Multiobjective optimization-based determination of change-of-basis matrix $R$ using one nitroxide mobility component per species in third technical replicate. ....	31
<b>Fig. S16.</b> Multiobjective optimization-based determination of change-of-basis matrix $R$ using two nitroxide mobility components per species in third technical replicate. ....	32
<b>Table S6.</b> Summary of multiobjective optimization based best fit motional parameters of $B_+$ and $B_-$ in replicate datasets. ....	33
<b>Fig. S17.</b> Summary of spectral fit of $B_+$ and $B_-$ and associated kinetics. ....	34
<b>Fig. S18.</b> Determination of fictitious KaiC-bound KaiB populations. ....	35
3.4 $B_-$ is an intermediate between $B_+$ and free KaiB. ....	36
<b>Fig. S19.</b> Overlay of $dB_+/dt$ and $B_-$ in $K25C_{3IAP}$ -KaiC <sub>ST/EE/EA</sub> reactions. ....	36
<b>Fig. S20.</b> Spectral simulations of $K25C_{3IAP}$ -KaiC <sub>ST/EE/EA</sub> reactions. ....	37
<b>Fig. S21.</b> The Koda-Saito model does not adequately explain the observed KaiB-KaiC binding kinetics. ....	39
<b>Table S7.</b> Rate constants derived from the basic Koda-Saito model. ....	40
<b>Fig. S22.</b> Koda-Saito with monomeric KaiB fold switching. ....	41
<b>Table S8.</b> Rate constants derived from the Koda-Saito model with monomeric KaiB fold switching. ....	41
<b>Fig. S23.</b> Koda-Saito with tetramer-dimer-monomer KaiB equilibrium. ....	42
<b>Table S9.</b> Rate constants derived from the Koda-Saito model with tetramer-dimer-monomer KaiB equilibrium. ....	42
<b>Fig. S24.</b> Koda-Saito with KaiC conformational equilibrium. ....	43
<b>Table S10.</b> Rate constants derived from the Koda-Saito model with KaiC conformational equilibrium. ....	43
<b>Fig. S25.</b> Koda-Saito with KaiB fold switching equilibrium and KaiC conformational equilibrium. ....	44
<b>Table S11.</b> Rate constants derived from the Koda-Saito model with KaiB fold switching equilibrium and KaiC conformational equilibrium. ....	44
<b>Fig. S26.</b> Koda-Saito with KaiB-KaiC nucleation-induced KaiC activation model. (a) Koda-Saito model with KaiB-KaiC nucleation-induced KaiC activation model. ....	45
<b>Table S12.</b> Rate constants derived from the Koda-Saito with KaiB-KaiC nucleation-induced KaiC activation model. ....	45
<b>Table S13.</b> Rate constants derived from the Koda-Saito model coupled with KaiB-KaiC encounter complex formation and induced fit nucleation. ....	46
<b>Fig. S27.</b> Hyperphosphorylated KaiC is more competent in KaiB-KaiC binding nucleation than unphosphorylated or S431-phosphorylated KaiC. ....	47
<b>Table S14.</b> Bootstrap resampling derived KaiB-KaiC dissociation constants. ....	49

3.5	KaiC <sub>spT</sub> is ineffective at seeding KaiB-KaiC interactions during the day-to-night transition .....	50
	<b>Fig. S28.</b> KaiB-KaiC <sub>AE</sub> binding requires the presence of KaiA.....	50
	<b>Fig. S29.</b> KaiA drives KaiB-KaiC <sub>AE</sub> interactions by multiple mechanisms.....	52
3.6	KaiA triggers the night-to-day transition by antagonizing KaiB-KaiC <sub>pST</sub> interactions.....	54
	<b>Fig. S30.</b> cw-EPR derived kinetics of KaiB-KaiC <sub>EE/EA</sub> binding when exposed to KaiA.....	54
	<b>Fig. S31.</b> Spectral simulations of K25C <sub>3IAP</sub> -KaiC <sub>EE/EA</sub> reactions with KaiA spiking.....	55
	<b>Fig. S32.</b> B <sub>-</sub> formation is linearly correlated with B <sub>+</sub> degradation on KaiA-induced antagonization of KaiB-KaiC <sub>EA</sub> interactions.....	56
	<b>Fig. S33.</b> The C-terminal domain of KaiA is most effective in antagonizing KaiB-KaiC <sub>EA</sub> interactions.....	57
3.7	Interconversion of B <sub>-</sub> and B <sub>+</sub> in the Kai oscillator .....	58
	<b>Fig. S34.</b> cw-EPR of K25C <sub>3IAP</sub> oscillator.....	58
	<b>Fig. S35.</b> Reproducibility of reconstituted K25C <sub>3IAP</sub> oscillators.....	59
	<b>Fig. S36.</b> Spectral simulations of the K25C <sub>3IAP</sub> reconstituted in vitro oscillator. ....	60
	<b>Fig. S37.</b> Fit of dynamics of subpopulations of KaiC-bound KaiB to sum of cosines (MFourFit) using 1-4 cosines.....	61
	<b>Table S15.</b> mFourfit parameters of K25C <sub>3IAP</sub> 5× oscillator.....	62
4	References for Supporting Information .....	65



## 1 Supporting Text

### 1.1 Estimation of the spectra of B<sub>+</sub> and B<sub>-</sub>

We previously demonstrated the use of cw-EPR in quantifying the fraction of KaiC-bound KaiB using N19C<sub>3IAP</sub> by determining the spectrum of KaiC-bound KaiB under saturating conditions.<sup>1</sup> Unlike our previous work, pure B<sub>+</sub> and B<sub>-</sub> in the absence of free KaiB could not be obtained without further manipulating the KaiB construct and/or sample preparation which could lead to loss of function or generalizability. Instead, the real-time cw-EPR data were interpreted by estimating the spectra of B<sub>+</sub> and B<sub>-</sub> via spectral simulations (Fig. S8-S17). We used the spectrum of free KaiB and the binned spectra ( $t = 15-18$  hrs) of 1:1 KaiB-KaiC<sub>EE</sub> (dominated by B<sub>+</sub>) and 1:10 KaiB-KaiC<sub>EE</sub> (dominated by B<sub>-</sub>) as our proxy spectra (Fig. S8). Direct fitting with the Naïve spectral model (Methods Section 2.7, eq. 4.1) of the spectra to the Brownian motion model<sup>2</sup> with a single nitroxide component describing either B<sub>+</sub> or B<sub>-</sub> led to negative B<sub>-</sub> kinetics in the stoichiometric K25C<sub>3IAP</sub>-KaiC<sub>EE</sub> reaction (Fig. S9). Expansion of the parameter search space to incorporate two motional components for each of B<sub>+</sub> and B<sub>-</sub> akin to free K25C<sub>3IAP</sub> (Fig. S4) resulted in negative B<sub>+</sub> kinetics in the K25C<sub>3IAP</sub>-KaiC<sub>EE</sub> reaction with excess KaiC<sub>EE</sub> (Fig. S10). Although these observations hinted at oversimplification of the Brownian motion model, they also revealed the lack of physical constraints in the basic fit-and-quantify strategy, a problem that we deemed will likely persist on further parameter search space expansion even if more sophisticated motional models are employed.

To introduce nonnegative constraints to the data analysis, a modified fitting procedure was developed to explicitly penalize negative kinetics (eq. 4.2 and Figs. S11-16). Spectral fits that led to negative kinetics were penalized based on the magnitude of the negative kinetics they produced. The spectral fit residual and the negative kinetics penalty constituted a multiobjective optimization problem that required a compromise between the two objectives<sup>3</sup> that could be resolved by finding the “corner”<sup>4</sup> or closest-to-origin point<sup>5</sup> on the Pareto front. This compromise is quantified by a scaling factor,  $\lambda$ , that reduces the optimization problem to a single objective at either  $\lambda = 0$  or  $\infty$ . Using this strategy, we estimated the spectra of B<sub>+</sub> and B<sub>-</sub> as shown in Fig. S17a and their respective kinetics in partial reactions with unphosphorylated KaiC as well as KaiC phosphomimetics (Fig. S17b). Importantly, these penalized spectral fits no longer produced kinetic fits that had statistically significant excursions into negative concentrations. We note that the multiobjective optimization procedure led to fictitious levels of KaiC-bound KaiB populations in KaiC-free control experiments (Fig. S18) that could explain the apparent nonzero binding observed in K25C<sub>3IAP</sub>-KaiC<sub>AE</sub> experiments. This minimal KaiB-KaiC<sub>AE</sub> association is consistent with previous fluorescence anisotropy experiments.<sup>6</sup> Nevertheless, the ability to interpret real-time cw-EPR data to obtain physically plausible kinetics affords additional insight by enabling comparison against kinetic models.

## 1.2 Evaluation of the mechanism of KaiB-KaiC binding

To evaluate the mechanism underlying KaiB-KaiC binding, we considered a total of 7 models. A summary and description of individual models is provided here for reference:

- i. Fig. S21 and Table S7 described the Koda-Saito model in which KaiC was assumed to possess 6 independent sites for binding to monomeric KaiB. There were  $2^6 = 64$  states of KaiBC complexes ranging from  $B_0C_6$  to  $B_6C_6$ . The  $k_{on}$  was independent for all binding events whereas  $k_{off}$  was dependent on the number of adjacent KaiC-bound KaiB. This model was identical to the original publication by Koda and Saito (2020).<sup>7</sup>
- ii. Fig. S22 and Table S8 described the addition of KaiB fold-switching to model (i). The fold switching is implemented by assuming that KaiB is in equilibrium between two forms, gs-KaiB and fs-KaiB, that are spectroscopically equivalent and switches between the two folds at rates described by two rate constants. Only fs-KaiB is capable of binding to KaiC.
- iii. Fig. S23 and Table S9 described the addition of KaiB monomerization to model (i). KaiB was assumed to exist as a combination of tetramers, dimers and monomers in solution that are spectroscopically indistinguishable from one another. Its interconversion is described by four rate constants. Only the monomer is capable of binding to KaiC.
- iv. Fig. S24 and Table S10 described the addition of KaiC conformational equilibrium to model (i). This model assumed that  $KaiB_0C_6$  existed as two states,  $C_{B-incomp}$  and  $C_{B-comp}$  that are respectively incompetent and competent to KaiB binding, resulting in a total of  $2^6+1 = 65$  possible states of KaiBC complexes. The interconversion between  $C_{B-incomp}$  and  $C_{B-comp}$  is described by two rate constants.
- v. Fig. S25 and Table S11 described the addition of both KaiB fold-switching (v) and KaiC conformational equilibrium (iv) to the model (i).
- vi. Fig. S26 and Table S12 described the modification of model (i) to allow the nucleation event ( $B_{free} + C_6 \rightleftharpoons B_1C_6$ ) to possess different  $k_{on}$  and  $k_{off}$  from subsequent binding/dissociation events. The biochemical justification for this difference is that the first binding event “locks” or activates KaiC into a KaiB-binding competent state once nucleation occurs. This model adds two parameters to model (i).
- vii. Fig. 3 and Table S13 described the encounter complex model shown in the main text. In addition to the  $2^6$  states of KaiBC ( $B_0C_6$  to  $B_6C_6$ ) as in (i), we introduced the  $B_1C_6$  encounter complex denoted as  $BC_{inactive}$  in Fig. 3b. The total number of BC complexes from  $B_0C_6$  to  $B_6C_6$  is then  $2^6+6 = 70$ . We assumed that KaiB in the encounter complex was spectroscopically indistinguishable from free KaiB. This model required 4 additional rate constants to describe respectively the rate of encounter complex formation/dissociation and interconversion between the encounter complex and stably bound  $KaiB_1C_6$  state.

## 2 Methods

### 2.1 Cloning, protein expression, purification, and fluorescence / spin labeling

All genes were cloned into pET-28b using the NdeI/HindIII restriction sites for production of SUMO-fusion proteins. The pET-28b plasmids harboring the *kaiA*, *kaiB* and *kaiC* genes were used to transform *Escherichia coli* BL21 (DE3) cells (Novagen). Details of the cloning,<sup>8</sup> expression, purification<sup>9</sup> and fluorescence<sup>10</sup> / spin labelling<sup>1</sup> protocols have been described previously.

### 2.2 Protein characterization

The concentrations of all protein stock solutions were determined by Bradford assay using bovine serum albumin (ThermoFisher) as a concentration standard. All concentrations refer to the monomer unless otherwise stated. Labeling efficiency of KaiB-K25C-3IAP (K25C<sub>3IAP</sub>) was determined by electrospray ionization high resolution liquid chromatography mass spectrometry (ESI-HR-LCMS) using an LTQ Orbitrap XL mass spectrometer equipped with an electrospray ionization source (ThermoFisher, San Jose, CA) operating in positive ion mode. Details have been described previously.<sup>1</sup>

### 2.3 In vitro Kai protein reactions sample preparations

All reactions were performed at 30°C in reaction buffer (20 mM Tris, 150 mM NaCl, pH 8.0, 0.5 mM EDTA, 5 mM MgCl<sub>2</sub> and 1 mM ATP). The in vitro 1× oscillator was carried out using 1.2 μM KaiA, 3.5 μM KaiB and 3.5 μM KaiC and that of 5× reactions were scaled accordingly without adjusting ATP concentration. Fluorescence samples at 1× protein concentrations were prepared as 100 μL samples with an additional 50 nM of KaiB-K25C-6IAF included as described previously.<sup>10</sup> For real-time cw-EPR characterization, 20–40 μL samples at 5× protein concentrations were prepared by replacing WT-KaiB with spin labeled KaiB. For NMR samples at 5× protein concentrations, solutions were prepared to contain a final concentration of 5% D<sub>2</sub>O and 10 μM DSS. Unphosphorylated KaiC (KaiC<sub>ST</sub>) was prepared by incubating WT-KaiC at 30°C for 48 hours whereas KaiC<sub>S431E,T432E</sub> (KaiC<sub>EE</sub>), KaiC<sub>S431E,T432A</sub> (KaiC<sub>EA</sub>) and KaiC<sub>S431A,T432E</sub> (KaiC<sub>AE</sub>) were used as purified. Evaluation of the effect of KaiA on KaiB-KaiC binding was done by spiking KaiA to the reaction mixture at  $t = 24$  hours after equilibration of the KaiB-KaiC mixture. Native-PAGE samples were prepared as 200 μL reaction mixtures at 1× protein concentration and incubated at 30°C for 0 hours to overnight. Details of Native-PAGE sample preparation, electrophoresis, staining and imaging procedures have been described previously.<sup>1</sup>

### 2.4 <sup>1</sup>H-NMR based ATPase assays

One-dimensional proton NMR spectra were measured at 30°C every 2 minutes for 2 days, all NMR data were processed with NMRPipe.<sup>11</sup> The ATP and ADP peak were fit using a parabolic interpolation function. Peak intensities were normalized to total peak intensities and plotted as a function of time. ATPase activity pre-KaiA spiking was determined by linear regression.

## 2.5 cw-EPR spectroscopy

X-band (9.2 GHz) spectra were collected using a Bruker ECS 106 spectrometer equipped with an SHQE cavity as previously described.<sup>1</sup> The sample temperature was controlled using an FTS XR401 Air-jet Crystal Cooler (SP Scientific, Stone Ridge, NY) and monitored by an external type T thermocouple (Omega Inc., CT) connected to a Universal Thermocouple Connector Direct USB to PC Connection (Omega Inc., CT). Microwave frequency was continuously monitored externally via an EIP 578B frequency counter (National Instruments, Santa Clara, CA).

## 2.6 cw EPR data preprocessing

EPR data were preprocessed by microwave frequency drift correction and background subtraction as described previously.<sup>1</sup> For quantitative cw-EPR, “*B*-shift” correction was accounted for by solving the nonlinear least squares problem

$$Y_t = \text{shift} \left[ \sum_{i=1}^r \text{shift}(B_i w_{it}, s_i), s_t \right] + \varepsilon \dots (1.1)$$

as previously described where  $Y_t$  is the real-time cw-EPR data,  $B_i$  is the EPR spectra of the  $i^{\text{th}}$  component out of a total of  $r$  components,  $w_i$  is the weight of the  $i^{\text{th}}$  component,  $s_i$  is the spectrum-dependent “*B*-shift”,  $s_t$  is the time-dependent “*B*-shift” and  $\varepsilon$  represents noise. To solve (1.1), experimental spectra at various timepoints  $Y_{t=t_x}$  and/or across multiple datasets can be used as surrogates ( $B^*$ ) for  $B_i$ . This treatment isolates “*B*-shift” from weight/concentration consideration. Further analysis will assume that “*B*-shift” is no longer present and that the data  $Y$  consisting of  $n_t$  spectra collected at 1024 magnetic field positions can be written as

$$Y_{1024 \times n_t} = B_{1024 \times r} w_{r \times n_t} + \varepsilon_{1024 \times n_t} \dots (1.2)$$

As pointed out previously,<sup>1</sup> double integration to scale  $B_i$  is avoided due to susceptibility to noise.<sup>12</sup> In the two-component system seen in N19C<sub>3IAP</sub>,  $B_{\text{free}} (= B_1)$  was scaled via a scaling factor  $\theta$  for quantification purposes. The scaling equation can be extended to accommodate an  $r$ -component system by replacing  $\theta$  with  $\theta_i$  for the  $(r - 1)$  components to be scaled:

$$Y_{r\text{-component}} = (B_1 \quad B_{2u} \quad \dots)_{1024 \times r} \begin{pmatrix} w_1 \\ \theta_2 w_2 \\ \vdots \\ w_r \end{pmatrix}_{r \times n_t} \dots (2.1)$$

where  $u$  subscript in  $B_{iu}$  refers to the unscaled spectrum of the  $i^{\text{th}}$  component.

Concentration conservation of spin labeled KaiB gives

$$w_1 + \theta_2 w_2 + \dots + \theta_r w_r = C \leftrightarrow \theta_2 w_2 + \dots + \theta_r w_r - C = -w_1 \dots (2.2)$$

for some constant  $C$  that is dataset specific. Rewriting (2.2) in matrix form,

$$(\theta_2 \quad \dots \quad \theta_r \quad C)_{1 \times r} \begin{pmatrix} w_2 \\ \vdots \\ w_r \\ -1 \end{pmatrix}_{r \times n_t} = (-w_1)_{1 \times n_t} \dots (2.3)$$

Equation (2.3) can be solved directly. Alternatively, information from  $m$  datasets each with their respective data lengths  $n_j$  and conservation constants  $C_j$ , ( $j = 1 \dots m$ ) can be incorporated simultaneously:

$$\begin{aligned}
& (\theta_2 \cdots \theta_r \ C_1 \cdots C_m)_{1 \times (r+m-1)} \begin{pmatrix} W_{2,\text{set } 1} & W_{2,\text{set } 1} & \cdots & W_{2,\text{set } m} \\ \vdots & \vdots & \vdots & \vdots \\ W_{r,\text{set } 1} & W_{r,\text{set } 2} & \cdots & W_{r,\text{set } m} \\ -\mathbf{1}_{1 \times n_1} & 0 & \cdots & 0 \\ 0 & -\mathbf{1}_{1 \times n_2} & \cdots & 0 \\ \vdots & \vdots & \ddots & \vdots \\ 0 & 0 & 0 & -\mathbf{1}_{1 \times n_m} \end{pmatrix} \\
& = (-w_{1,\text{set } 1} \cdots -w_{1,\text{set } m})_{1 \times \sum n_t} \dots (2.4)
\end{aligned}$$

$$(r+m-1) \times \sum n_t$$

The scaled spectra  $B_2 \dots B_r$  in equation (1.2) can then be determined by solving for  $\theta_2 \dots \theta_r$  as a linear regression problem. After scaling,  $w$  can be solved again for the correctly scaled weights.

## 2.7 Quantitative cw EPR via change-of-basis from surrogate basis

The weights determined above using experimental spectra at various timepoints  $Y_{t=tx}$  and/or across multiple datasets as surrogates ( $B^*$ ) to  $B_i$  only give rise to proxy weights/concentrations  $w^*$  (see Fig. S8). Specifically, the true spectra ( $B$ ) and weight ( $w$ ) of the components can be related to the surrogate spectra  $B^*$  via a change-of-basis matrix  $R_{r \times r}$ :

$$Y = B_{1024 \times r} w_{r \times n_t} = (BR)_{1024 \times r} (R^{-1}w)_{r \times n_t} = B^* w^* \dots (3.1)$$

$$B = B^* R^{-1}; w = R w^* \dots (3.2)$$

There are two rationales that constrain the elements of  $R$ : (i)  $B_{\text{free}} = B_1$  should not be changed and (ii)  $\sum w_i$  is constant after change of basis. (i) is satisfied when  $R_{11} = 1$  and  $R_{i1} = 0$  for  $i > 1$ . (ii) is satisfied when  $\sum_i^r R_{ij} = 1$ . Hence,  $R$  has the following structure:

$$R = \begin{pmatrix} 1 & R_{12} & \cdots & R_{1r} \\ 0 & R_{22} & \cdots & R_{2r} \\ \vdots & \vdots & \ddots & \vdots \\ 0 & 1 - R_{12} - R_{22} - \dots & \cdots & 1 - R_{1r} - R_{2r} - \dots \end{pmatrix}_{r \times r} \dots (3.3)$$

This leaves  $R$  with  $(r-1)^2$  unknown elements. Further analysis can be divided into two classes: (I) Naïve spectral model and (II) Spectral model with nonnegativity constraint.

### 2.7.1 (I) Spectral model

In the naïve spectral model, the elements of  $R$  are further constrained by the assumption that  $B = B^* R^{-1}$  represents the true spectra of spin labeled species. Consequently,  $B$  can be modeled via spectral simulations by solving the Stochastic Liouville Equation (SLE) for nitroxide radicals with some motional parameters  $P$  given the experimental parameters  $\text{Exp}$ . The corresponding objective function is then

$$\text{argmin}_{R,P} \varepsilon_s = \frac{\sum |B^* R^{-1} - \text{SLE}(P, \text{Exp})|^2}{\sum |B^* R^{-1}|^2} \dots (4.1)$$

$\varepsilon_s$  is then interpreted as spectral error and measures how well the cw-EPR spectra fit to those simulated from the given spin parameters. There exist multiple motional models (e.g. Brownian motion,<sup>2</sup> slowly relaxing local structure<sup>13</sup>) to simulate nitroxide spectra. The Brownian motion model<sup>2</sup> was chosen in this work due to its relative ease of computation and implemented with the MATLAB (Natick, MA) EPR simulations package EasySpin<sup>14</sup> via the function `chili`. Each nitroxide component spectrum was assumed to be described by 3 rotational correlation times ( $\tau$ ) and Gaussian and Lorentzian linewidths ( $\Gamma$ ), resulting in 5 variables per component. If  $k$  nitroxide components are necessary to describe a single species, the number of variables increases to  $6k - 1$  to account for non-unity weight of the 2<sup>nd</sup> to  $k^{\text{th}}$  components. Values of  $k = 1$  and 2 were used in this study, corresponding to respectively a single (Fig. S9a) or two nitroxide component(s) (Fig. S10a) per cw-EPR-distinguishable component.

### 2.7.2 (II) Spectral model with nonnegativity constraint

In practice, (I) could lead to overfitting of the data to the assumed nitroxide spin model and negative values of  $w$  as predicted by eq. (3.2) (also see Fig. S8-9b-c). As  $w$  represents the true concentration of underlying species and thus cannot have negative values, a penalty is imposed on the fitting procedure to penalize values of  $R$  that lead to negative  $w$ , resulting in the spectral model with nonnegativity constraint (II). The corresponding objective function is

$$\operatorname{argmin}_{R,P} \begin{cases} \varepsilon_s = \frac{\sum |B^* R^{-1} - \text{SLE}(P, \text{Exp})|^2}{\sum |B^* R^{-1}|^2} \dots(4.2) \\ \lambda \varepsilon_n = \lambda \sum |(Rw^* < 0)|^2 \end{cases}$$

The added objective  $\varepsilon_n$  corresponds to negative concentration penalty. The prefactor  $\lambda$  is treated as an adjustable weight parameter as both constraints are not strictly correct due to respectively imperfect modeling and noise-induced excursion of  $w$  into small negative values during quantification due to noise. For the fit, experimental triplicate values of  $B^*$  and  $w^*$  obtained from 1:1 K25C<sub>3IAP</sub>-KaiC<sub>EE</sub>, 1:10 K25C<sub>3IAP</sub>-KaiC<sub>EE</sub> and 1:1 K25C<sub>3IAP</sub>-KaiC<sub>EA</sub> experiments were used.

### 2.7.3 Solutions to multiobjective optimization

There exist two objectives for class (II) data analyses. In general, optimization problems with multiple objectives cannot be simultaneously optimized. A decrease in  $\varepsilon_s$  leads to an increase in  $\varepsilon_n$  and vice versa and the system forms a Pareto front.<sup>3</sup> To determine the best solution that forms a compromise between the two objectives, the objective functions in eqs. (4.2) can be scalarized to a single objective function:<sup>3</sup>

$$\text{(II):argmin}_{R,P} [\varepsilon_s(R,P) + \lambda \varepsilon_n(R)] \dots(5.1)$$

$\varepsilon_s$  and  $\varepsilon_n$  can be computed at each value of  $\lambda$  to generate the Pareto front when  $\varepsilon_s$  and  $\varepsilon_n$  are plotted against one another in a log-log plot of coordinates

$$(x,y) = (\log_{10} \varepsilon_s(\lambda), \log_{10} \varepsilon_n(\lambda)) \dots(5.2)$$

Two strategies are employed to determine the best compromise (“nadir-utopia point”) between the two objectives. The first approach was described by Cohan et al.<sup>5</sup> and is based on the generation of a “utopia point” by means of “anchor points” where only one of the two objectives are optimized irrespective of the other ( $\lambda \rightarrow 0$  and  $\lambda \rightarrow \infty$ ). The

Euclidean distance between the utopia point and points on the curve can be computed.  $\lambda$  is then chosen by finding the minimum distance for the “nadir-utopia point”. In the second approach, the corner of the Pareto front is computed by computing the curvature  $\kappa$ .  $\lambda$  is then chosen by finding the maximum curvature  $\kappa_{\max}$ .<sup>4</sup> Both procedures are analogous to the  $L$ -curve criterion implemented in regularization.<sup>15</sup>

Both approaches to determine  $\lambda$  and their respective change-of-basis matrices  $R$  were collected. This procedure was repeated using both a single nitroxide mobility component ( $k = 1$ ) and two mobility components ( $k = 2$ ) per species, resulting in four change-of-basis matrices and four spectral estimates  $B^*R^{-1}$  per [1:1 K25C<sub>3IAP</sub>-KaiC<sub>EE</sub>, 1:10 K25C<sub>3IAP</sub>-KaiC<sub>EE</sub> and 1:1 K25C<sub>3IAP</sub>-KaiC<sub>EA</sub>] technical replicate dataset. This procedure was repeated with two other replicates (three technical replicates), resulting in a total of twelve spectral estimates of  $B$ . Uncertainty in quantification were propagated using these twelve spectral estimates by assuming that the intra-dataset uncertainty ( $s_{\text{intra}}$ ) originating from spin modeling and inter-dataset uncertainty ( $s_{\text{inter}}$ ) originating from inter-sample variability are independent of one another:

$$f = \bar{f} \pm \sqrt{(t_{0.975, df=4} s_{\text{intra}})^2 + (t_{0.975, df=3} s_{\text{inter}})^2 + (z_{0.975} \sigma_{S/N})^2} \dots (6.1)$$

where  $\bar{f}$  is the best estimate for  $f$ ,  $t_{0.975, df}$  and  $z$  are respective  $t$ - and  $z$ -values for 95% confidence with  $df$  refers to the degrees of freedom in the evaluation of  $R$ .  $\sigma_{S/N}$  refers to uncertainty due to imperfect signal-to-noise. Eq. (6.1) is used in the uncertainty reported in Fig. S17. For experiments where inter-experiment comparisons are of interest (Fig. 3-6), results from the mean of all models are taken. The inter-model uncertainty is ignored, and the reported fractions are

$$f_{n=1} = \bar{f} \pm z_{0.975} \sigma_{S/N} \dots (6.2)$$

for single-trial experiments and

$$f_{n>1} = \bar{f} \pm t_{0.975, df=n-1} s_{\text{rep}} \dots (6.3)$$

for experiments with multiple technical replicates where  $s_{\text{rep}}$  refers to the inter-replicate SEM.

## 2.8 Fitting of kinetic data to models

KaiB-KaiC binding kinetics predicted by models described in the main text are solved numerically by MATLAB (Natick, MA) function ode45. Rate constants were determined via coupling ode45 with the least squares solver lsqnonlin.

### 3 Supplementary Figures and Tables

#### 3.1 $K25C_{3IAP}$ is a functional surrogate of WT-KaiB

SPECTRUM - MS, 6833\_K25C.raw, FTMS + p ESI Full ms [110.00-2000.00], Scan #: 41-1402, RT: 0.32-9.99, AV: 1362, m/zIntensityRelative, NL: 1.40e+006 S/N: 70

Center	Area	Width
12603.1	92.35%	14.51
12625.1	1.75%	6.14
12372.3	2.34%	9.13
12642.0	3.57%	15.00

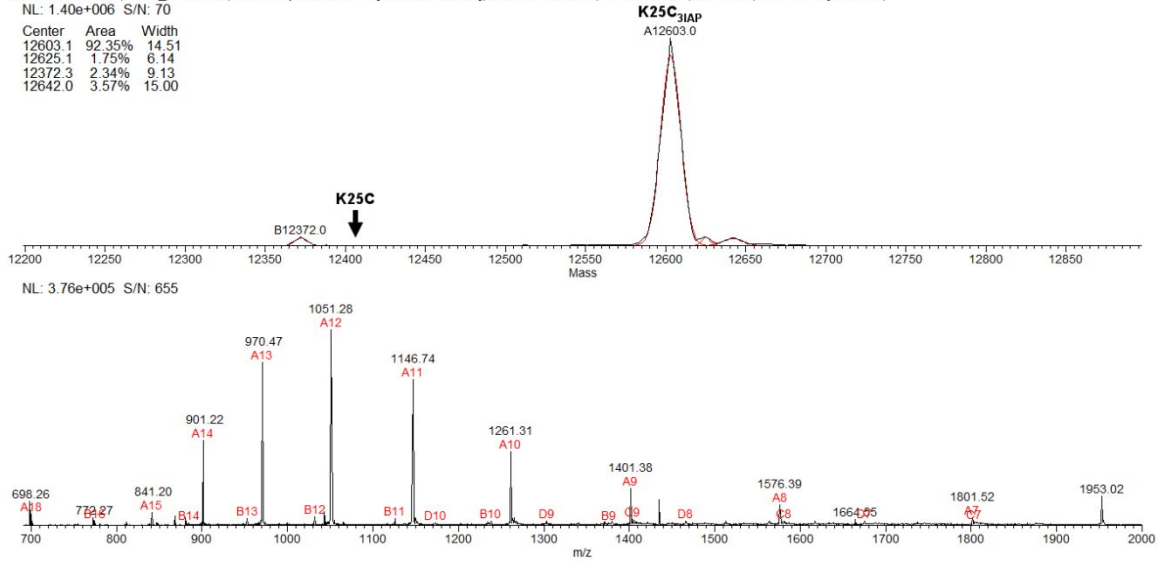


**Fig. S1.** Intact LCMS of  $K25C_{3IAP}$  shows complete spin labeling.

Top: transformed spectrum. Bottom: raw spectrum. LCMS masses:  $K25C_{3IAP}$  (Calc: 12603.6; Found: 12603.1).



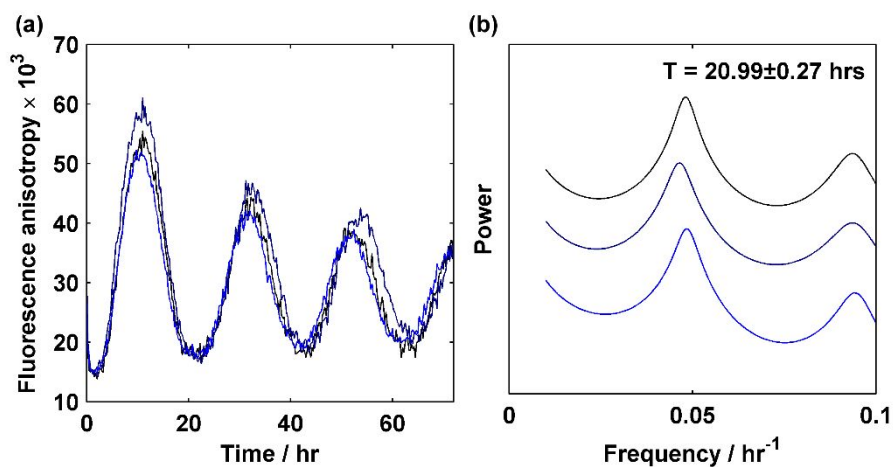


**Fig. S2.** Fluorescence anisotropy assay on functionality of K25C<sub>3IAP</sub> in the in vitro oscillator.

(a) Real-time fluorescence anisotropy traces of  $1 \times$  oscillator reactions using K25C<sub>3IAP</sub> (3.5  $\mu$ M) as a surrogate of WT-KaiB and 50 nM KaiB-K25C-6IAF as the fluorescence probe. The three traces of varying brightness show results from technical triplicates. (b) Corresponding periodograms computed using maximum entropy spectral analysis (MESA) with the mean and SEM of the periods shown ( $n = 3$ ).

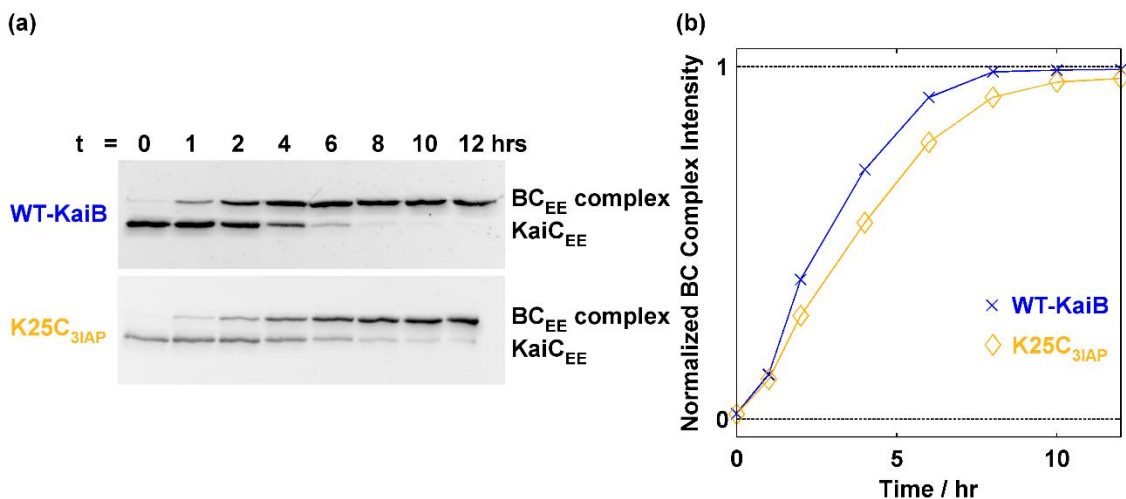


**Fig. S3.** Native-PAGE analysis of WT-KaiB and K25C<sub>3IAP</sub> binding to KaiC<sub>EE</sub>.

(a) Native-PAGE of samples collected at various time points from initial mixing of KaiB and KaiC<sub>EE</sub> as indicated on top of the images. Only KaiC-containing bands are shown. Species assignment is shown on the right. (b) KaiB-KaiC<sub>EE</sub> complexation estimated by densitometry. Traces refer to WT-KaiB (blue crosses) and K25C<sub>3IAP</sub> (yellow diamonds). The WT-KaiB data has previously been published in *Biochemistry*<sup>1</sup> (accessible at <https://pubs.acs.org/doi/10.1021/acs.biochem.0c00279>) and is reproduced here for comparison. Further permissions related to the material excerpted should be directed to the ACS.

### 3.2 cw-EPR of $K25C_{3IAP}$ distinguishes two populations of KaiC-bound KaiB

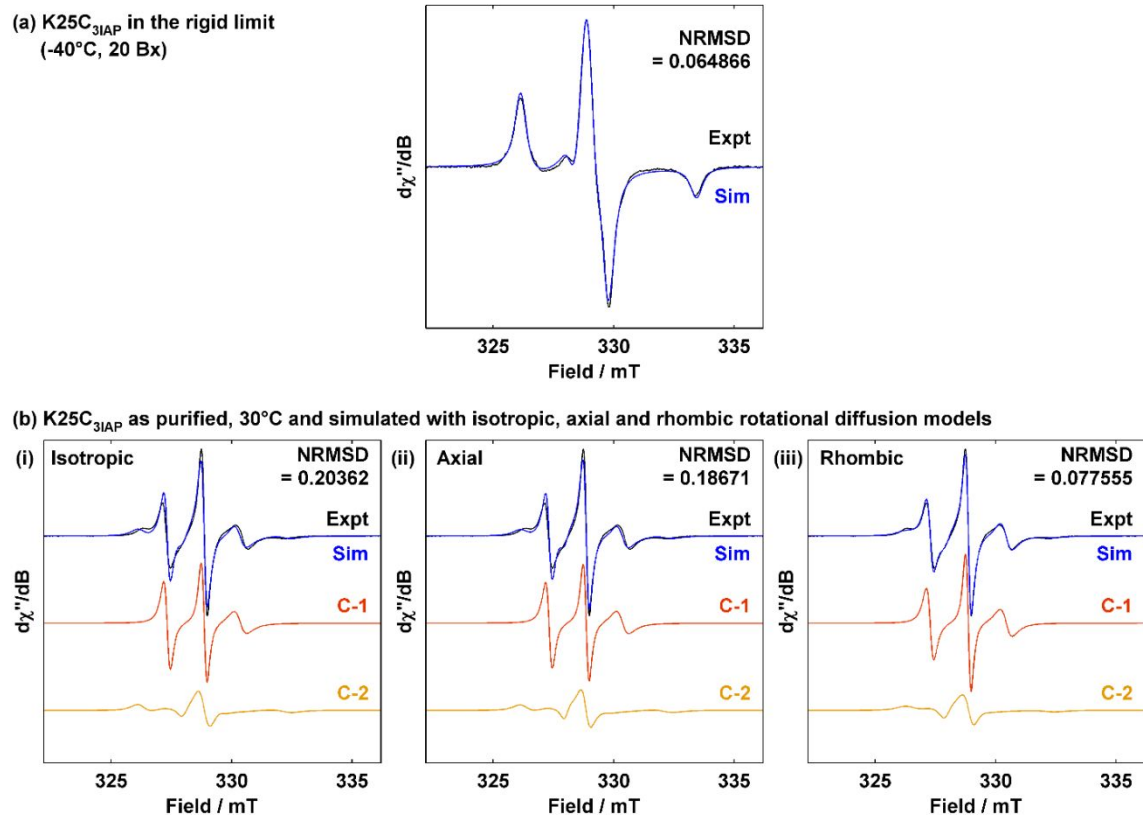


**Fig. S4.**  $K25C_{3IAP}$  displays at least two motional dynamics state.

(a) cw-EPR spectrum of  $K25C_{3IAP}$  at -40°C in 20% sucrose solution (black). Simulation of the near-rigid state spectrum is shown in blue. (b) Simulation (blue) of cw-EPR spectrum of  $K25C_{3IAP}$  (black) at ambient conditions (30°C) using (i) isotropic, (ii) axial and (iii) rhombic rotational diffusion models. The two motional components C-1 and C-2 are shown in red and yellow respectively. Refer to Table S1 for simulation parameters.

**Table S1.** Summary of best fit motional parameters for free K25C<sub>3IAP</sub>.

The  $g$  and  $A$  determined at  $-40^\circ\text{C}$ , 20% sucrose (= 20 Bx) are listed in the order of  $xx$ ,  $yy$  and  $zz$ . For  $\tau_c$ , axial values are listed in the order of  $\tau_{xy}$  and  $\tau_z$  whereas rhombic values are listed in the order of  $\tau_x$ ,  $\tau_y$ , and  $\tau_z$ . Square brackets indicate magnetic field bootstrap estimated 95% CI,  $n_{\text{bootstrap}} = 200$ .

K25C <sub>3IAP</sub>	Figure	$g$	$A$ / MHz	$\tau_c^{\text{expt}}$ / ns	Lw* / mT	Fraction/%	NRMSD
Near-rigid Limit (20Bx, 233K)	S4a			-	0.18, 0.29; [0.12, 0.25], [0.27, 0.30]	-	0.065
	S4bi <sup>†</sup>			1.40; [1.29, 1.51] 9.7; [8.2, 11.3]	-	50; [45, 56] 50; [44, 55]	0.204
$g, A$ fixed		2.0085, 2.0065, 2.00249;	16.3, 12.4, 102.24;	1.37, 10 <sup>5#</sup> ; [1.32, 1.44], [#]	-	49.6; [49.5, 49.8]	
	S4bii	[2.0084, 2.0087], [2.0063, 2.0065],	[15.1, 17.1], [11.6, 14.3],	8.803, 0.01 <sup>#</sup> ; [8.796, 8.804], [#]	-	50.4; [50.2, 50.5]	0.187
	S4biii	[2.00246, 2.00255]	[102.07, 102.49]	10 <sup>5#</sup> , 0.338, 1.323; [#], [0.314, 0.354], [1.274, 1.369]	-	52.2; [49.6, 54.5]	0.078
				3.1, 620, 5.5; [2.9, 3.3], [520, 780], [5.0, 6.4]	-	47.8; [45.5, 50.4]	

\* Phenomenological Gaussian and Lorentzian peak-to-peak linewidths in mT.

# Poorly constrained (reached lower or upper bound of parameter search space).

† The rotational correlation time of tetrameric KaiB was previously estimated to be 10.6 or 13.1 ns based on application of the Stokes-Einstein relation<sup>1</sup> and thus slower than that estimated by spectral simulations.

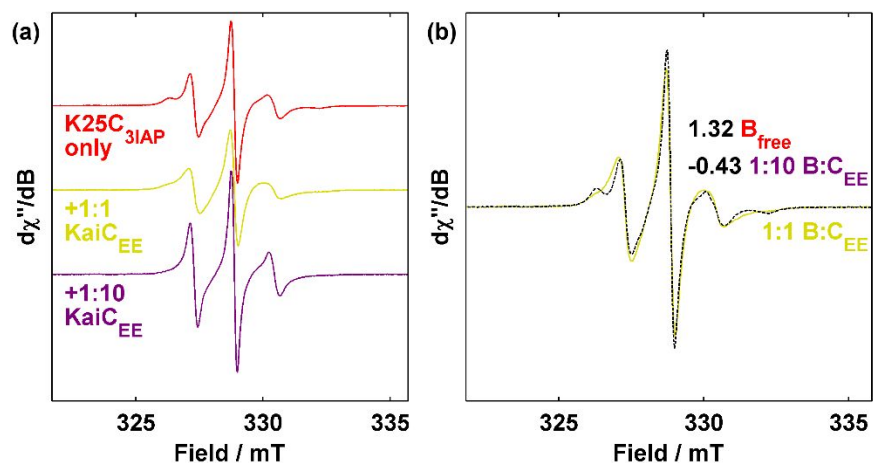


**Fig. S5.** Two components are insufficient to explain  $K25C_{3IAP}$ - $KaiC_{EE}$  reaction spectra. (a) Reproduction of Fig. 2c in the main text showing the spectrum of free  $K25C_{3IAP}$  (red) and its spectra when incubated with stoichiometric (dark yellow) and tenfold excess (purple)  $KaiC_{EE}$ . The reaction spectra are binned spectra for the time window  $t = 15 - 18$  hrs. (b) The experimental spectrum of 1:1  $K25C_{3IAP} + KaiC_{EE}$  (dark yellow) was attempted to be reproduced (black dotted line) by summing up spectra of free  $KaiB$  (red in (a)) and  $KaiB$  in tenfold excess  $KaiC_{EE}$  (purple in (a)). The smoothness of the low-field transition could not be reproduced in the weighted sum spectrum, suggesting that two spectral components are insufficient to explain the stoichiometric  $K25C_{3IAP}$ - $KaiC_{EE}$  spectrum.

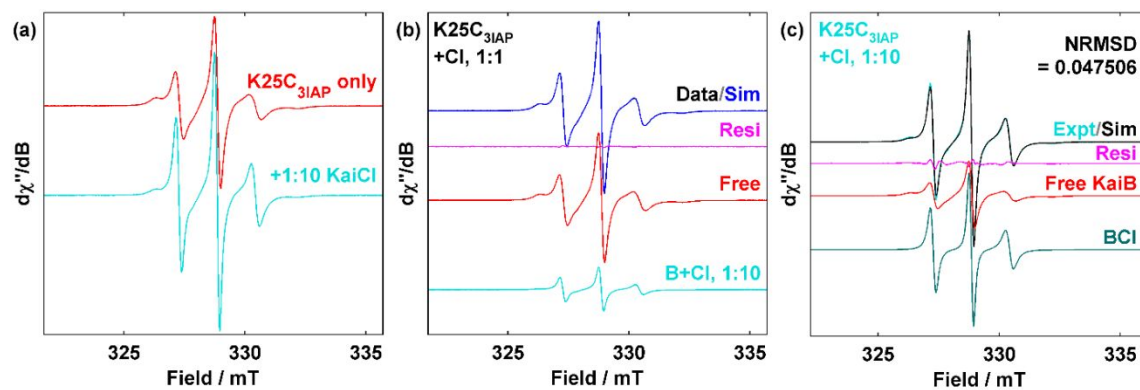


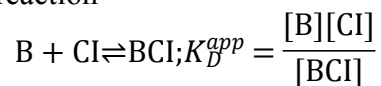
**Fig. S6.**  $\text{K25C}_{3\text{IAP}}$ -KaiCI reaction spectra at stoichiometric and 1:10 excess KaiC<sub>EE</sub> ratios. (a) Experimental spectra of  $\text{K25C}_{3\text{IAP}}$  alone (red) and in the presence of tenfold excess KaiCI (cyan). (b) Reproduction of the experimental spectrum of  $\text{K25C}_{3\text{IAP}}$  in the presence of stoichiometric KaiCI (black) with a sum of the spectra of free  $\text{K25C}_{3\text{IAP}}$  (red) and the 1:10 CI spectrum (cyan). (c) Semiphenomenological fitting (black) of the 1:10  $\text{K25C}_{3\text{IAP}}$ -KaiCI spectrum (cyan) using a sum of the spectrum of free  $\text{K25C}_{3\text{IAP}}$  (red) and a nitroxide species undergoing rhombic rotational diffusion (turquoise, see Table S2). The  $\text{K25C}_{3\text{IAP}}$ -CI reaction spectra shown are averaged between  $t = 15$ -18 hrs.

**Table S2.** Estimation of KaiB-CI direct binding dissociation constant.

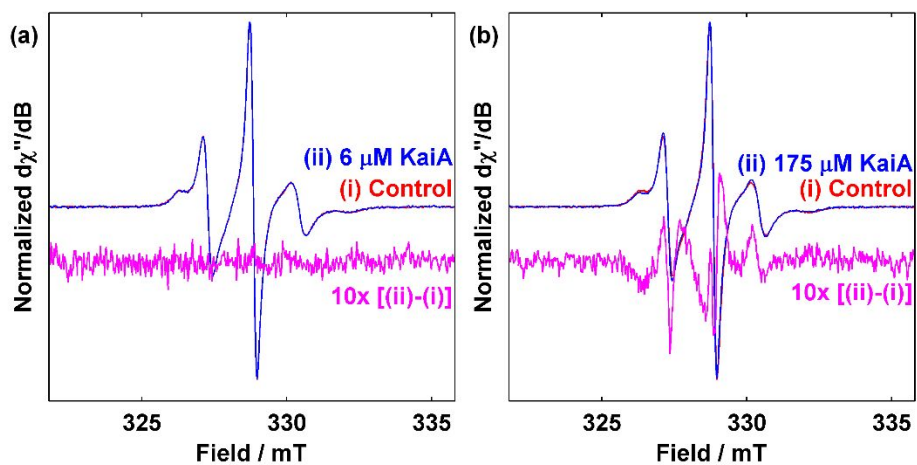
The  $g$  and  $A$  values were fixed from Table S1 whereas rhombic  $\tau_c$  and weight were floated. Values of  $\tau_c$  are listed in the order of  $\tau_x$ ,  $\tau_y$  and  $\tau_z$ . Square brackets indicate magnetic field bootstrap estimated 95% CI,  $n_{\text{bootstrap}} = 200$ .

	Figure	$\tau_c^{\text{expt}} / \text{ns}$	Weight / %	$K_D^{\text{app}} / \mu\text{M}^\#$	NRMSD
K25C <sub>31AP</sub> + 10x CI (BCI)	S6c	1.45, 0.32, 800;			
		[1.41, 1.50], [0.29, 0.37], [100, 1100]	46; [42, 52]	190; [150, 230]	0.0475

# Estimated by assuming the reaction



without accounting for KaiB tetramer-monomer equilibrium,  $[\text{B}]_0 = 17.5 \mu\text{M}$  and  $[\text{CI}]_0 = 175 \mu\text{M}$ .



**Fig. S7.** K25C<sub>31AP</sub> is insensitive to direct KaiA-KaiB interactions.

(a) and (b) Comparison of cw-EPR spectra acquired with 17.5  $\mu M$  K25C<sub>31AP</sub> (red) against K25C<sub>31AP</sub> equilibrated with 6  $\mu M$  (a) and 175  $\mu M$  (b) KaiA (blue). Spectra were normalized by their maximum intensity. The difference multiplied by 10 is shown in magenta below.



### 3.3 Estimation of cw-EPR spectra of $B_+$ and $B_-$

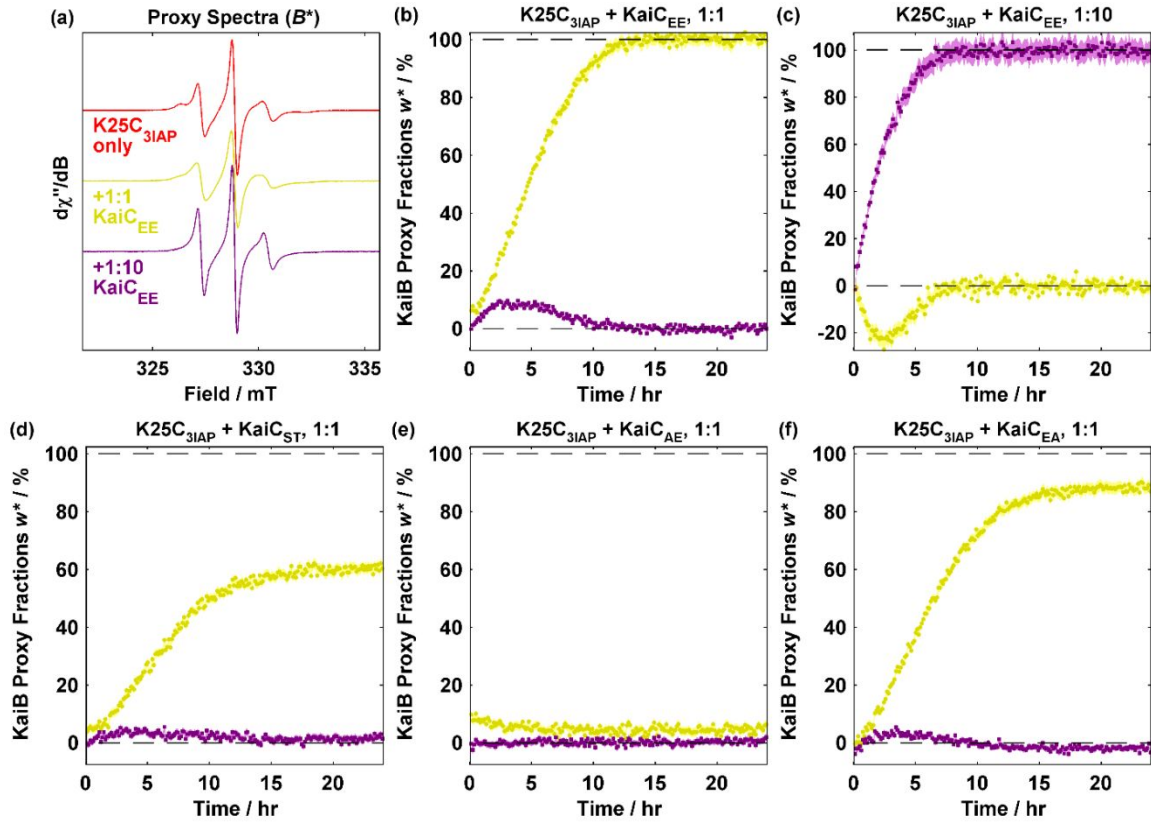


**Fig. S8.** Surrogate basis spectra ( $B^*$ ) and their respective proxy weights/concentrations ( $w^*$ ).

The use of experimental spectra as basis spectra ( $B^*$ ) for quantification leads to proxy weights ( $w^*$ ) that can be negative. (a) Reproduction of Fig. 2c in the main text showing the spectrum of free  $K25C_{3IAP}$  (red) and its spectra when incubated with stoichiometric (dark yellow) and tenfold excess (purple)  $KaiC_{EE}$ . The reaction spectra are binned spectra for the time window  $t = 15 - 18$  hrs. (b)-(e) Single-trial proxy kinetics of KaiB-KaiC phosphomimetic binding using the experimental spectra in (a) as basis spectra. The proxy weights sum up to 100% so the proxy weight of free  $K25C_{3IAP}$  was not shown.

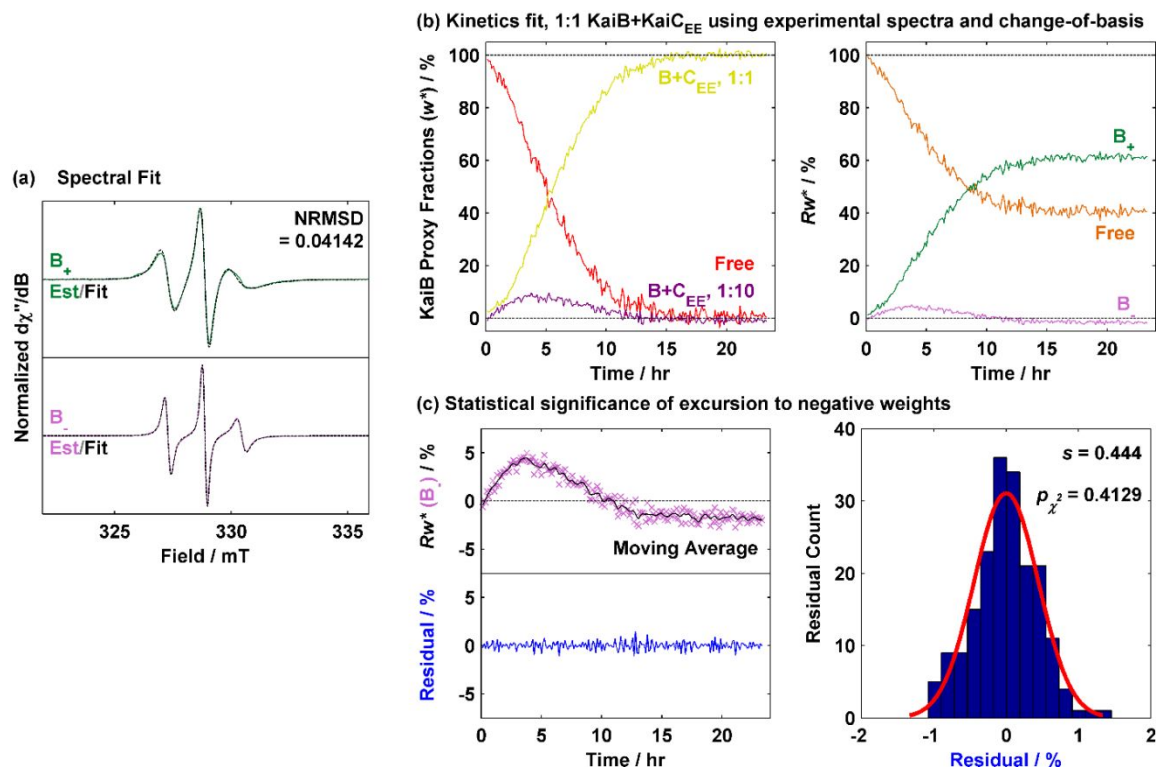


**Fig. S9.** Unconstrained single-component fitting of K25C<sub>3IAP</sub>-KaiC<sub>EE</sub> reaction spectra. Using the assumption that the spectra of B<sub>+</sub> and B<sub>-</sub> are approximated by spectra of nitroxides undergoing rhombic Brownian rotational diffusion as the only objective function via eq. (4.1) in the main text leads to negative kinetics. The spectra were fit to determine  $P$  and  $R$  using a *single* nitroxide component for each of B<sub>+</sub> and B<sub>-</sub>. In (a), the estimated spectra in green (B<sub>+</sub>) and light purple (B<sub>-</sub>) are overlaid with the spectral fit as black dashed lines. The normalized residual mean squared deviation (NRMSD) of the spectral fit is shown in the upper right. Refer to Table S3 for fitted parameters. In (b), the proxy kinetics ( $w^*$ , left) and resultant kinetics by performing the change-of-basis operation ( $w = R w^*$ , right) in the 1:1 KaiB+KaiC<sub>EE</sub> reaction are shown. Proxy kinetics: B<sub>free</sub> (red), 1:1 KaiB+KaiC<sub>EE</sub> (yellow) and 1:10 KaiB+KaiC<sub>EE</sub> (purple). Refer to Fig. S8a for their respective spectra. The statistical significance of the negative excursions in the kinetic traces of B<sub>-</sub> in (b) were examined in (c). Estimation of the uncertainty in the fitted kinetics by computation of the 7-point moving average (black in left panel) and the residual (blue in both panels) versus the change-of-basis fit (crosses) are shown. The normality of the residuals was tested by performing a  $\chi^2$  goodness-of-fit test and the  $p$ -values for deviation from Gaussian distribution as well as the standard deviations of the residuals are shown.

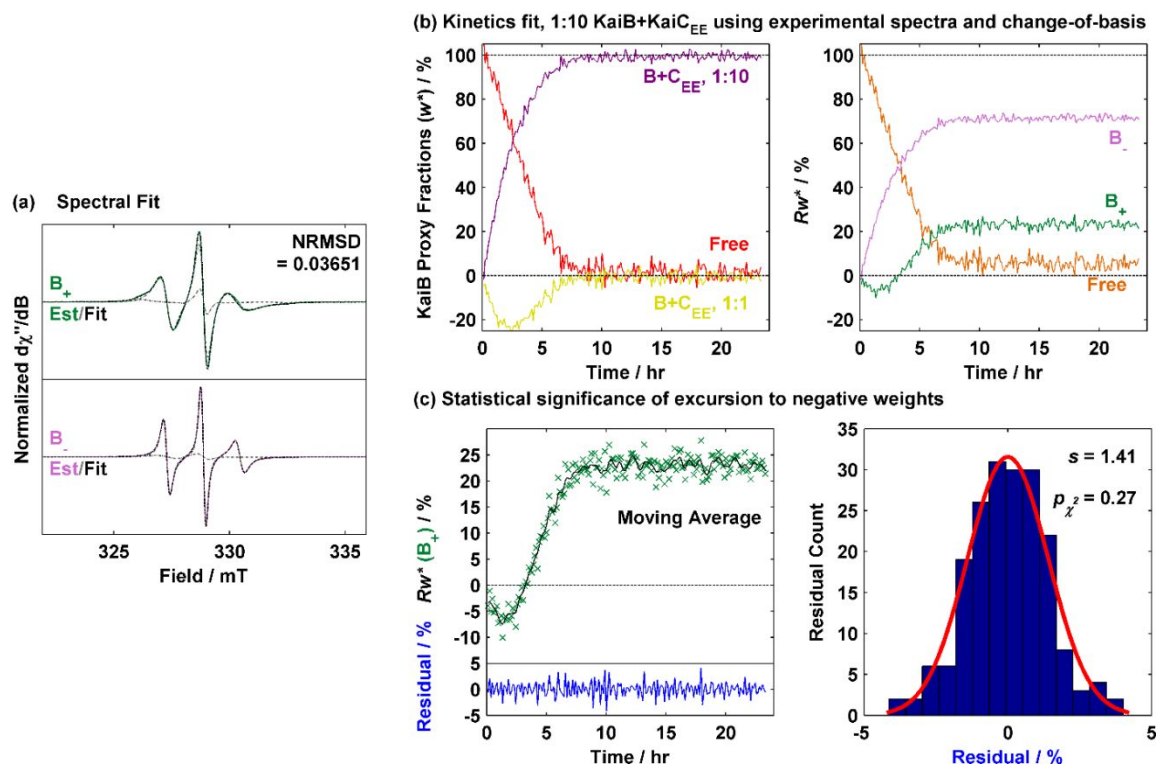


**Fig. S10.** Unconstrained two-component fitting of K25C<sub>3IAP</sub>-KaiC<sub>EE</sub> reaction spectra. Using the assumption that the spectra of B<sub>+</sub> and B<sub>-</sub> are approximated by spectra of nitroxides undergoing rhombic Brownian rotational diffusion as the only objective function via eq. (4.1) in the main text leads to negative kinetics. The spectra were fitted to determine  $P$  and  $R$  using *two* nitroxide components for each of B<sub>+</sub> and B<sub>-</sub>. In (a), the estimated spectra ( $B$ ) in green (B<sub>+</sub>) and light purple (B<sub>-</sub>) are overlaid with the spectral fit as black dashed lines. Individual nitroxide mobility components contributing to the spectra are shown as grey dash-dot lines. The normalized residual mean squared deviation (NRMSD) of the spectral fit is shown in the upper right. Refer to Table S3 for fitted parameters. In (b), the proxy kinetics ( $w^*$ , left) and resultant kinetics by performing the change-of-basis operation ( $w = Rw^*$ , right) in the 1:10 KaiB+KaiC<sub>EE</sub> reaction are shown. Proxy kinetics: B<sub>free</sub> (red), 1:1 KaiB+KaiC<sub>EE</sub> (yellow) and 1:10 KaiB+KaiC<sub>EE</sub> (purple). Refer to Fig. S8a for their respective spectra. The statistical significance of the negative excursions in the kinetic traces of B<sub>+</sub> in (b) were examined in (c). Estimation of the uncertainty in the fitted kinetics by computation of the 7-point moving average (black in left panel) and the residual (blue in both panels) versus the change-of-basis fit (crosses) are shown. The normality of the residuals was tested by performing a  $\chi^2$  goodness-of-fit test and the  $p$ -values for deviation from Gaussian distribution as well as the standard deviations of the residuals are shown.

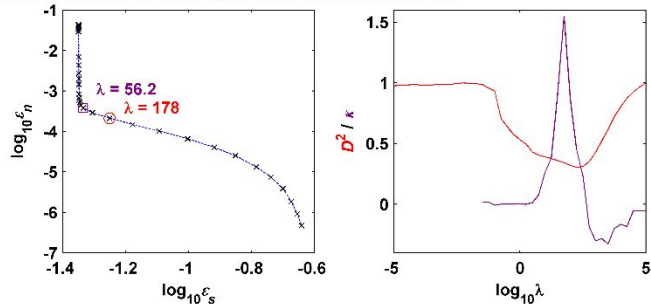
**Table S3.** Summary of single-objective best fit motional parameters for B<sub>+</sub> and B<sub>-</sub>. The  $g$  and  $A$  determined are fixed to those from Table S1. For  $\tau_c$ , rhombic values are listed in the order of  $\tau_x$ ,  $\tau_y$  and  $\tau_z$ .

K25C <sub>31AP</sub>	Component	Figure	$\tau_c^{\text{fit}} / \text{ns}$	Lw* / mT	Fraction/%	NRMSD
Single nitroxide	B <sub>+</sub>	S9a	1600, 0.9, 1.7	0.08, 0 <sup>#</sup>	-	0.0414
	B <sub>-</sub>		1.9, 0.4, 13	0.03, 0.004	-	
Two nitroxides	B <sub>+</sub>	S10a	8000, 0.9, 1.5	0.08, 0.002	82	0.0365
			4000, 3.3, 13	0.02, 0 <sup>#</sup>	18	
	B <sub>-</sub>		2.0, 0.4, 13	0.04, 0.004	79	
			1.6, 74, 4.0	0.07, 0.09	21	

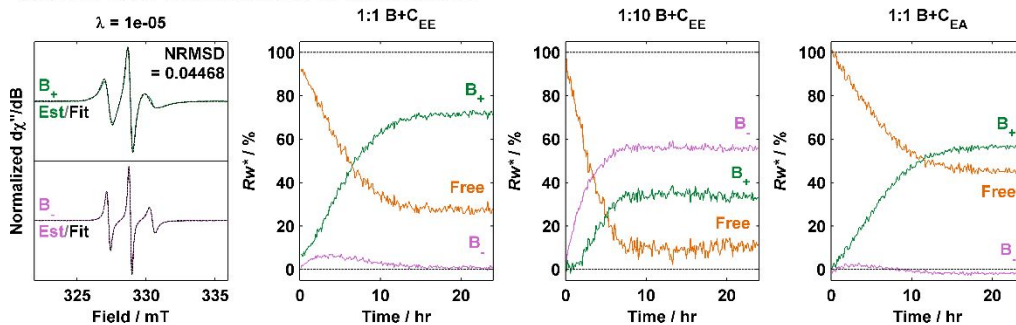
\* Phenomenological Gaussian and Lorentzian peak-to-peak linewidths in mT.

# Poorly constrained (reached lower or upper bound of parameter search space).

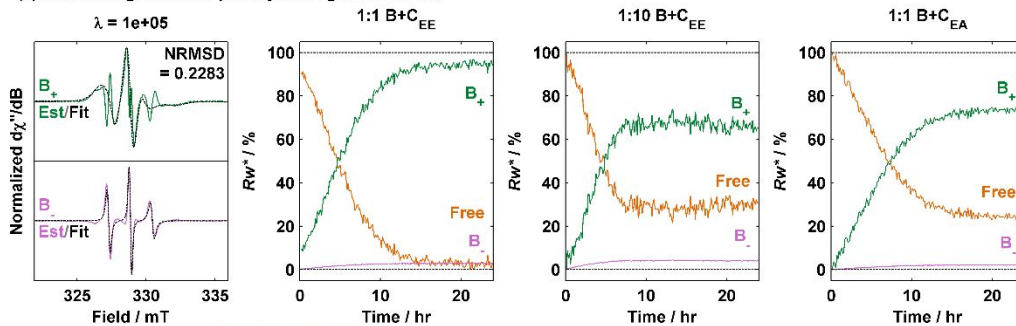
(a) Determination of  $\lambda$  in multiobjective optimization based quantitative cw-EPR



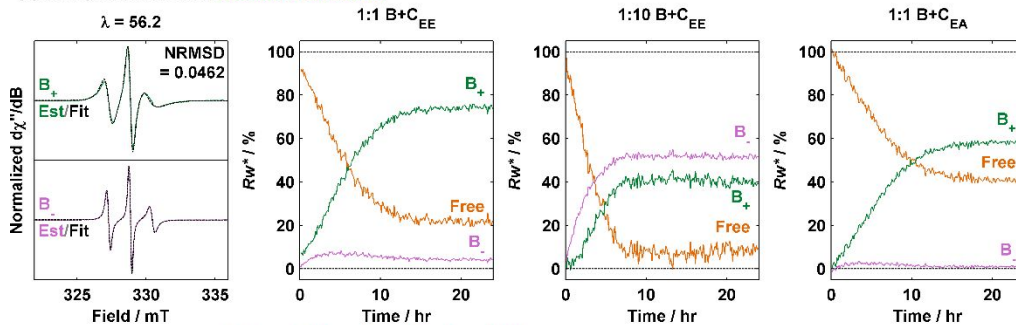
(b)  $\lambda$  is too small / insufficient penalty for negative kinetics



(c)  $\lambda$  is too large / excess penalty for negative kinetics



(d)  $\lambda$  is optimal based on maximum curvature  $\kappa$



(e)  $\lambda$  is optimal based on minimum distance from Utopia point  $D^2$

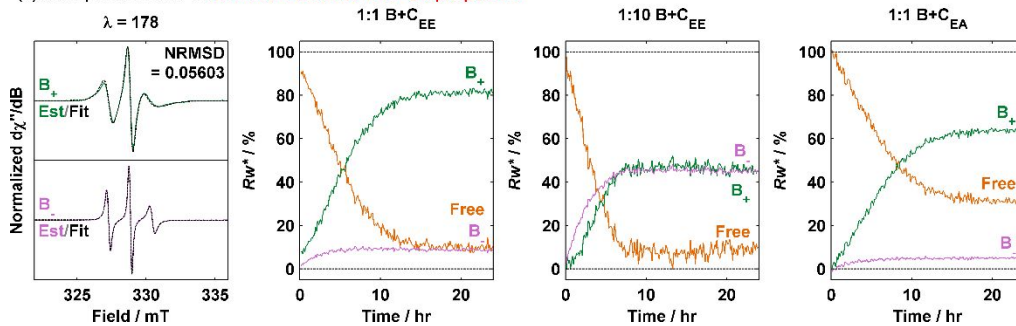


**Fig. S11.** Multiobjective optimization-based determination of change-of-basis matrix  $R$  using a single nitroxide mobility component per species:  $\lambda$  dependence.

(a) Determination of optimal  $\lambda$  to balance spectral error ( $\varepsilon_s$ ) and negative penalty ( $\varepsilon_n$ ). Left shows the plot of  $\varepsilon_n$  against  $\varepsilon_s$  on a log-log plot. Right shows the computed distance squared ( $D^2$ , red) and curvature ( $\kappa$ , purple). (b)–(e) plots of spectral fits (left) and their associated kinetics derived from change-of-basis (right) in the three experiments used for computing the negative kinetics penalty. (b): insufficient penalty ( $\lambda = 10^{-5}$ ). (c): excess penalty ( $\lambda = 10^5$ ). (d): optimal penalty based on maximum curvature on the  $L$ -curve ( $\lambda = 56.2$ ). (e): optimal penalty based on minimum Euclidean distance from the Utopia point ( $\lambda = 178$ ). The color scheme in (b)–(e) are free KaiB (dark orange),  $B_+$  (green) and  $B_-$  (light purple). Refer to Table S4 for fitting parameters.

**Table S4.** Summary of  $\lambda$ -dependent best fit motional parameters using a single nitroxide mobility component per species derived from one replicate dataset.

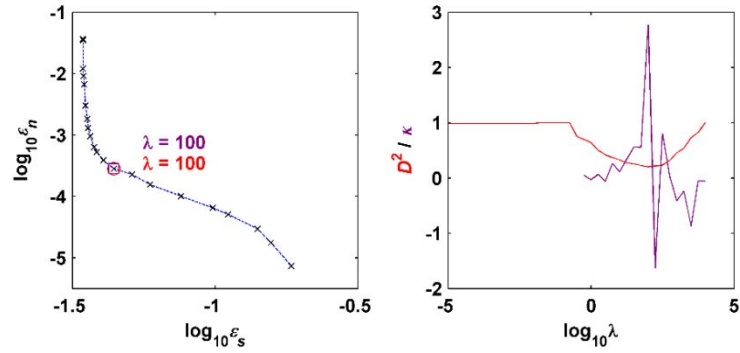
One replicate dataset consists of the K25C<sub>31AP</sub> experiments (i) 1:1 KaiB + KaiC<sub>EE</sub>, (ii) 1:10 KaiB + KaiC<sub>EE</sub> and (iii) 1:1 KaiB + KaiC<sub>EA</sub>. The  $g$  and  $A$  determined are fixed to those from Table S1. For  $\tau_c$ , rhombic values are listed in the order of  $\tau_x$ ,  $\tau_y$  and  $\tau_z$ .

$\lambda$	Component	Figure	$\tau_c^{\text{fit}} / \text{ns}$	Lw* / mT	NRMSD
$10^{-5}$	$B_+$	S11b	2200, 0.9, 1.6	0.03, 0 <sup>#</sup>	0.0447
	$B_-$		1.8, 0.4, 33	0.02, 0.009	
56.2 ( $\kappa_{\text{max}}$ )	$B_+$	S11d	1800, 1.0, 1.6	0.01, 0 <sup>#</sup>	0.0462
	$B_-$		1.7, 0.4, 650	0.04, 0.005	
178 ( $D^2_{\text{min}}$ )	$B_+$	S11e	3600, 1.0, 1.7	0.005, 0 <sup>#</sup>	0.0563
	$B_-$		1.6, 0.4, 1600	0.06, 0.001	
$10^5$	$B_+$	S11c	7.1, 2.7, 2.7	0.17, 0 <sup>#</sup>	0.228
	$B_-$		1.2, 0.1, 2300	0.08, 0 <sup>#</sup>	

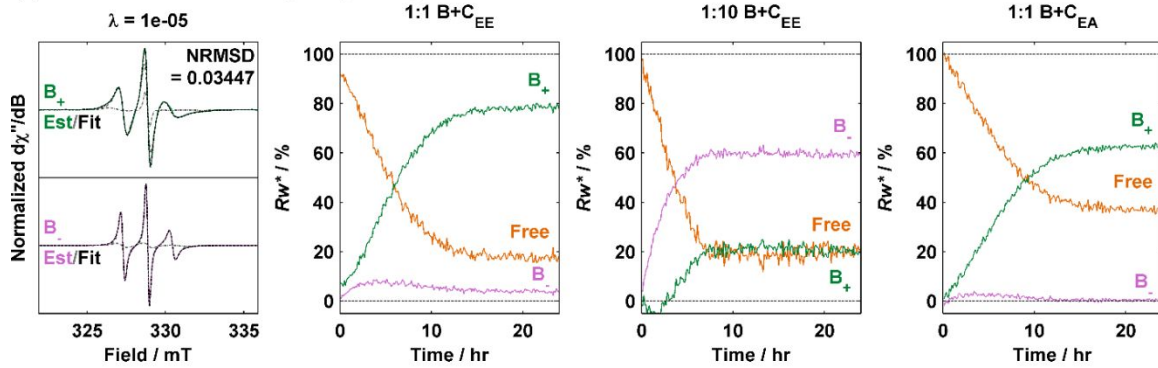
\* Phenomenological Gaussian and Lorentzian peak-to-peak linewidths in mT.

# Poorly constrained (reached lower or upper bound of parameter search space).

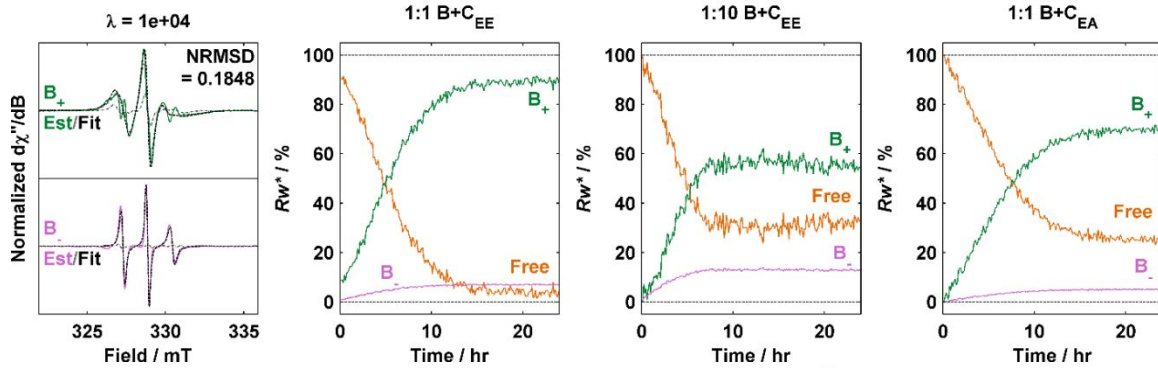
(a) Determination of  $\lambda$  in multiobjective optimization based quantitative cw-EPR



(b)  $\lambda$  is too small / insufficient penalty for negative kinetics



(c)  $\lambda$  is too large / excess penalty for negative kinetics



(d)  $\lambda$  is optimal based on maximum curvature  $\kappa$  and minimum distance from Utopia point  $D^2$

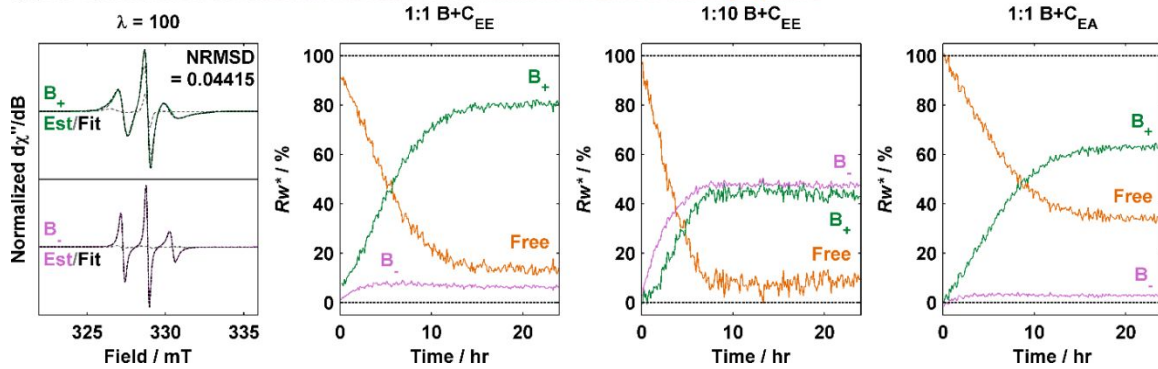


**Fig. S12.** Multiobjective optimization-based determination of change-of-basis matrix  $R$  using two nitroxide mobility components per species:  $\lambda$  dependence.

(a) Determination of optimal  $\lambda$  to balance spectral error ( $\varepsilon_s$ ) and negative penalty ( $\varepsilon_n$ ). Left shows the plot of  $\varepsilon_n$  against  $\varepsilon_s$  on a log-log plot. Right shows the computed distance squared ( $D^2$ , red) and curvature ( $\kappa$ , purple). (b)–(d) plots of spectral fits (left) and their associated kinetics derived from change-of-basis (right) in the three experiments used for computing the negative kinetics penalty. (b): insufficient penalty ( $\lambda = 10^{-5}$ ). (c): excess penalty ( $\lambda = 10^5$ ). (d): optimal penalty based on maximum curvature and minimum Euclidean distance from the Utopia point on the  $L$ -curve ( $\lambda = 100$ ). The color scheme in (b)–(d) are free KaiB (dark orange),  $B_+$  (green) and  $B_-$  (light purple). Refer to Table S5 for fitting parameters.

**Table S5.** Summary of  $\lambda$ -dependent best fit motional parameters using two nitroxide mobility component per species derived from one replicate dataset.

One replicate dataset consists of the K25C<sub>31AP</sub> experiments (i) 1:1 KaiB + KaiC<sub>EE</sub>, (ii) 1:10 KaiB + KaiC<sub>EE</sub> and (iii) 1:1 KaiB + KaiC<sub>EA</sub>. The  $g$  and  $A$  determined are fixed to those from Table S1. For  $\tau_c$ , rhombic values are listed in the order of  $\tau_x$ ,  $\tau_y$  and  $\tau_z$ . Each row describes one mobility component contributing to the overall spectrum of the respective species.

$\lambda$	Component	Figure	$\tau_c^{\text{fit}}$ / ns	Lw* / mT	Weight Fraction / %	NRMSD
$10^{-5}$	$B_+$	S12b	300, 0.8, 1.4	0.20 <sup>#</sup> , 0 <sup>#</sup>	83	0.0345
			2900, 2.6, 560	0.16, 0 <sup>#</sup>	17	
	$B_-$		1.7, 0.4, 1100	0.06, 0 <sup>#</sup>	76	
			0.7, 210, 21	0.20 <sup>#</sup> , 0.18	24	
100 ( $D^2_{\text{min}}$ ; $\kappa_{\text{max}}$ )	$B_+$	S12d	58, 0.9, 1.4	0.18, 0 <sup>#</sup>	83	0.0442
			800, 2.1, 1100	0.20 <sup>#</sup> , 0 <sup>#</sup>	17	
	$B_-$		1.6, 0.4, 10 <sup>4</sup>	0.06, 0 <sup>#</sup>	92	
			0.2, 2100, 2800	0.03, 0.17	8	
$10^4$	$B_+$	S12c	79, 1.5, 0.9	0.11, 0 <sup>#</sup>	84	0.185
			9000, 0.6, 7000	0.20 <sup>#</sup> , 0.11	16	
	$B_-$		1.2, 0.2, 210	0.08, 0 <sup>#</sup>	95	
			0.1, 7000, 760	0.13, 0.01	5	

\* Phenomenological Gaussian and Lorentzian peak-to-peak linewidths in mT.

# Poorly constrained (reached lower or upper bound of parameter search space).



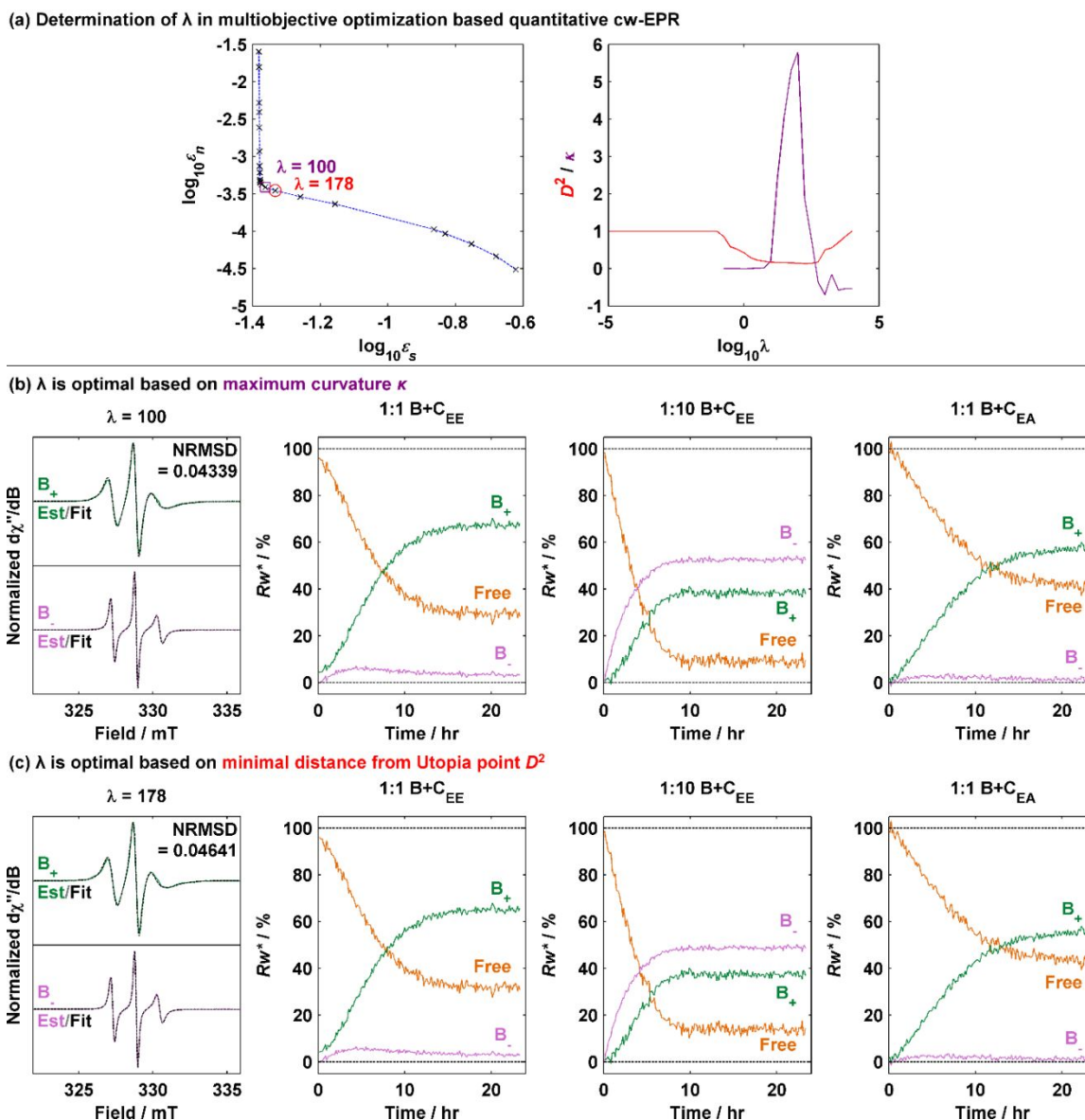


**Fig. S13.** Multiobjective optimization-based determination of change-of-basis matrix  $R$  using one nitroxide mobility component per species in second technical replicate.

(a) Determination of optimal  $\lambda$  to balance spectral error ( $\varepsilon_s$ ) and negative penalty ( $\varepsilon_n$ ). Left shows the plot of  $\varepsilon_n$  against  $\varepsilon_s$  on a log-log plot. Right shows the computed distance squared ( $D^2$ , red circle) and curvature ( $\kappa$ , purple square). (b)–(c) plots of spectral fits (left) and their associated kinetics derived from change-of-basis (right) in the three experiments used for computing the negative kinetics penalty. (b): optimal penalty based on maximum curvature ( $\lambda = 100$ ). (c): optimal penalty based on minimum Euclidean distance from the Utopia point on the  $L$ -curve ( $\lambda = 178$ ). The color scheme in (b)–(c) are free KaiB (dark orange),  $B_+$  (green) and  $B_-$  (light purple). Refer to Table S6 for fitting parameters.

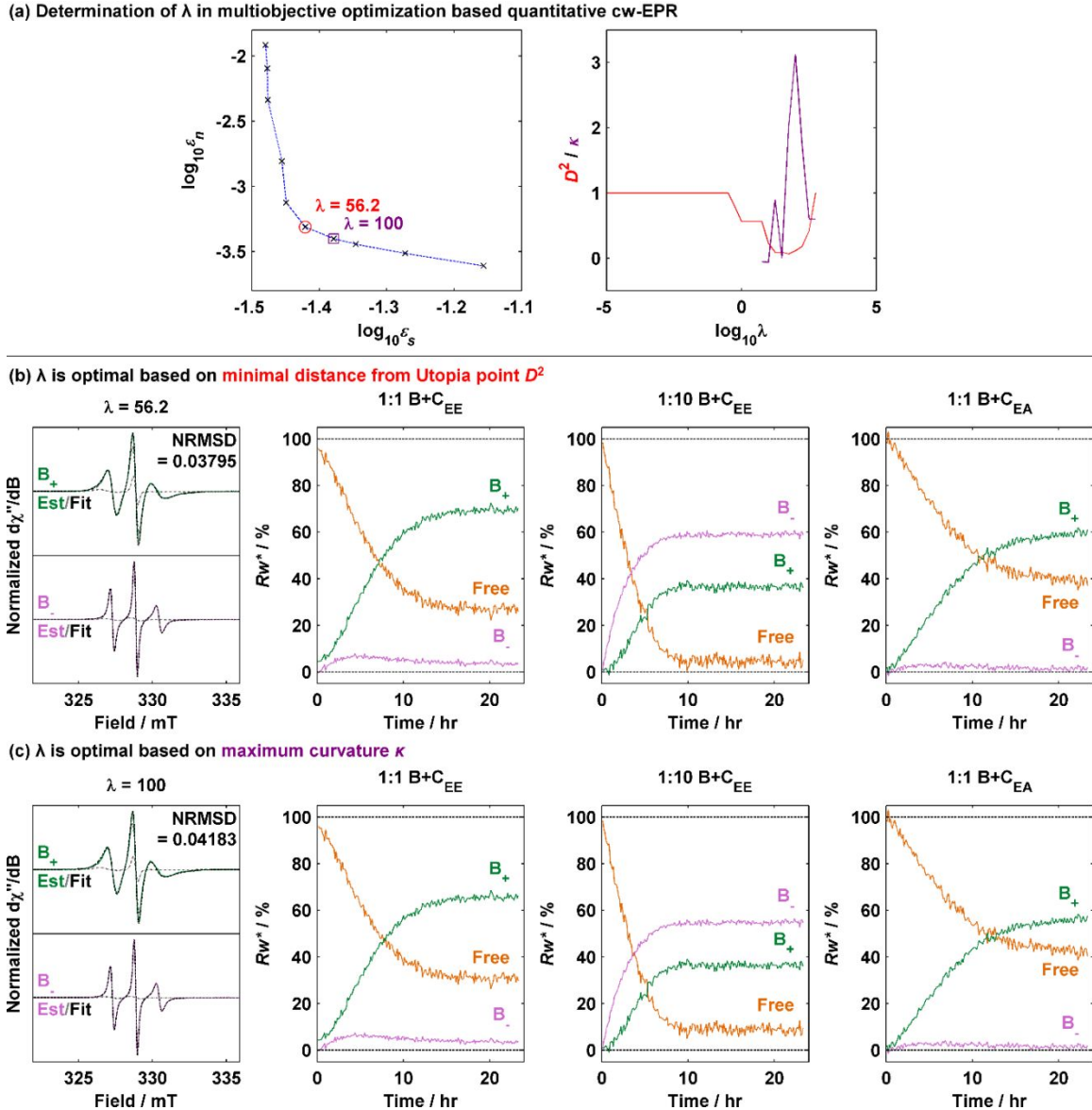
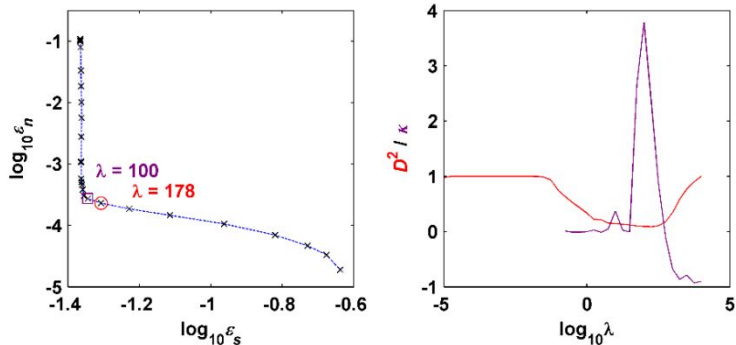


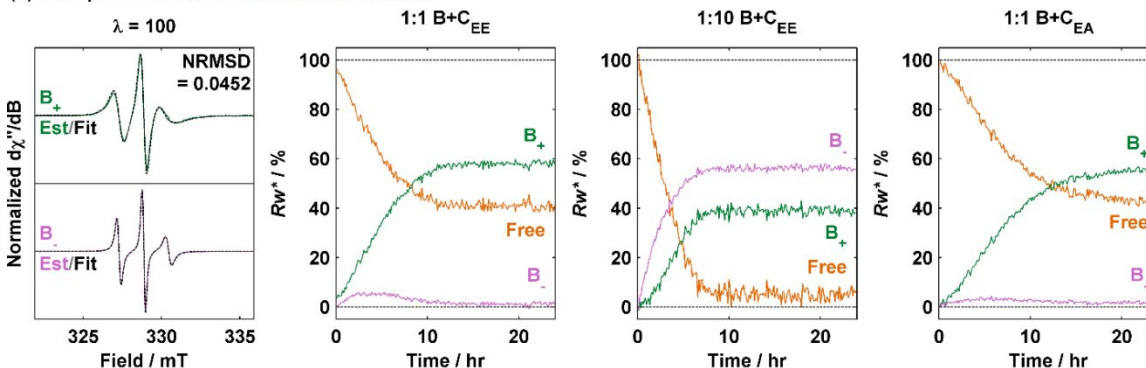
**Fig. S14.** Multiobjective optimization-based determination of change-of-basis matrix  $R$  using two nitroxide mobility components per species in second technical replicate.

(a) Determination of optimal  $\lambda$  to balance spectral error ( $\epsilon_s$ ) and negative penalty ( $\epsilon_n$ ). Left shows the plot of  $\epsilon_n$  against  $\epsilon_s$  on a log-log plot. Right shows the computed distance squared ( $D^2$ , red circle) and curvature ( $\kappa$ , purple square). (b)–(c) plots of spectral fits (left) and their associated kinetics derived from change-of-basis (right) in the three experiments used for computing the negative kinetics penalty. The nitroxide mobility components are overlaid in gray. (b): optimal penalty based on minimum Euclidean distance from the Utopia point on the  $L$ -curve ( $\lambda = 56.2$ ). (c): optimal penalty based on maximum curvature ( $\lambda = 100$ ). The color scheme in (b)–(c) are free KaiB (dark orange),  $B_+$  (green) and  $B_-$  (light purple). Refer to Table S6 for fitting parameters.

(a) Determination of  $\lambda$  in multiobjective optimization based quantitative cw-EPR



(b)  $\lambda$  is optimal based on maximum curvature  $\kappa$



(c)  $\lambda$  is optimal based on minimal distance from Utopia point  $D^2$

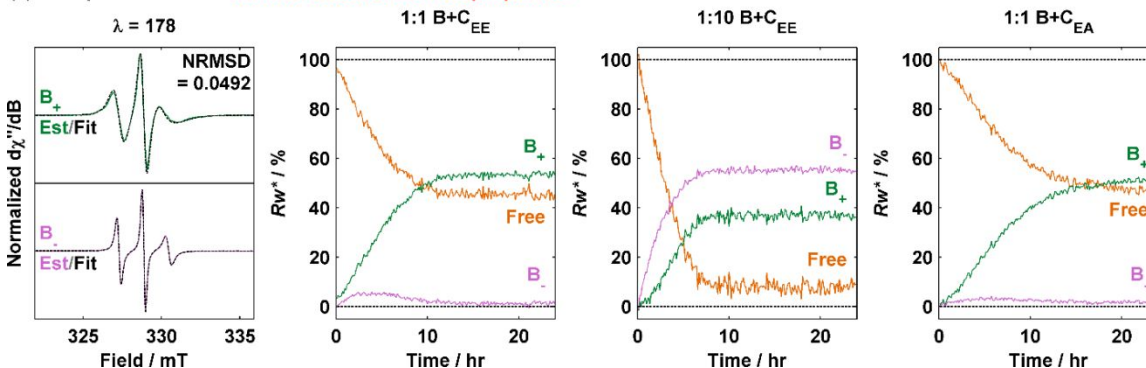
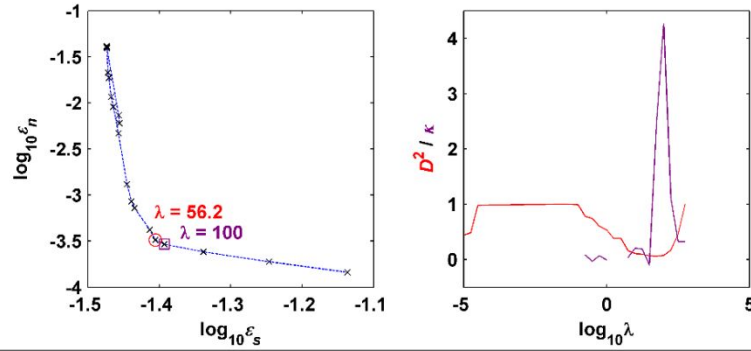


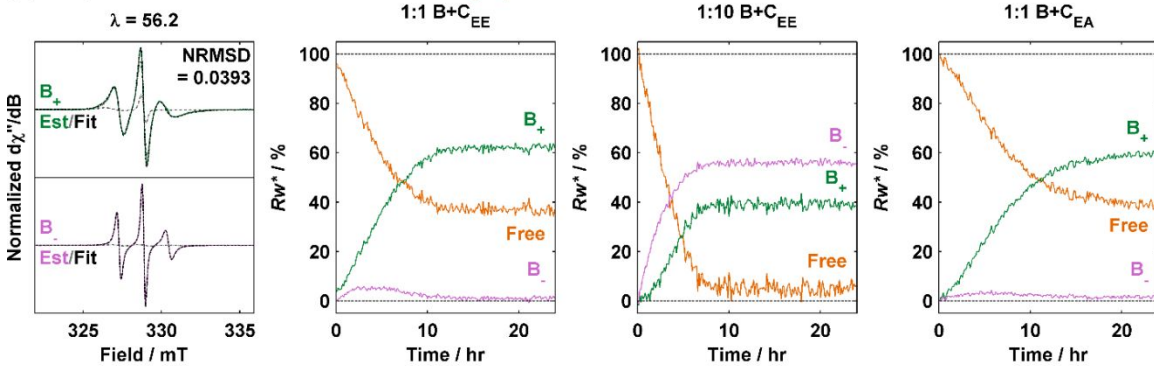
**Fig. S15.** Multiobjective optimization-based determination of change-of-basis matrix  $R$  using one nitroxide mobility component per species in third technical replicate.

(a) Determination of optimal  $\lambda$  to balance spectral error ( $\epsilon_s$ ) and negative penalty ( $\epsilon_n$ ). Left shows the plot of  $\epsilon_n$  against  $\epsilon_s$  on a log-log plot. Right shows the computed distance squared ( $D^2$ , red circle) and curvature ( $\kappa$ , purple square). (b)–(c) plots of spectral fits (left) and their associated kinetics derived from change-of-basis (right) in the three experiments used for computing the negative kinetics penalty. (b): optimal penalty based on maximum curvature ( $\lambda = 100$ ). (c): optimal penalty based on minimum Euclidean distance from the Utopia point on the  $L$ -curve ( $\lambda = 178$ ). The color scheme in (b)–(c) are free KaiB (dark orange),  $B_+$  (green) and  $B_-$  (light purple). Refer to Table S6 for fitting parameters.

(a) Determination of  $\lambda$  in multiobjective optimization based quantitative cw-EPR



(b)  $\lambda$  is optimal based on minimal distance from Utopia point  $D^2$



(c)  $\lambda$  is optimal based on maximum curvature  $\kappa$

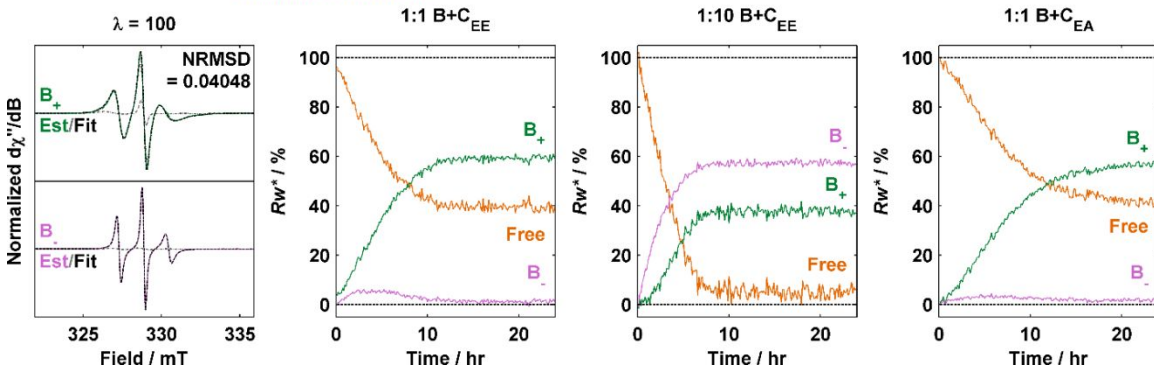


**Fig. S16.** Multiobjective optimization-based determination of change-of-basis matrix  $R$  using two nitroxide mobility components per species in third technical replicate.

(a) Determination of optimal  $\lambda$  to balance spectral error ( $\epsilon_s$ ) and negative penalty ( $\epsilon_n$ ). Left shows the plot of  $\epsilon_n$  against  $\epsilon_s$  on a log-log plot. Right shows the computed distance squared ( $D^2$ , red circle) and curvature ( $\kappa$ , purple square). The curvature at around  $\lambda = 1$  was manually pruned during analysis to preclude selection of local curvature maximum in the Pareto front. (b)–(c) plots of spectral fits (left) and their associated kinetics derived from change-of-basis (right) in the three experiments used for computing the negative kinetics penalty. The nitroxide mobility components are overlaid in gray. (b): optimal penalty based on minimum Euclidean distance from the Utopia point on the  $L$ -curve ( $\lambda = 56.2$ ). (c): optimal penalty based on maximum curvature ( $\lambda = 100$ ). The color scheme in (b)–(c) are free KaiB (dark orange),  $B_+$  (green) and  $B_-$  (light purple). Refer to Table S6 for fitting parameters.

**Table S6.** Summary of multiobjective optimization based best fit motional parameters of B<sub>+</sub> and B<sub>-</sub> in replicate datasets.

One replicate dataset consists of the K25C<sub>3IAP</sub> experiments (i) 1:1 KaiB + KaiC<sub>EE</sub>, (ii) 1:10 KaiB + KaiC<sub>EE</sub> and (iii) 1:1 KaiB + KaiC<sub>EA</sub>. The  $g$  and  $A$  determined are fixed to those from Table S1. For  $\tau_c$ , rhombic values are listed in the order of  $\tau_x$ ,  $\tau_y$  and  $\tau_z$ . Each row describes one mobility component contributing to the overall spectrum of the respective species.

Dataset; (mobility components)	$\lambda$	Species	Figure	$\tau_c^{\text{fit}} / \text{ns}$	Lw* / mT	Weight Fraction / %	NRMSD	
2 (1-component)	100 ( $\kappa_{\text{max}}$ )	B <sub>+</sub>	S13b	300, 1.0, 1.7	0.08, 0 <sup>#</sup>	-	0.0434	
		B <sub>-</sub>		1.8, 0.4, 29	0.03, 0.004	-		
	178 ( $D_{\text{min}}$ )	B <sub>+</sub>	S13c	300, 1.0, 1.7	0.09, 0 <sup>#</sup>	-		
		B <sub>-</sub>		1.7, 0.4, 35	0.03, 0.005	-		
2 (2-component)	56.2 ( $D_{\text{min}}$ )	B <sub>+</sub>	S14b	970, 0.9, 1.5 900, 2.5, 4000	0.2 <sup>#</sup> , 0 <sup>#</sup> 0.19, 0 <sup>#</sup>	84 16	0.0380	
		B <sub>-</sub>		1.8, 0.4, 26 1.5, 2100, 32	0.05, 0 <sup>#</sup> 0.2 <sup>#</sup> , 0.14	81 19		
	100 ( $\kappa_{\text{max}}$ )	B <sub>+</sub>	S14c	840, 0.9, 1.5 9000, 2.3, 1800	0.2 <sup>#</sup> , 0 <sup>#</sup> 0.19, 0 <sup>#</sup>	86 14		0.0418
		B <sub>-</sub>		1.7, 0.4, 41 1.2, 2200, 39	0.05, 0 <sup>#</sup> 0.2 <sup>#</sup> , 0.14	84 16		
3 (1-component)	100 ( $\kappa_{\text{max}}$ )	B <sub>+</sub>	S15b	1100, 1.0, 1.7	0.1, 0 <sup>#</sup>	-	0.0452	
		B <sub>-</sub>		1.8, 0.4, 44	0.04, 0 <sup>#</sup>	-		
	178 ( $D_{\text{min}}$ )	B <sub>+</sub>	S15c	570, 1.0, 1.8	0.14, 0 <sup>#</sup>	-		
		B <sub>-</sub>		1.8, 0.4, 77	0.04, 0 <sup>#</sup>	-		
3 (2-component)	56.2 ( $D_{\text{min}}$ )	B <sub>+</sub>	S16b	110, 0.9, 1.5 3100, 2.6, 720	0.2 <sup>#</sup> , 0 <sup>#</sup> 0.2 <sup>#</sup> , 0 <sup>#</sup>	85 15	0.0393	
		B <sub>-</sub>		1.8, 0.4, 41 0.9, 9000, 10 <sup>5#</sup>	0.04, 0 <sup>#</sup> 0.2 <sup>#</sup> , 0.2 <sup>#</sup>	90 10		
	100 ( $\kappa_{\text{max}}$ )	B <sub>+</sub>	S16c	190, 0.9, 1.6 5000, 2.7, 2800	0.2 <sup>#</sup> , 0 <sup>#</sup> 0.2 <sup>#</sup> , 0.003	87 13		0.0405
		B <sub>-</sub>		1.8, 0.4, 59 0.9, 10 <sup>5#</sup> , 10 <sup>5#</sup>	0.04, 0 <sup>#</sup> 0.2 <sup>#</sup> , 0.2 <sup>#</sup>	90 10		

\* Phenomenological Gaussian and Lorentzian peak-to-peak linewidths in mT.

# Poorly constrained (reached lower or upper bound of parameter search space).

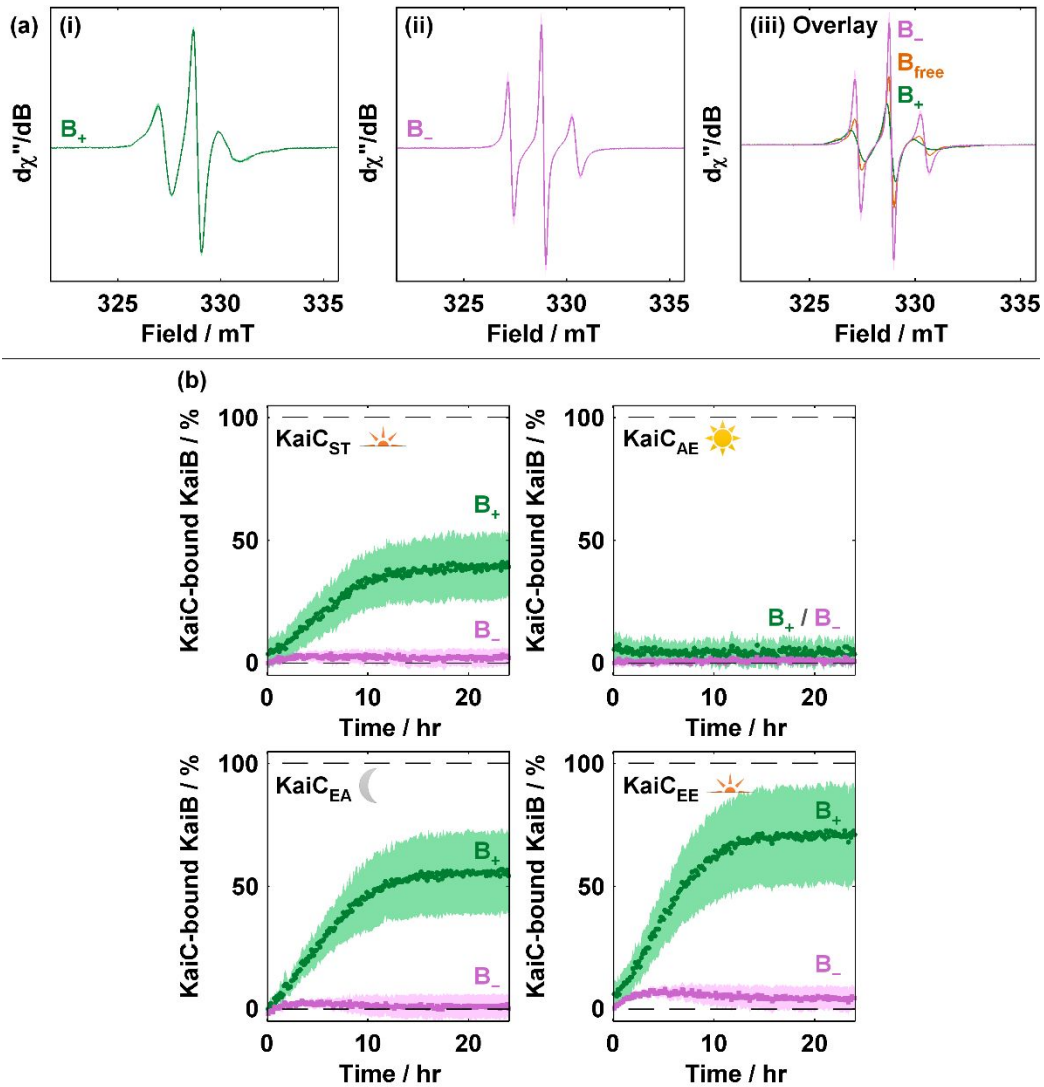


**Fig. S17.** Summary of spectral fit of  $B_+$  and  $B_-$  and associated kinetics.

(a) Estimated spectra of  $B_+$  (i, green),  $B_-$  (ii, light purple), and overlay with free KaiB (brown). Shaded areas show 95% CI (visible at higher magnification). Note that the spectrum of free KaiB also possesses uncertainty as the spectrum as shown is an average from technical triplicates. (b) Estimated kinetics of  $B_+$  and  $B_-$  using spectra obtained from the negative kinetics-penalized spectral fits. Shaded areas show single-trial 95% CI based on spectral modeling ( $\lambda$  dependence) and imperfect signal-to-noise.

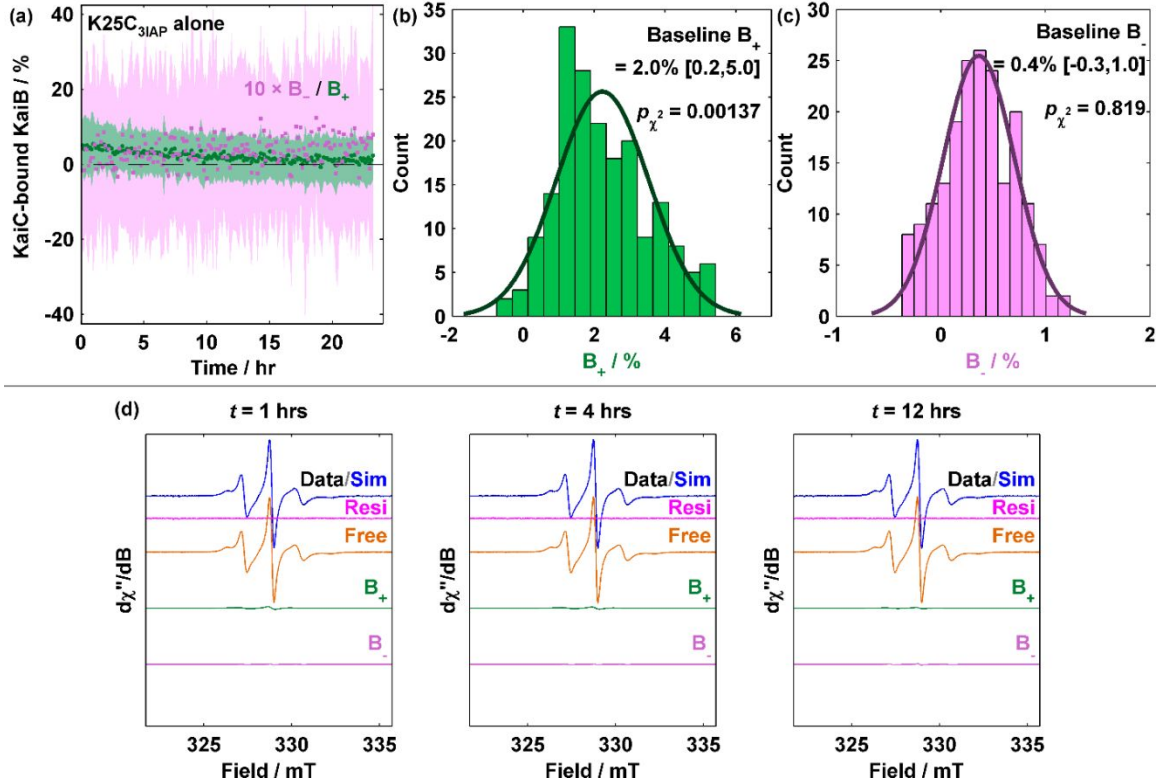


**Fig. S18.** Determination of fictitious KaiC-bound KaiB populations.

The baseline  $B_+$  and  $B_-$  populations were determined by quantifying them in reaction samples containing only  $K25C_{3IAP}$  in the absence of KaiC (i.e., false positives). (a) KaiB-KaiC binding kinetics in control experiment without KaiC. Shaded areas show 95% CI derived from a combination of modeling uncertainty and inter-replicate variability ( $n = 3$ ).  $B_+$ : green circles.  $B_-$ : light purple squares. (b) and (c) Histograms of  $B_+$  and  $B_-$  concentrations in (a). Legend shows median and 95% CI (2.5<sup>th</sup> and 97.5<sup>th</sup> percentiles) as well as  $\chi^2$  goodness-of-fit test against Gaussian distributions. (d) Representative spectral fit (blue) of the experimental spectra (black). The residual is shown in bright magenta. The components are free KaiB (orange),  $B_+$  (green) and  $B_-$  (light purple).

### 3.4 $B_-$ is an intermediate between $B_+$ and free KaiB

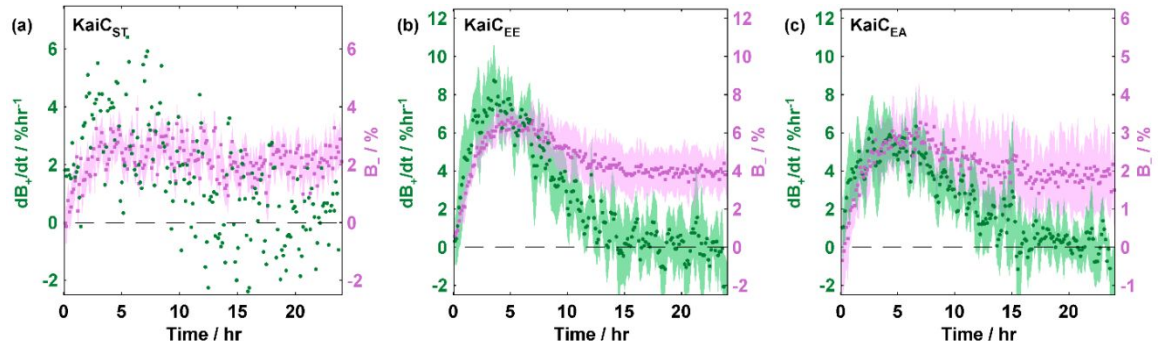


**Fig. S19.** Overlay of  $dB_+/dt$  and  $B_-$  in  $K25C_{3IAP}$ - $KaiC_{ST/EE/EA}$  reactions.

(a)  $KaiC_{ST}$ ; (b)  $KaiC_{EE}$ ; (c)  $KaiC_{EA}$ . Green circles:  $dB_+/dt$  ( $\% hr^{-1}$ ); Light purple squares:  $B_-$  ( $\%$ ). For (a), shaded area for  $B_-$  indicates single-trial 95% CI due to imperfect signal-to-noise ( $n = 1$ ). The uncertainty in rate of  $B_+$  formation could not be directly computed and was not shown. For (b) and (c), shaded areas represent inter-replicate 95% CI ( $n = 6$ ).



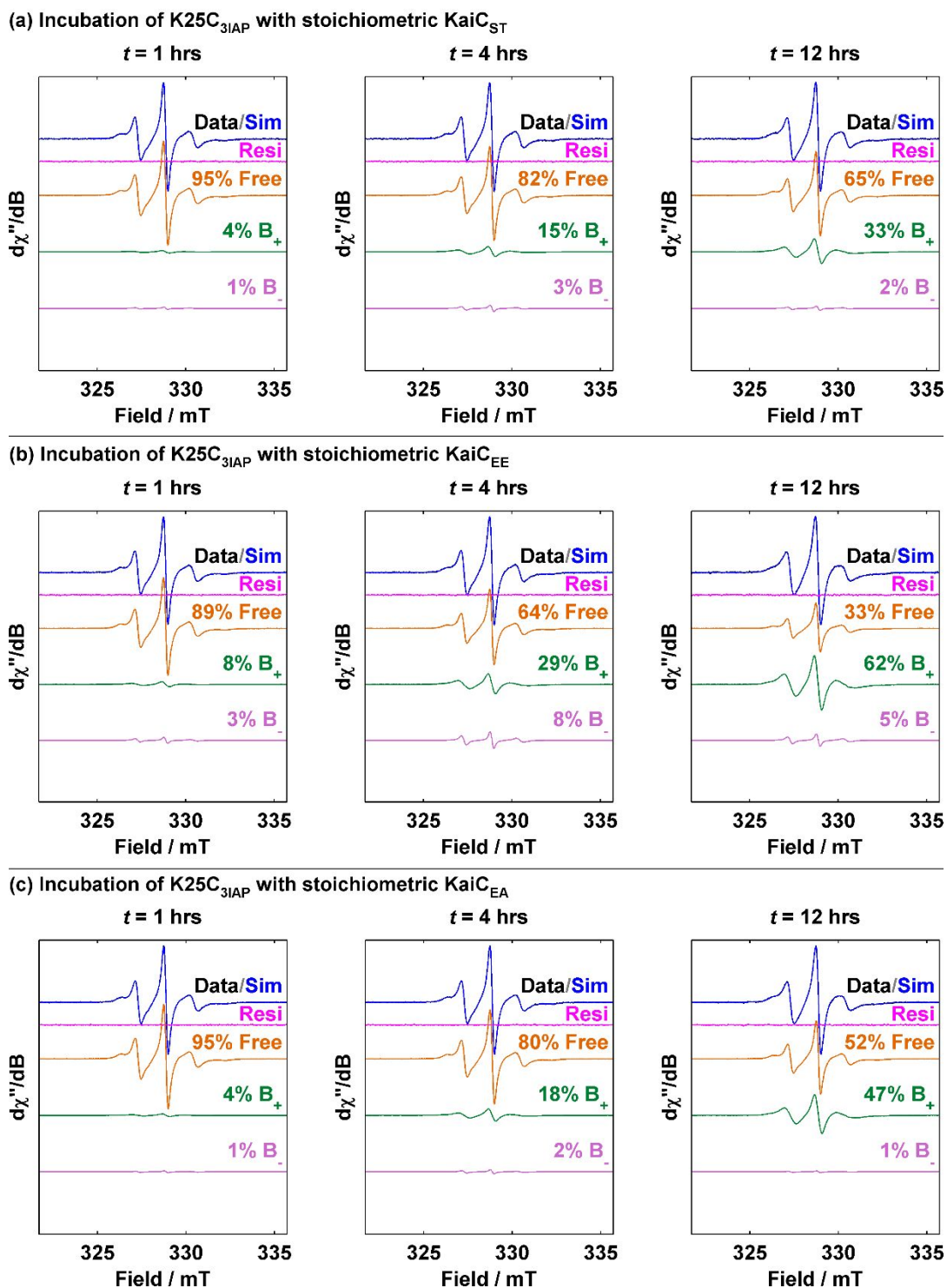


**Fig. S20.** Spectral simulations of  $K25C_{3IAP}$ - $KaiC_{ST/EE/EA}$  reactions.

(a), (b) and (c) correspond to  $KaiC_{ST}$ ,  $KaiC_{EE}$  and  $KaiC_{EA}$ , respectively. Experimental spectra are shown in black and overlaid with simulations in blue. The residual is shown in

bright magenta. The components are free KaiB (orange), B<sub>+</sub> (green) and B<sub>-</sub> (light purple). Representative spectral model (out of 12 spectral models) shown in the fits.

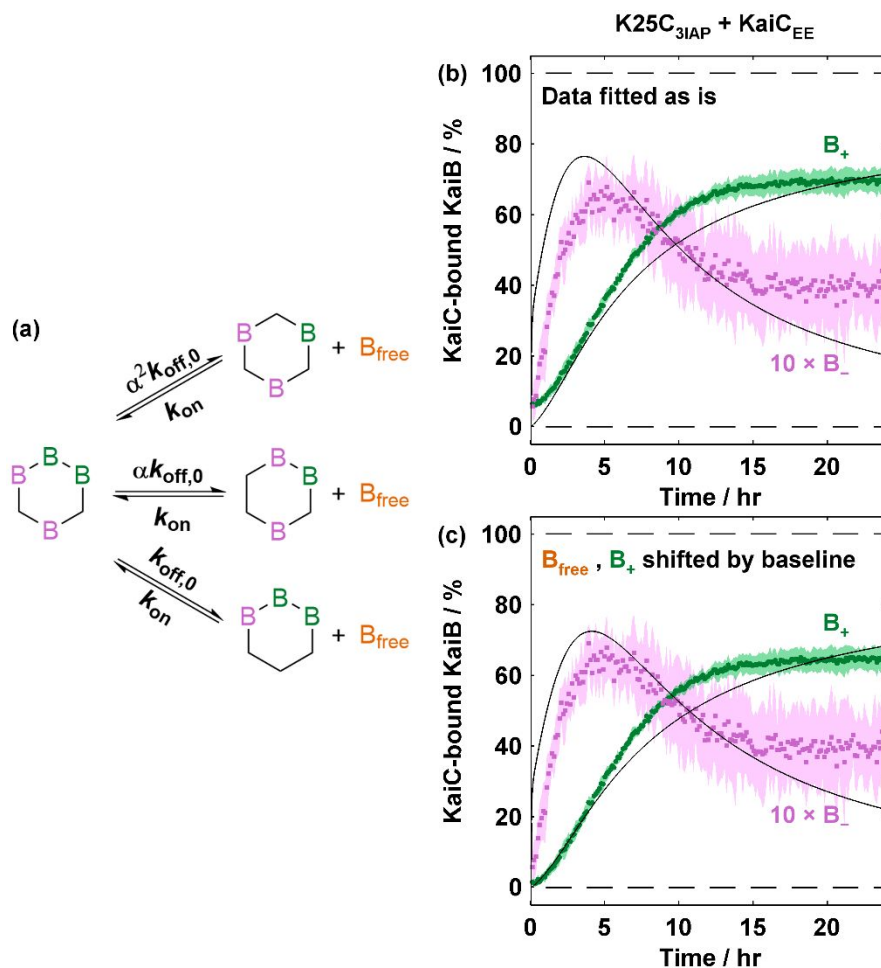


**Fig. S21.** The Koda-Saito model does not adequately explain the observed KaiB-KaiC binding kinetics.

(a) Basic premise of the Koda-Saito model. KaiC hexamers (shown as hexagons here) contain six KaiB-KaiC binding sites represented by the six vertices of the hexagons. Sites occupied by KaiB are denoted with the letter B, with “edge” sites ( $B_-$ ) colored in light purple and “bulk” sites ( $B_+$ ) colored in green. The bimolecular binding rate  $k_{on}$  is independent of the KaiBC stoichiometry. The unimolecular dissociation rate of any KaiB monomer from the KaiBC complex  $k_{off}$  is given by some basic dissociation rate  $k_{off,0}$  that is suppressed by a factor  $\alpha$  for each neighboring KaiB in the KaiBC complex. (b) and (c) Fitting of the K25C<sub>3IAP</sub>-KaiC<sub>EE</sub> 5 $\times$  reaction to the model.  $B_+$ : green circles.  $10 \times B_-$ : light purple squares. The data was fitted as is in (b) whereas the concentration of  $B_+$  was shifted downwards by 5% whereas that of free KaiB was shifted upwards by 5% in (c) to potentially account for baseline  $B_+$  (see Fig. S18). Shaded areas show 95% CI due to inter-sample variability ( $n = 6$ ). Best fits of the kinetic traces are shown as solid black lines. See Table S7 for rate constants.

**Table S7.** Rate constants derived from the basic Koda-Saito model.

Nonlinear least squares fitting of the parameters was performed on the mean of the experimental data based on multiple replicates and multiple models. The 95% confidence interval were derived using the Jacobian matrices. Unless otherwise stated, the weights of the components for the fitting procedure were [1, 1, 10] for free KaiB, B<sub>+</sub> and B<sub>-</sub> due to the low concentration of B<sub>-</sub>.

Experiment	Figure	Fitted parameter			NRMSD	
		Parameter / unit	Best fit	95% CI		
K25C <sub>3IAP</sub> + KaiC <sub>EE</sub> , 1:1	S21b	$k_{on} / \mu\text{M}^{-1}\text{hr}^{-1}$	0.037	0.034	0.039	0.353
		$k_{off,0} / \text{hr}^{-1}$	18	16	19	
		$\alpha$	10 <sup>-6#</sup>	#	#	
K25C <sub>3IAP</sub> + KaiC <sub>EE</sub> , 1:1, B <sub>+</sub> and B <sub>free</sub> Shifted by 5%	S21c	$k_{on} / \mu\text{M}^{-1}\text{hr}^{-1}$	0.033	0.031	0.035	0.308
		$k_{off,0} / \text{hr}^{-1}$	18	17	19	
		$\alpha$	10 <sup>-6#</sup>	#	#	

# Poorly constrained (reached lower or upper bound of parameter search space).

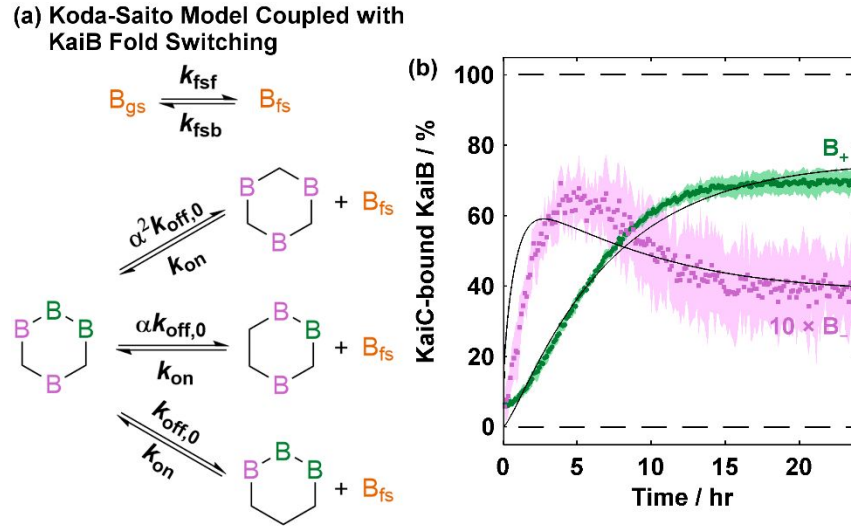


**Fig. S22.** Koda-Saito with monomeric KaiB fold switching.

(a) Koda-Saito model with monomeric KaiB fold switching. This model combines the monomeric KaiB fold switching model by Chang et al. (2015) with the Koda-Saito model. Fold switching is characterized by two rate constants, forward fold switching ( $k_{fsf}$ ) and reverse fold switching ( $k_{fsb}$ ). The two forms are assumed to be spectroscopically indistinguishable. Fold-switched KaiB can then bind to KaiC in the fashion described by Koda and Saito (2020, see Fig. S21). (b) Fitting of the K25C<sub>3IAP</sub>-KaiC<sub>EE</sub> 5× reaction to the model. B<sub>+</sub>: green circles. 10 × B<sub>-</sub>: light purple squares. Shaded areas show 95% CI due to inter-sample variability ( $n = 6$ ). Best fits of the kinetic traces are shown as solid black lines. See Table S8 for rate constants.

**Table S8.** Rate constants derived from the Koda-Saito model with monomeric KaiB fold switching.

Nonlinear least squares fitting of the parameters was performed on the mean of the experimental data based on multiple replicates and multiple models. The 95% confidence interval were derived using the Jacobian matrices. Unless otherwise stated, the weights of the components for the fitting procedure were [1, 1, 10] for free KaiB, B<sub>+</sub> and B<sub>-</sub> due to the low concentration of B<sub>-</sub>.

Experiment	Figure	Parameter / unit	Fitted Parameter			NRMSD
			Best fit	95% CI		
K25C <sub>3IAP</sub> + KaiC <sub>EE</sub> , 1:1	S22b	$k_{on} / \mu\text{M}^{-1}\text{hr}^{-1}$	62.1	58.3	66.0	0.177
		$k_{off,0} / \text{hr}^{-1}$	87.1	75.7	100.2	
		$\alpha$	0.0246	0.0239	0.0254	
		$k_{fsf} / \text{hr}^{-1}$	0.137	0.131	0.144	
		$k_{fsb} / \text{hr}^{-1}$	10.5	8.3	13.2	

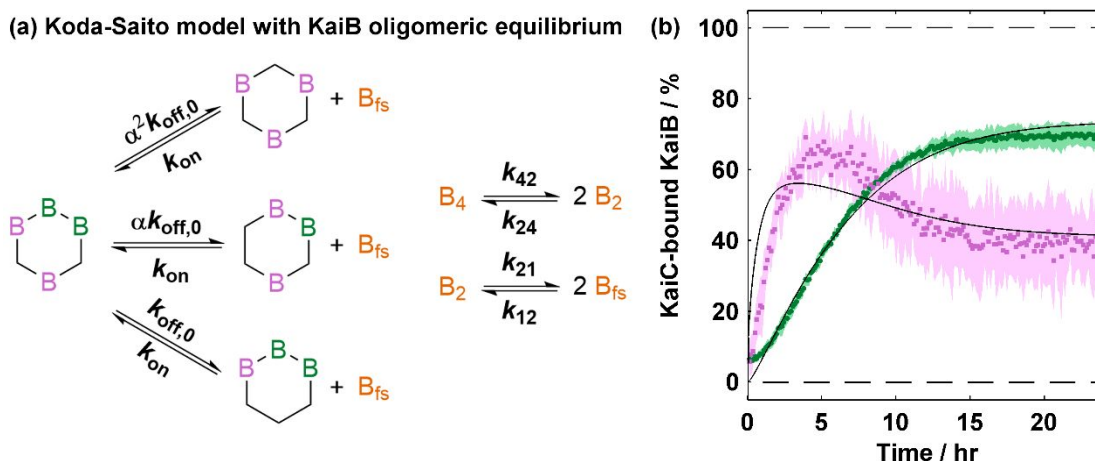


**Fig. S23.** Koda-Saito with tetramer-dimer-monomer KaiB equilibrium.

(a) Koda-Saito model with KaiB tetramer-dimer-monomer equilibrium. This model combines the tetramer-dimer-monomer equilibrium of KaiB with the Koda-Saito model. The tetramer-dimer-monomer equilibrium is characterized by 4 rate constants,  $k_{42}$ ,  $k_{24}$ ,  $k_{21}$  and  $k_{12}$ , and 2 equilibrium constants,  $K_{42} = k_{42}/k_{24}$  and  $K_{21} = k_{21}/k_{12}$ . The three forms of free KaiB are assumed to be spectroscopically indistinguishable. Monomeric KaiB can then bind to KaiC in the fashion described by Koda and Saito (2020, see Fig. S21). (b) Fitting of the  $K25C_{3IAP}$ -KaiC<sub>EE</sub>  $5\times$  reaction to the model. B<sub>+</sub>: green circles.  $10\times$  B<sub>-</sub>: light purple squares. Shaded areas show 95% CI due to inter-sample variability ( $n = 6$ ). Best fits of the kinetic traces are shown as solid black lines. See Table S9 for rate constants.

**Table S9.** Rate constants derived from the Koda-Saito model with tetramer-dimer-monomer KaiB equilibrium.

Nonlinear least squares fitting of the parameters was performed on the mean of the experimental data based on multiple replicates and multiple models. The 95% confidence interval were derived using the Jacobian matrices. Unless otherwise stated, the weights of the components for the fitting procedure were [1, 1, 10] for free KaiB, B<sub>+</sub> and B<sub>-</sub> due to the low concentration of B<sub>-</sub>.

Experiment	Figure	Fitted Parameter			NRMSD	
		Parameter / unit	Best fit	95% CI		
<b>K25C<sub>3IAP</sub> + KaiC<sub>EE</sub>, 1:1</b>	S23b	$k_{on} / \mu\text{M}^{-1}\text{hr}^{-1}$	33.0	21.1	51.7	0.148
		$k_{off,0} / \text{hr}^{-1}$	119	101	141	
		$\alpha$	0.0259	0.0253	0.0266	
		$K_{42} / \mu\text{M}$	0.019	&	&	
		$k_{24} / \text{hr}^{-1}$	440	&	&	
		$K_{21} / \mu\text{M}$	0.12	&	&	
		$k_{12} / \text{hr}^{-1}$	35	7.9	154	

& Poorly constrained (Jacobian-derived 95% CI spans over 3 orders of magnitude).

(a) KaiC conformational equilibrium with Koda-Saito model

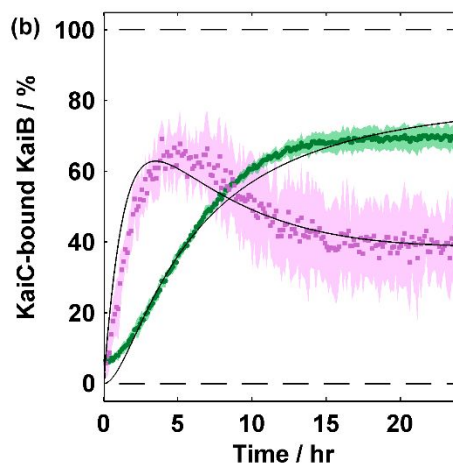
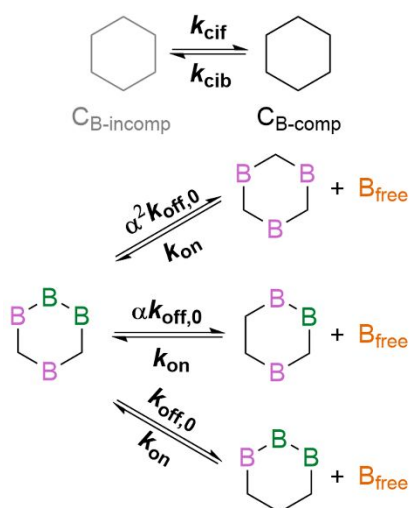


**Fig. S24.** Koda-Saito with KaiC conformational equilibrium.

(a) Koda-Saito model with KaiC conformational equilibrium. This model combines KaiC conformational equilibrium with the Koda-Saito model. KaiC has previously been modeled as existing in an equilibrium between two states, one of which is KaiA-binding competent whereas the other is KaiB-binding competent (Lin et al., 2014). This is incorporated by describing this equilibrium with two rate constants,  $k_{cif}$  and  $k_{cib}$ , alluding to the necessity of CI ATPase activity for converting to the KaiB-binding competent state. Monomeric KaiB cannot bind to the KaiB-binding incompetent state ( $C_{B-incomp}$ , grey) but it can bind to the KaiB-binding competent KaiC ( $C_{B-comp}$ , black) in the fashion described by Koda and Saito (2020, see Fig. S21). (b) Fitting of the K25C<sub>31AP</sub>-KaiC<sub>EE</sub> 5× reaction to the model. B<sub>+</sub>: green circles. 10 × B<sub>-</sub>: light purple squares. Shaded areas show 95% CI due to inter-sample variability ( $n = 6$ ). Best fits of the kinetic traces are shown as solid black lines. See Table S10 for rate constants.

**Table S10.** Rate constants derived from the Koda-Saito model with KaiC conformational equilibrium.

Nonlinear least squares fitting of the parameters was performed on the mean of the experimental data based on multiple replicates and multiple models. The 95% confidence interval were derived using the Jacobian matrices. Unless otherwise stated, the weights of the components for the fitting procedure were [1, 1, 10] for free KaiB, B<sub>+</sub> and B<sub>-</sub> due to the low concentration of B<sub>-</sub>.

Experiment	Figure	Fitted Parameter			NRMSD
		Parameter / unit	Best fit	95% CI	
K25C <sub>31AP</sub> + KaiC <sub>EE</sub> , 1:1	S24b	$k_{on} / \mu\text{M}^{-1}\text{hr}^{-1}$	0.0581	0.0566	0.0596
		$k_{off,0} / \text{hr}^{-1}$	0.77	0.54	1.10
		$\alpha$	0.085	0.070	0.103
		$k_{cif} / \text{hr}^{-1}$	0.35	0.27	0.46
		$k_{cib} / \text{hr}^{-1}$	4.8	2.8	8.2

(a) Koda-Saito Model with KaiB fold-switching and KaiC conformational switching

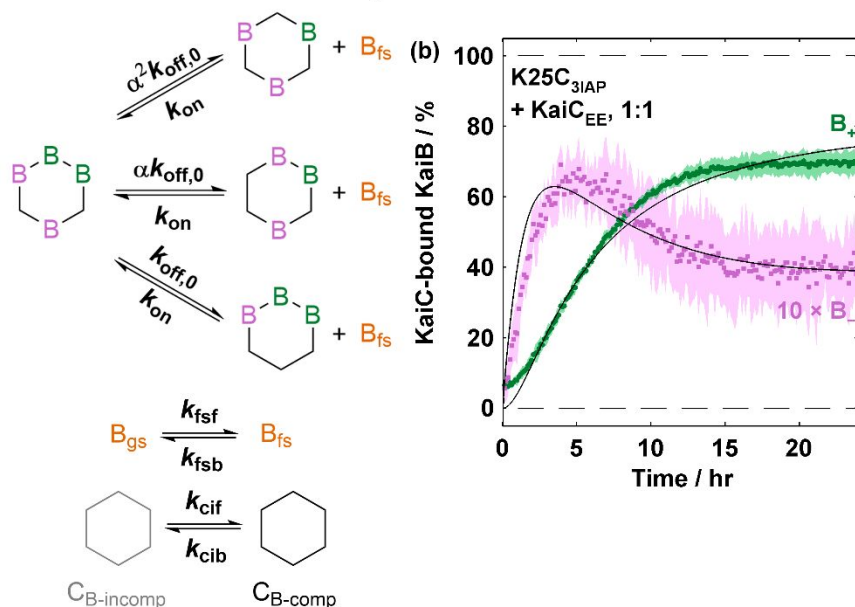


**Fig. S25.** Koda-Saito with KaiB fold switching equilibrium and KaiC conformational equilibrium.

(a) Koda-Saito model with KaiB fold switching equilibrium and KaiC conformational equilibrium. This model combines KaiC conformational equilibrium (Fig. S24) and KaiB fold switching equilibrium (Fig. S22) with the Koda-Saito model (Fig. S21). (b) Fitting of the  $K25C_{3IAP}$ -KaiC<sub>EE</sub> 5× reaction to the model. B<sub>+</sub>: green circles. 10 × B<sub>-</sub>: light purple squares. Shaded areas show 95% CI due to inter-sample variability ( $n = 6$ ). Best fits of the kinetic traces are shown as solid black lines. See Table S11 for rate constants.

**Table S11.** Rate constants derived from the Koda-Saito model with KaiB fold switching equilibrium and KaiC conformational equilibrium.

Nonlinear least squares fitting of the parameters was performed on the mean of the experimental data based on multiple replicates and multiple models. The 95% confidence interval were derived using the Jacobian matrices. Unless otherwise stated, the weights of the components for the fitting procedure were [1, 1, 10] for free KaiB, B<sub>+</sub> and B<sub>-</sub> due to the low concentration of B<sub>-</sub>.

Experiment	Figure	Fitted Parameter			NRMSD
		Parameter / unit	Best fit	95% CI	
K25C <sub>3IAP</sub> + KaiC <sub>EE</sub> , 1:1	S25b	$k_{on} / \mu M^{-1} hr^{-1}$	0.06	&	&
		$k_{off,0} / hr^{-1}$	0.77	0.50	1.18
		$\alpha$	0.085	0.070	0.104
		$k_{fsf} / hr^{-1}$	10	&	&
		$k_{fsb} / hr^{-1}$	0.009	&	&
		$k_{cif} / hr^{-1}$	0.35	0.26	0.49
		$k_{cib} / hr^{-1}$	4.8	2.7	8.7

& Poorly constrained (Jacobian-derived 95% CI spans over 3 orders of magnitude).



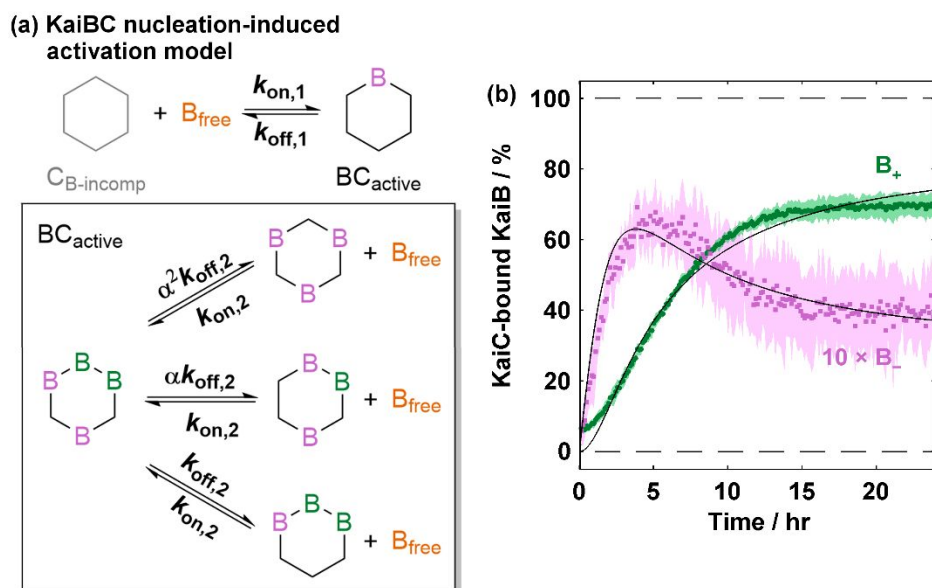


**Fig. S26.** Koda-Saito with KaiB-KaiC nucleation-induced KaiC activation model. (a) Koda-Saito model with KaiB-KaiC nucleation-induced KaiC activation model.

This model assumes that KaiB-KaiC binding follows the Koda-Saito model (Fig. S21) but the nucleation event ( $B_{\text{free}} + C_6 \rightleftharpoons B_1C_6$ ) possesses different binding and dissociation rates from further binding and dissociation events. The nucleation event thus “activates” KaiC for further KaiB binding and can be framed as an induced fit model. (b) Fitting of the K25C<sub>31AP</sub>-KaiC<sub>EE</sub> 5× reaction to the model. B<sub>+</sub>: green circles. 10 × B<sub>-</sub>: light purple squares. Shaded areas show 95% CI due to inter-sample variability ( $n = 6$ ). Best fits of the kinetic traces are shown as solid black lines. See Table S12 for rate constants.

**Table S12.** Rate constants derived from the Koda-Saito with KaiB-KaiC nucleation-induced KaiC activation model.

Nonlinear least squares fitting of the parameters was performed on the mean of the experimental data based on multiple replicates and multiple models. The 95% confidence interval were derived using the Jacobian matrices. Unless otherwise stated, the weights of the components for the fitting procedure were [1, 1, 10] for free KaiB, B<sub>+</sub> and B<sub>-</sub> due to the low concentration of B<sub>-</sub>.

Experiment	Figure	Fitted Parameter			NRMSD
		Parameter / unit	Best fit	95% CI	
K25C <sub>31AP</sub> + KaiC <sub>EE</sub> , 1:1	S26b	$k_{\text{on},1} / \mu\text{M}^{-1}\text{hr}^{-1}$	0.00231	0.00224	0.00237
		$k_{\text{off},1} / \text{hr}^{-1}$	0.023	0.010	0.051
		$k_{\text{on},2} / \mu\text{M}^{-1}\text{hr}^{-1}$	0.0744	0.0719	0.0770
		$k_{\text{off},2} / \text{hr}^{-1}$	160	90	290
		$\alpha$	0.00174	0.00101	0.00299

**Table S13.** Rate constants derived from the Koda-Saito model coupled with KaiB-KaiC encounter complex formation and induced fit nucleation.

Nonlinear least squares fitting of the parameters was performed on the mean of the experimental data based on multiple replicates and multiple models. The 95% confidence intervals were derived using the Jacobian matrices. Unless otherwise stated, the weights of the components for the fitting procedure were [1, 1, 10] for free KaiB, B<sub>+</sub> and B<sub>-</sub> due to the low concentration of B<sub>-</sub>.

Experiment	Figure	Parameter / unit	Fitted Parameter		NRMSD
			Best fit	95% CI	
K25C <sub>3IAP</sub> + KaiC <sub>ST</sub> , 1:1		$k_{on1} / \mu\text{M}^{-1}\text{hr}^{-1}$	0.007	0.002	0.025
		$k_{off1} / \text{hr}^{-1}$	0.04	&	&
		$k_{c,on} / \text{hr}^{-1}$	1	0.008	200
		$k_{c,off} / \text{hr}^{-1}$	20	0.1	3000
		$k_{on2} / \mu\text{M}^{-1}\text{hr}^{-1}$	0.18	0.15	0.21
		$k_{off2} / \text{hr}^{-1}$	210	100	430
		$\alpha$	0.0079	0.0048	0.013
K25C <sub>3IAP</sub> + KaiC <sub>EE</sub> , 1:1	3a	$k_{on1} / \mu\text{M}^{-1}\text{hr}^{-1}$	0.007	0.0002	0.24
		$k_{off1} / \text{hr}^{-1}$	0.02	&	&
		$k_{c,on} / \text{hr}^{-1}$	1	0.009	100
		$k_{c,off} / \text{hr}^{-1}$	4.2	0.20	85
		$k_{on2} / \mu\text{M}^{-1}\text{hr}^{-1}$	0.091	0.068	0.122
		$k_{off2} / \text{hr}^{-1}$	18.0	11.5	28.0
		$\alpha$	0.016	0.012	0.022
K25C <sub>3IAP</sub> + KaiC <sub>EA</sub> , 1:1		$k_{on1} / \mu\text{M}^{-1}\text{hr}^{-1}$	0.004	0.0003	0.05
		$k_{off1} / \text{hr}^{-1}$	0.09	0.007	1
		$k_{c,on} / \text{hr}^{-1}$	1	0.02	60
		$k_{c,off} / \text{hr}^{-1}$	10	1	100
		$k_{on2} / \mu\text{M}^{-1}\text{hr}^{-1}$	0.15	0.12	0.18
		$k_{off2} / \text{hr}^{-1}$	133	96	184
		$\alpha$	0.0060	0.0047	0.0077

& Poorly constrained (Jacobian-derived 95% CI spans over 3 orders of magnitude).

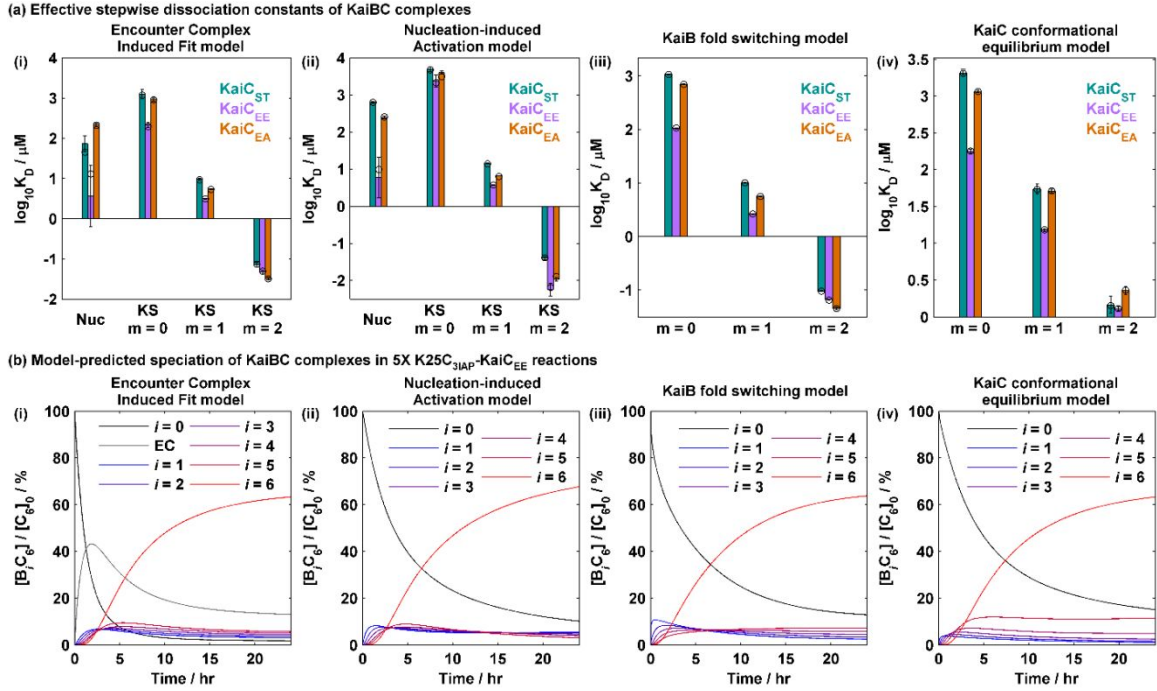
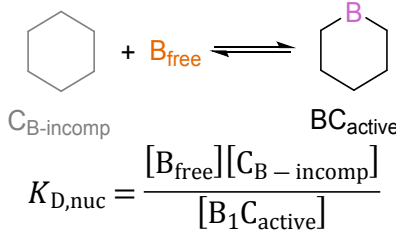


**Fig. S27.** Hyperphosphorylated KaiC is more competent in KaiB-KaiC binding nucleation than unphosphorylated or S431-phosphorylated KaiC.

(a) The effective dissociation constants for each step in KaiB-KaiC binding are plotted as bar graphs for KaiC<sub>ST</sub> (turquoise), KaiC<sub>EE</sub> (purple) and KaiC<sub>EA</sub> (orange). Error bars show standard deviation estimated by bootstrap resampling the original dataset 20 times (see Table S14). Best fit results are shown as black open circles. (i) Encounter complex induced fit model (Fig. 3a-b). Figure reproduced from Fig. 4a. (ii) Nucleation-induced activation model (Fig. S26). (iii) Conformational selection via KaiB fold switching (Fig. S22). (iv) Conformational selection via KaiC conformational equilibrium (Fig. S24). (b) Speciation of KaiB-KaiC<sub>EE</sub> complexes predicted by respective KaiB-KaiC binding models. The definitions of the dissociation constants in (a) are as follows: In (i) and (ii), two classes of dissociation constants can be defined: The initial (seeding / nucleation) dissociation constant  $K_{D,nuc}$  can be defined for the following reaction:



For (i), the overall dissociation constant accounts for both the encounter complex equilibrium and the induced fit step:

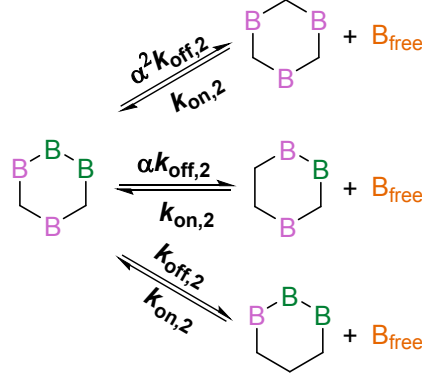
$$K_{D,nuc} = \frac{[B_{\text{free}}][C_{B\text{-incomp}}]}{[B_{\text{weak}} C_{\text{inactive}}]} \times \frac{[B_{\text{weak}} C_{\text{inactive}}]}{[B_1 C_{\text{active}}]}$$

$$= K_{D,\text{weak}} K_C = \frac{k_{\text{off},1}}{k_{\text{on},1}} \times \frac{k_{c,\text{off}}}{k_{c,\text{on}}}$$

For (ii), the dissociation constant for the single nucleation-activation step is

$$K_{D,\text{nuc}} = \frac{k_{\text{off},1}}{k_{\text{on},1}}$$

The subsequent Koda-Saito dissociation constants  $K_{D,\text{KS},m}$  ( $m = 0, 1$  or  $2$ ) can be defined by the reactions:



$$K_{\text{KS}}(m) = \frac{[B_{\text{free}}][B_i C]}{[B_{i+1} C]} = \alpha^m \frac{k_{\text{off}}}{k_{\text{on}}}$$

The latter dissociation constants also apply to conformational selection models in (iii) and (iv). However, these dissociation constants require corrections for the associated conformational equilibrium. For (iii), the effective dissociation constants are

$$K_{\text{KS,eff}}(m) = \frac{[B_{\text{gs}}][B_i C]}{[B_{i+1} C]} = \alpha^m \frac{k_{\text{off}}}{k_{\text{on}}} \times \frac{k_{\text{fsb}}}{k_{\text{fsf}}}$$

For (iv), the effective dissociation constants are

$$K_{\text{KS,eff}}(m) = \frac{[B][B_i C]}{[B_{i+1} C]} \times \frac{[C_{\text{inactive}}]}{[C_{\text{active}}]} = \alpha^m \frac{k_{\text{off}}}{k_{\text{on}}} \times \frac{k_{\text{cib}}}{k_{\text{cif}}}$$

**Table S14.** Bootstrap resampling derived KaiB-KaiC dissociation constants.

Nonlinear least squares fitting of the parameters was performed on the mean of the experimental data based on multiple replicates and multiple models. The dissociation constants shown were derived via bootstrap resampling the original data ( $n_{\text{bootstrap}} = 20$ ) and displayed in the format of mean  $\pm$  standard deviation. Unless otherwise stated, the weights of the components for the fitting procedure were [1, 1, 10] for free KaiB, B<sub>+</sub> and B<sub>-</sub> due to the low concentration of B<sub>-</sub>.

Model	Figure	log <sub>10</sub> (K <sub>D</sub> / $\mu$ M)	Experiment		
			KaiC <sub>ST</sub>	KaiC <sub>EE</sub>	KaiC <sub>EA</sub>
<b>Encounter Complex Induced Fit</b>	4a-b S27i	$K_{D,\text{nuc}}$	1.86 $\pm$ 0.19	0.56 $\pm$ 0.76	2.326 $\pm$ 0.039
		$K_{D,\text{KS},m=0}$	3.09 $\pm$ 0.11	2.326 $\pm$ 0.063	2.961 $\pm$ 0.043
		$K_{D,\text{KS},m=1}$	0.977 $\pm$ 0.026	0.497 $\pm$ 0.011	0.732 $\pm$ 0.010
		$K_{D,\text{KS},m=2}$	-1.142 $\pm$ 0.062	-1.332 $\pm$ 0.047	-1.497 $\pm$ 0.029
<b>Nucleation-induced Activation</b>	S26 S27ii	$K_{D,\text{nuc}}$	2.793 $\pm$ 0.027	0.77 $\pm$ 0.55	2.394 $\pm$ 0.034
		$K_{D,\text{KS},m=0}$	3.670 $\pm$ 0.066	3.37 $\pm$ 0.17	3.604 $\pm$ 0.049
		$K_{D,\text{KS},m=1}$	1.150 $\pm$ 0.012	0.566 $\pm$ 0.011	0.8166 $\pm$ 0.0068
		$K_{D,\text{KS},m=2}$	-1.400 $\pm$ 0.045	-2.24 $\pm$ 0.17	-1.971 $\pm$ 0.051
<b>Conformational selection, KaiB fold switching*</b>	S22 S27iii	$K_{D,\text{KS},m=0}$	3.0302 $\pm$ 0.0094	2.019 $\pm$ 0.011	2.8431 $\pm$ 0.0080
		$K_{D,\text{KS},m=1}$	1.0058 $\pm$ 0.0045	0.4197 $\pm$ 0.0086	0.751 $\pm$ 0.012
		$K_{D,\text{KS},m=2}$	-1.019 $\pm$ 0.011	-1.1792 $\pm$ 0.0076	-1.341 $\pm$ 0.023
<b>Conformational selection, KaiC conformational equilibrium</b>	S24 S27iv	$K_{D,\text{KS},m=0}$	3.314 $\pm$ 0.025	2.249 $\pm$ 0.031	3.059 $\pm$ 0.016
		$K_{D,\text{KS},m=1}$	1.738 $\pm$ 0.070	1.180 $\pm$ 0.018	1.710 $\pm$ 0.026
		$K_{D,\text{KS},m=2}$	0.16 $\pm$ 0.12	0.111 $\pm$ 0.029	0.360 $\pm$ 0.054

\* KaiB fold switching rate constants were fixed to best-fit values obtained from KaiC<sub>EE</sub> (Table S8).

3.5 KaiC<sub>SPT</sub> is ineffective at seeding KaiB-KaiC interactions during the day-to-night transition

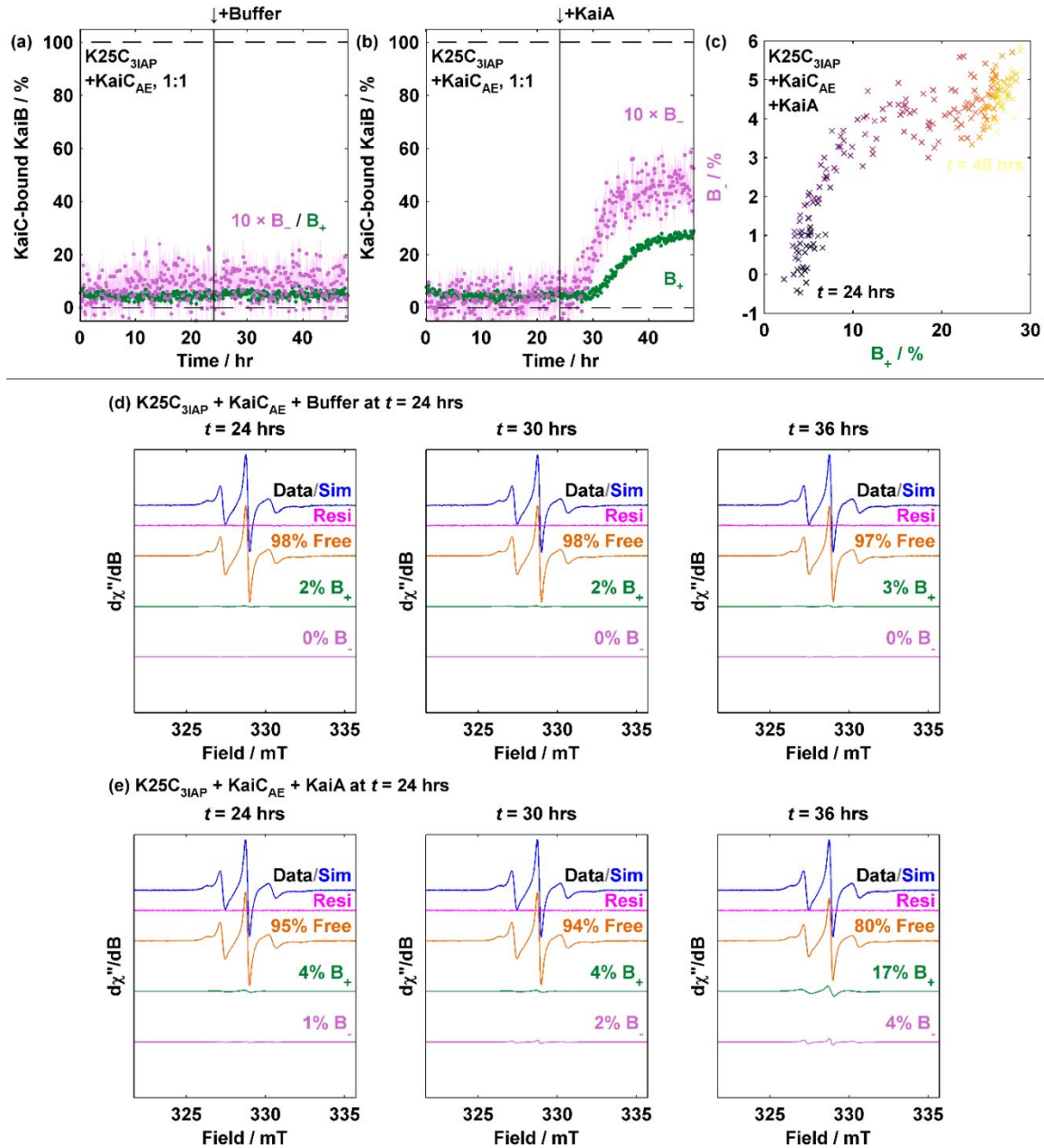


**Fig. S28.** KaiB-KaiC<sub>AE</sub> binding requires the presence of KaiA.

(a) and (b) Plot of concentration (in % relative to total KaiB) of B<sub>+</sub> (green circles) and B<sub>-</sub> (light purple squares) over time with (a) buffer or (b) KaiA spiking at  $t = 24$  hrs. The concentration of B<sub>-</sub> has been multiplied by 10 for illustration purpose. In both panels, shaded areas represent 95% CI due to imperfect signal-to-noise. (c) Correlation of B<sub>+</sub> and B<sub>-</sub> in the ternary KaiA-KaiB-KaiC<sub>AE</sub> mixture in (b). From black to purple to yellow: 24 hrs (0 hrs post-KaiA spiking) to 48 hrs (24 hrs after KaiA spiking). (d) and (e) Spectral simulations of K25C<sub>3IAP</sub>-KaiC<sub>AE</sub> reactions in the absence (d) and presence (e) of KaiA.

Experimental spectra are shown in black and overlaid with simulations in blue. The residual is shown in bright magenta. The components are free KaiB (orange), B<sub>+</sub> (green) and B<sub>-</sub> (light purple).

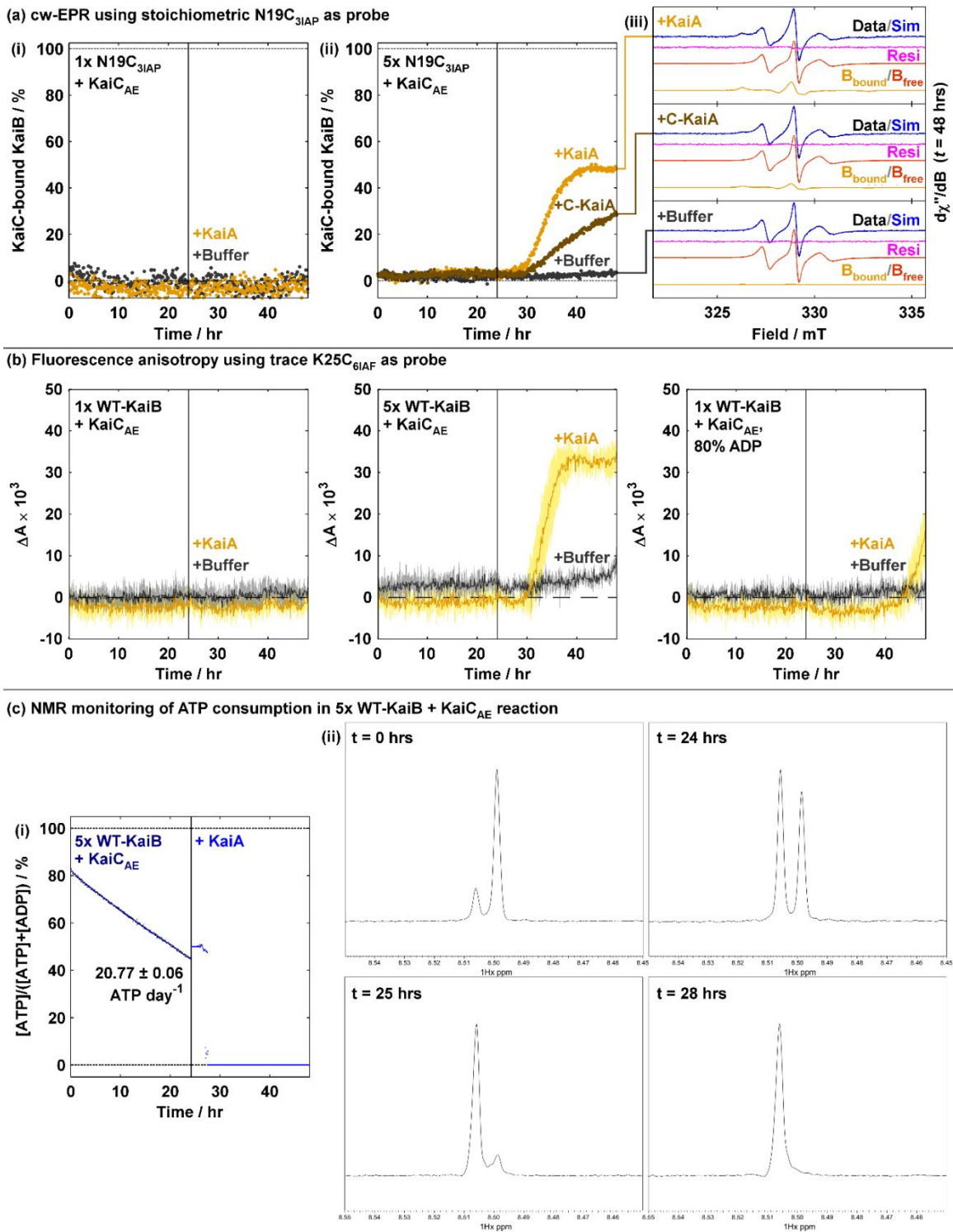


**Fig. S29.** KaiA drives KaiB-KaiC<sub>AE</sub> interactions by multiple mechanisms.

(a) KaiB-N19C-3IAP cw-EPR based KaiB-KaiC<sub>AE</sub> binding assays under (i) 1× and (ii) 5× Kai protein concentrations with full-length KaiA (yellow), KaiA<sub>181-284</sub> (C-KaiA, brown) or buffer (grey) spiking at  $t = 24$  hrs (black line in both panels). (iii) shows



experimental cw-EPR spectra (black) and fit (blue) to free KaiB (red) and KaiC-bound KaiB (yellow), with residual shown in magenta. (b) Fluorescence anisotropy based KaiB-KaiC<sub>AE</sub> binding assays under (i) and (iii) 1× and (ii) 5× Kai protein concentrations with full-length KaiA (yellow) or buffer (grey) spiking at  $t = 24$  hrs (black line in all panels) using 50 nM KaiB-K25C-6IAF as fluorescence probe. In (iii), 200  $\mu$ M ATP and 800  $\mu$ M ADP was used in place of 1 mM ATP in all other panels. In all three panels, basal anisotropy based on KaiB alone were subtracted. Shaded areas show inter-replicate 95% CI ( $n = 3$ ). (c) NMR based ATPase assay to determine ATP consumption in the 5× KaiB-KaiC<sub>AE</sub> reaction. (i) Fraction of ATP to total ATP + ADP in reaction mixture before (dark blue) and after (blue) KaiA addition at  $t = 24$  hrs. The pre-KaiA spiking ATPase activity per molecule of KaiC is estimated by linear regression and reported as mean  $\pm$  95% CI. (ii) Representative <sup>1</sup>H NMR spectra at  $t = 0, 24, 25$  and 28 hrs, the chemical shifts of ATP and ADP are 8.499 ppm and 8.506 ppm, respectively. Note that the ATP concentration in (i) is likely overestimated by the fitting algorithm at  $t = 25$  hrs.

### 3.6 KaiA triggers the night-to-day transition by antagonizing KaiB-KaiC<sub>pST</sub> interactions

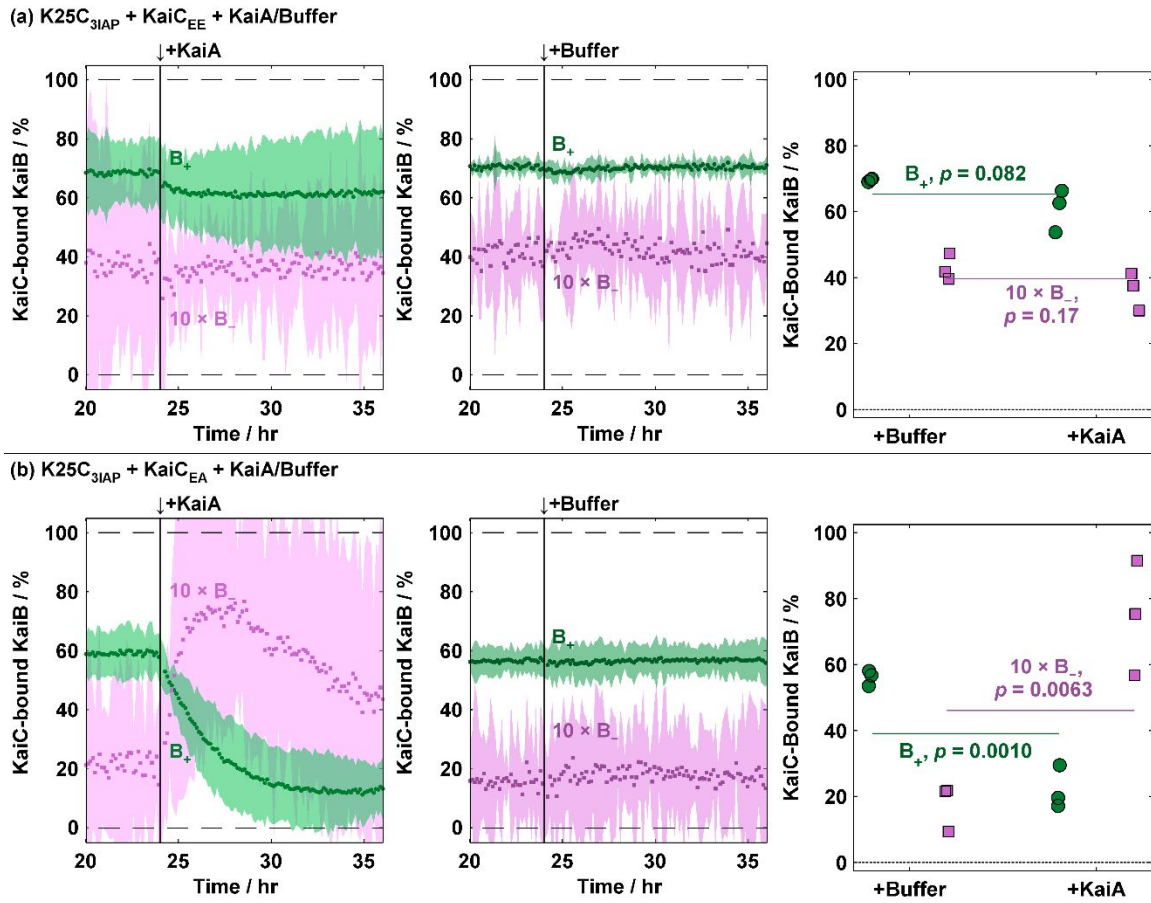
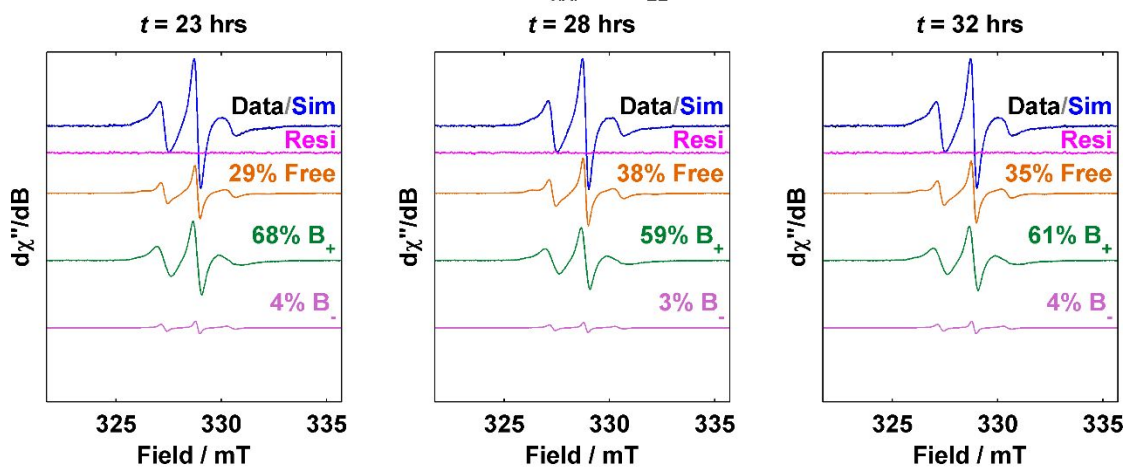


**Fig. S30.** cw-EPR derived kinetics of KaiB-KaiC<sub>EE/EA</sub> binding when exposed to KaiA. (a) and (b) Plot of concentration (in % relative to total KaiB) of B<sub>+</sub> (green circles) and B<sub>-</sub> (light purple squares) over time with between K25C<sub>3IAP</sub> and (a) KaiC<sub>EE</sub> or (b) KaiC<sub>EA</sub> with KaiA (left panels) or buffer (center panels) spiking at  $t = 24$  hrs. In both panels, shaded areas represent inter-replicate 95% CI ( $n = 3$ ). The right panels show two-tailed  $t$ -tests for B<sub>+</sub> and B<sub>-</sub> concentrations after spiking. Spectra were then collected within the 3.5-4 hour-window after spiking and the results were binned. The data in (a) were identical to the ones shown in Fig. 4e in the main text whereas the data in (b) were from a separate series of experiments.

(a) Effect of KaiA spiking (at  $t = 24$  hrs) on  $K25C_{3IAP}$ - $KaiC_{EE}$  reaction mixture



(b) Effect of KaiA spiking (at  $t = 24$  hrs) on  $K25C_{3IAP}$ - $KaiC_{EA}$  reaction mixture

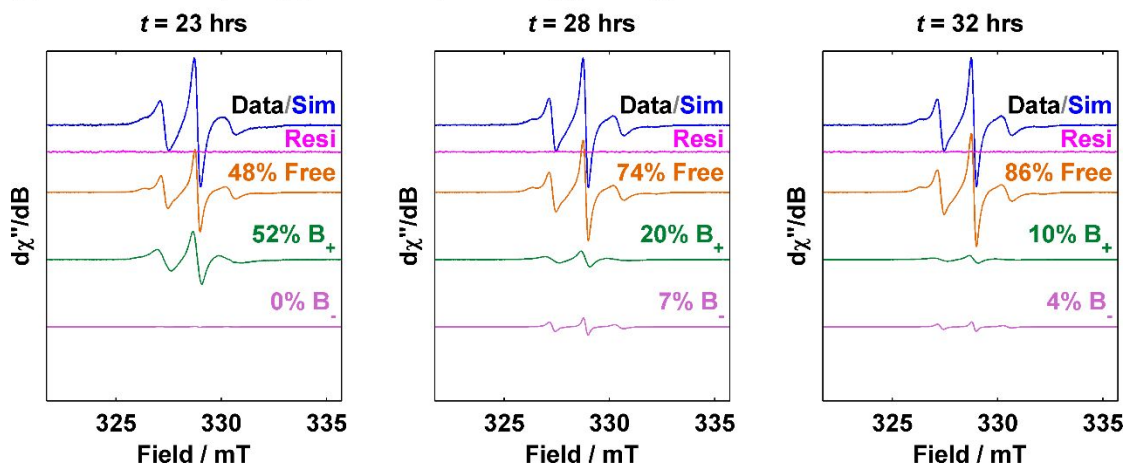


**Fig. S31.** Spectral simulations of  $K25C_{3IAP}$ - $KaiC_{EE/EA}$  reactions with KaiA spiking. Experimental spectra are shown in black and overlaid with simulations in blue. The residual is shown in bright magenta. The basis components are free KaiB (orange),  $B_+$  (green) and  $B_-$  (light purple).

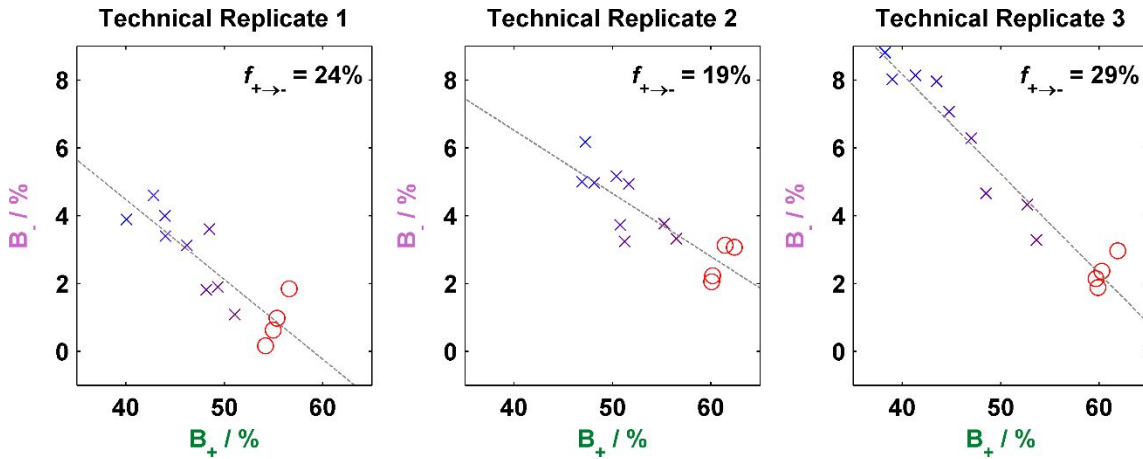


**Fig. S32.** B<sub>-</sub> formation is linearly correlated with B<sub>+</sub> degradation on KaiA-induced antagonization of KaiB-KaiC<sub>EA</sub> interactions.

The concentration of B<sub>-</sub> (light purple) is plotted against that of B<sub>+</sub> (green). Red circles represent kinetics between  $t = 23.5$  hrs to 24 hrs (30 minutes to immediately before KaiA spiking) whereas purple to blue crosses represent kinetics between  $t = 24$  hrs to 25 hrs (0 to 1 hour after spiking). Black dotted line shows fit to linear model. From left to right: 3 technical replicates are shown. The fractional B<sub>+</sub> to B<sub>-</sub> conversion rate,  $f_{+ \rightarrow -}$ , for the  $t = 23.5 - 25$  hrs window is shown in each plot.

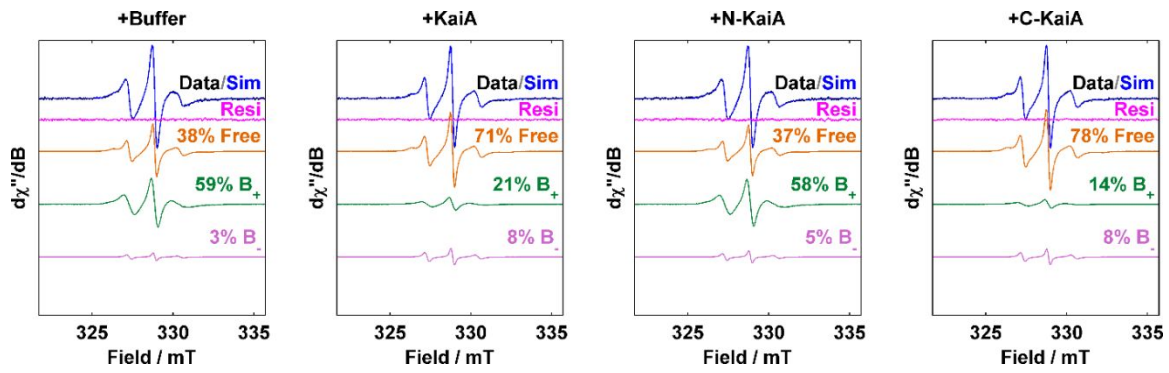


**Fig. S33.** The C-terminal domain of KaiA is most effective in antagonizing KaiB-KaiC<sub>EA</sub> interactions.

From left to right: buffer (control), full-length KaiA, N-terminal domain KaiA (KaiA<sub>1-135</sub>) and C-terminal domain KaiA (KaiA<sub>181-284</sub>). Experimental spectra are shown in black and overlaid with simulations in blue. The residual is shown in bright magenta. The basis components are free KaiB (orange), B<sub>+</sub> (green) and B<sub>-</sub> (light purple).

### 3.7 Interconversion of $B_-$ and $B_+$ in the Kai oscillator

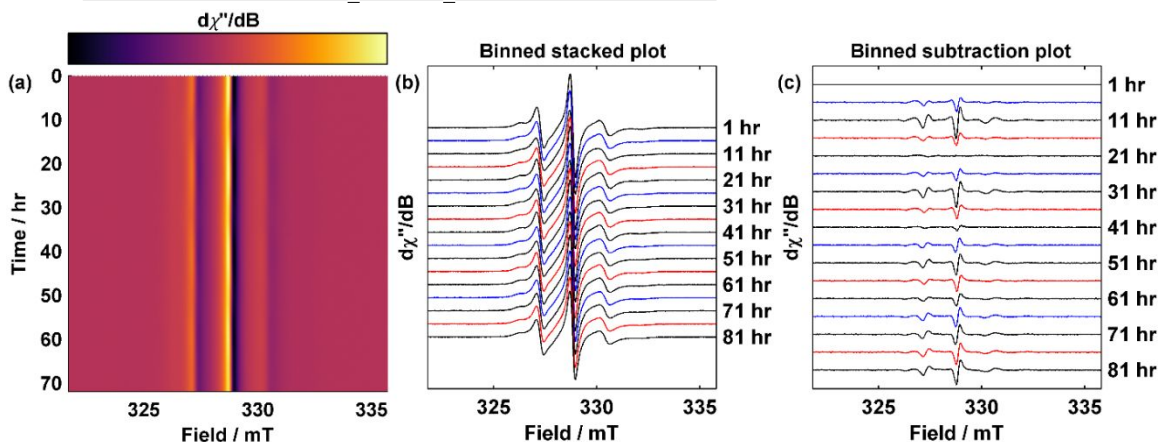


**Fig. S34.** cw-EPR of  $K25C_{31AP}$  oscillator.

(a) and (b) Surface and stacked plots of cw-EPR spectra of  $K25C_{31AP}$  5 $\times$  oscillator (17.5  $\mu$ M  $K25C_{31AP}$ , 17.5  $\mu$ M KaiC and 6.0  $\mu$ M KaiA). (c) Subtraction spectra to emphasize spectral changes by subtracting the spectrum at  $t = 1$  hrs. For (b) and (c), the spectra were binned by 1-hour bins.

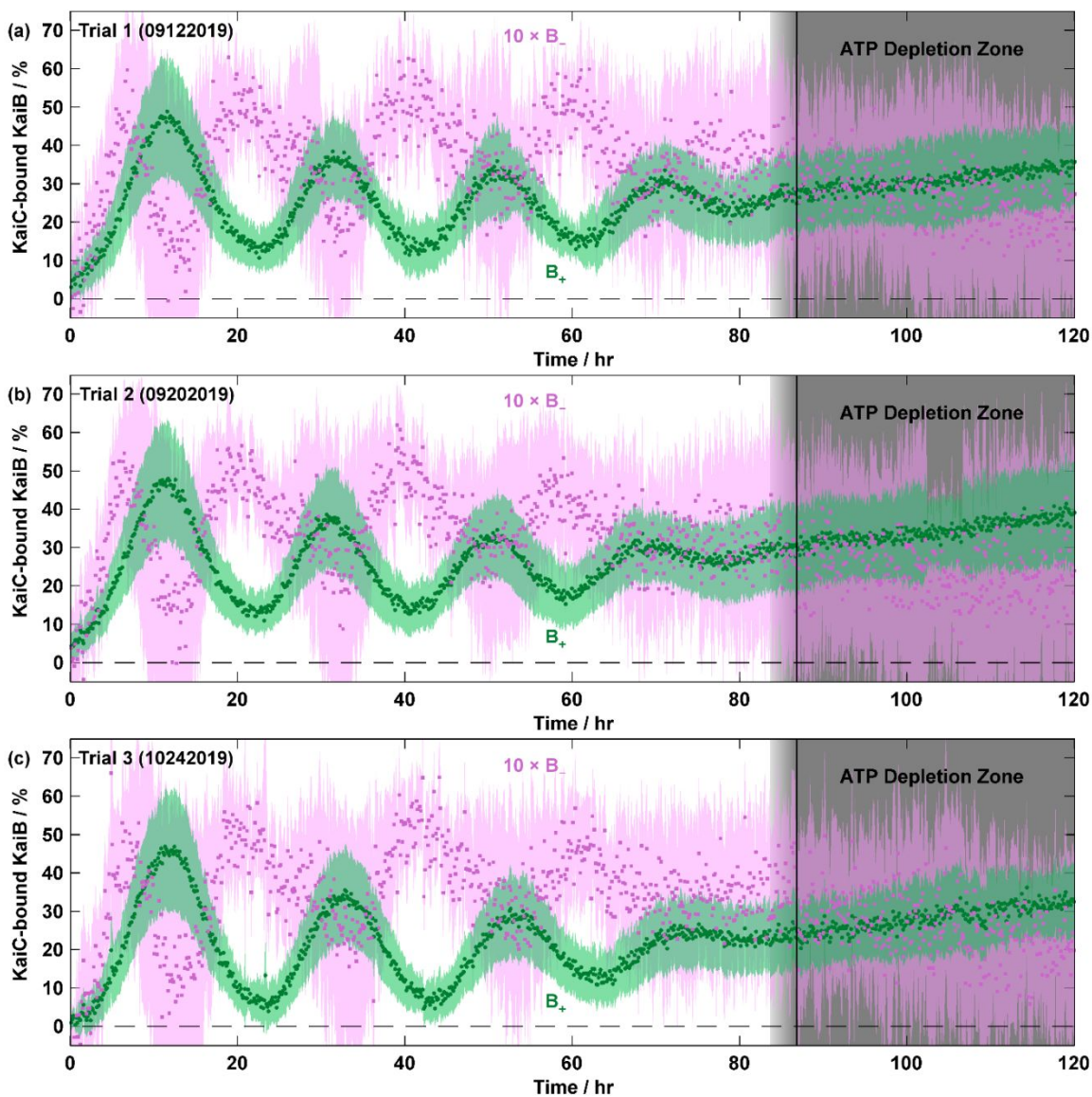


**Fig. S35.** Reproducibility of reconstituted K25C<sub>3IAP</sub> oscillators.

(a)-(c) show three independent technical replicates of the reaction carried out during three different weeks. The subpopulations are B<sub>+</sub> (green circles) and B<sub>-</sub> (magenta squares). Green and magenta shaded areas represent 95% CI as a combination of inter-model uncertainty and S/N error. The black line centered at 87 hours and the grey region to the right of the line refers to time at which ATP is expected to be depleted based on published ATP consumption rate of KaiC at  $15.8 \pm 1.9$  ATP molecules per KaiC per day (SD,  $n = 10$ ).<sup>16</sup> Gradient shade on the left of the black line shows SEM derived from published data.

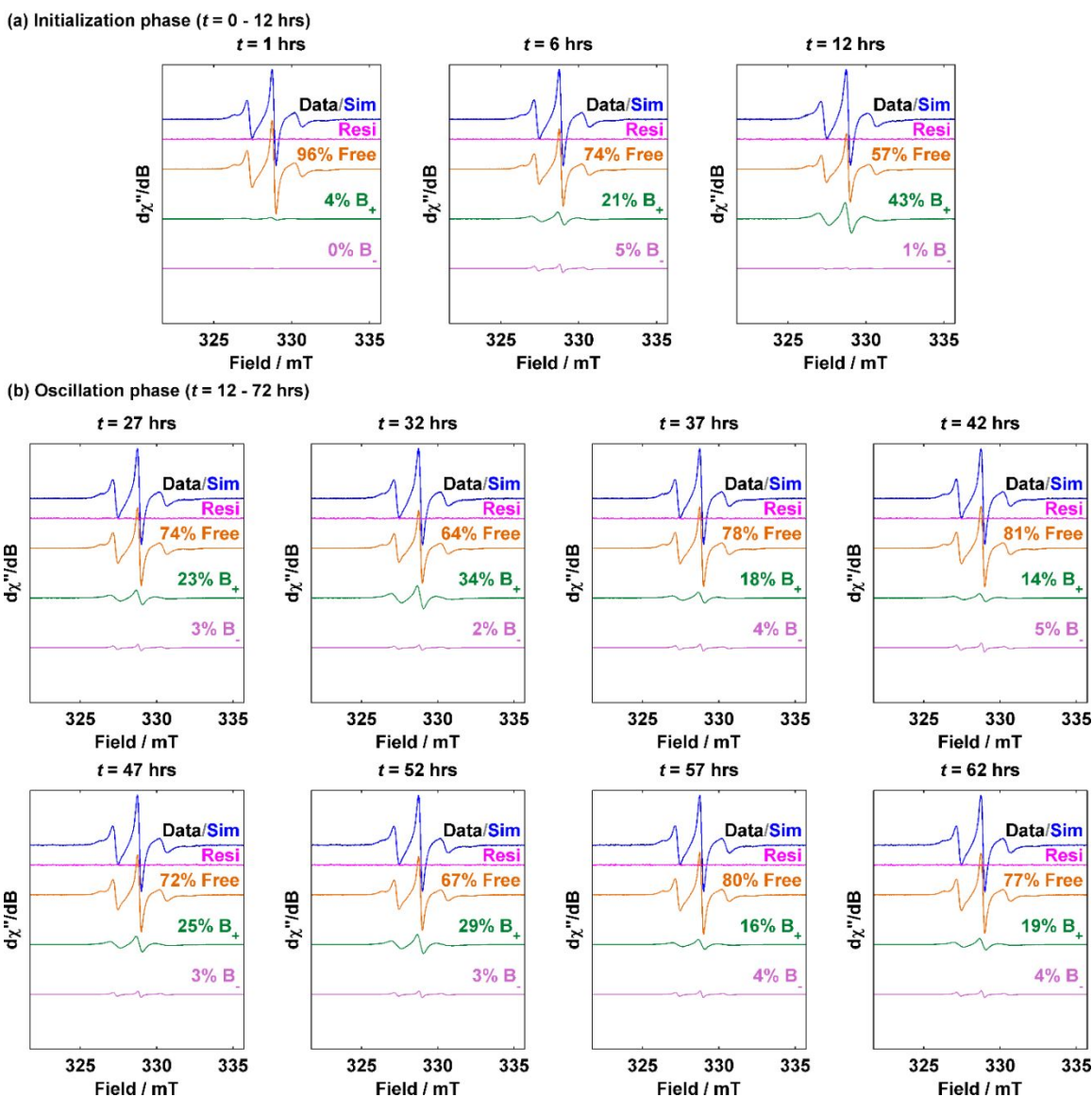


**Fig. S36.** Spectral simulations of the  $K25C_{3IAP}$  reconstituted in vitro oscillator.

Representative cw-EPR spectral simulations of the  $5 \times K25C_{3IAP}$  in vitro oscillator. (a) and (b) show respectively the initialization phase ( $t = 0 - 12$  hrs) and oscillation phase ( $t = 12 - 72$  hrs). Experimental spectra are shown in black and overlaid with simulations in blue. The residual is shown in bright magenta. The basis components are free KaiB (orange), B<sub>+</sub> (green) and B<sub>-</sub> (light purple).



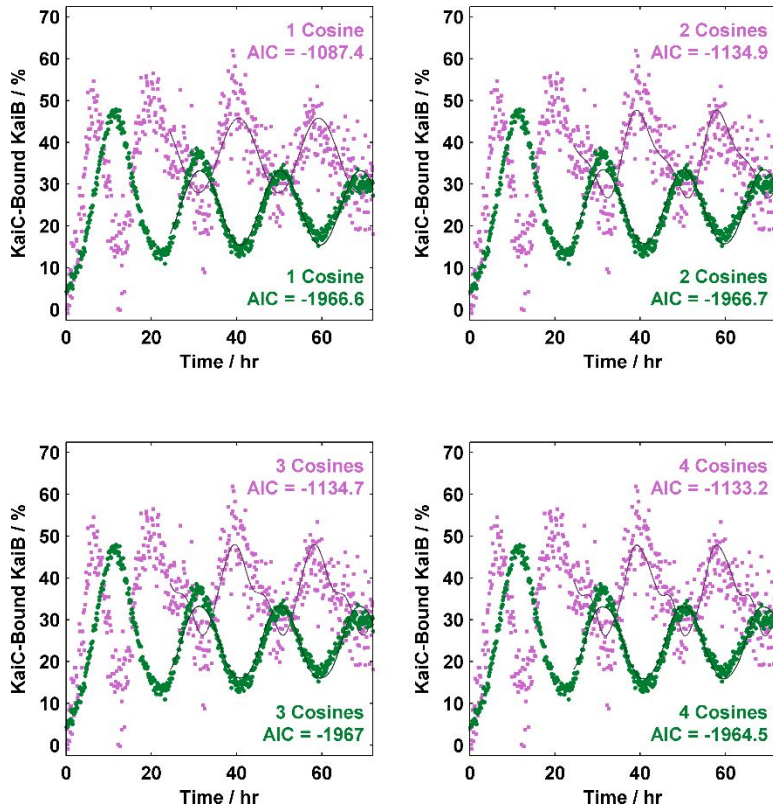


**Fig. S37.** Fit of dynamics of subpopulations of KaiC-bound KaiB to sum of cosines (MFourFit) using 1-4 cosines.

B<sub>+</sub>: green circles. B<sub>-</sub>: magenta squares. B<sub>-</sub> has been multiplied by 10 for illustration purpose. See Table S15 for fitting parameters.

**Table S15.** mFourfit parameters of K25C<sub>3IAP</sub> 5× oscillator.

K25C<sub>3IAP</sub> 5× oscillator mFourfit parameters for oscillation of fraction of KaiC-bound KaiB over time determined by nonlinear least squares for three independent trials. Parameters shown were determined from unbinned data between  $t = 24 - 72$  hrs ( $\sim 0.125$  hour per point). Errors shown are 95% confidence interval (CI) via the Jacobian matrix.

Trial 1 (09122019, Fig. S35a)

q	B <sub>+</sub>				10 × B <sub>-</sub>			
	1	2	3	4	1	2	3	4
C / %	23.4 ± 0.2	23.5 ± 0.2	23.5 ± 0.2	23.5 ± 0.2	39.3 ± 0.7	39.3 ± 0.7	39.4 ± 0.7	39.4 ± 0.7
T / hr	19.48 ± 0.12	19.48 ± 0.12	19.49 ± 0.12	19.48 ± 0.12	18.99 ± 0.36	19.31 ± 0.39	19.21 ± 0.35	19.28 ± 0.33
A <sub>1</sub> / %	-9.7 ± 0.3	-9.6 ± 0.3	-9.6 ± 0.3	-9.6 ± 0.3	11.0 ± 1.0	11.1 ± 1.0	11.1 ± 1.0	11.2 ± 1.0
φ <sub>1</sub> / hr	2.72 ± 0.29	2.72 ± 0.28	2.70 ± 0.28	2.71 ± 0.28	3.19 ± 0.89	2.45 ± 0.95	2.66 ± 0.88	2.53 ± 0.82
A <sub>2</sub> / %	-	0.3 ± 0.3	0.3 ± 0.3	0.3 ± 0.3	-	2.5 ± 1.0	2.3 ± 1.0	2.3 ± 1.0
φ <sub>2</sub> / hr	-	1.52 ± 1.44	1.65 ± 1.49	1.65 ± 1.50	-	0.38 ± 1.16	0.61 ± 1.10	0.46 ± 1.03
A <sub>3</sub> / %	-	-	-0.2 ± 0.3	-0.2 ± 0.3	-	-	-1.0 ± 1.0	-0.9 ± 1.0
φ <sub>3</sub> / hr	-	-	-0.33 ± 1.42	-0.24 ± 1.45	-	-	0.02 ± 1.43	0.08 ± 1.43
A <sub>4</sub> / %	-	-	-	-0.1 ± 0.3	-	-	-	1.3 ± 1.0
φ <sub>4</sub> / hr	-	-	-	1.04 ± 1.68	-	-	-	-0.85 ± 0.97
A <sub>peak-to-peak</sub> / %	19.3	19.3	18.9	18.9	22.0	24.0	25.1	23.9
RSS	0.149	0.147	0.146	0.146	2.02	1.91	1.89	1.86
p(AIC)	5	7	9	11	5	7	9	11
AIC	-2020.3	-2021	-2019.1	-2015.9	-973.19	-992.25	-992.03	-995.42

Trial 2 (09202019, Fig. S35b, also seen in Fig. 5 and S37)

q	B <sub>+</sub>				10 × B <sub>-</sub>			
	1	2	3	4	1	2	3	4
C / %	24.3 ± 0.2	24.3 ± 0.2	24.3 ± 0.2	24.3 ± 0.2	36.8 ± 0.6	36.9 ± 0.6	36.9 ± 0.6	36.9 ± 0.6
T / hr	18.83 ± 0.13	18.84 ± 0.12	18.84 ± 0.12	18.85 ± 0.12	18.79 ± 0.37	18.81 ± 0.32	18.77 ± 0.31	18.76 ± 0.30
A <sub>1</sub> / %	-8.9 ± 0.3	-8.9 ± 0.3	-8.9 ± 0.3	-8.9 ± 0.3	8.9 ± 0.9	9.0 ± 0.8	9.1 ± 0.8	9.1 ± 0.8
φ <sub>1</sub> / hr	3.21 ± 0.31	3.17 ± 0.31	3.17 ± 0.31	3.15 ± 0.31	2.93 ± 0.93	2.76 ± 0.82	2.87 ± 0.81	2.90 ± 0.79
A <sub>2</sub> / %	-	-0.3 ± 0.3	-0.3 ± 0.3	-0.3 ± 0.3	-	3.1 ± 0.8	3.0 ± 0.8	3.0 ± 0.8
φ <sub>2</sub> / hr	-	-11.63 ± 1.54	-11.46 ± 1.47	-11.50 ± 1.46	-	0.59 ± 0.94	0.72 ± 0.91	0.75 ± 0.89
A <sub>3</sub> / %	-	-	-0.3 ± 0.3	-0.3 ± 0.3	-	-	-0.8 ± 0.8	-0.7 ± 0.8
φ <sub>3</sub> / hr	-	-	0.28 ± 1.00	0.25 ± 1.07	-	-	-0.09 ± 1.30	-0.07 ± 1.37
A <sub>4</sub> / %	-	-	-	0.2 ± 0.3	-	-	-	0.6 ± 0.8
φ <sub>4</sub> / hr	-	-	-	0.71 ± 1.29	-	-	-	0.53 ± 1.16
A <sub>peak-to-peak</sub> / %	17.8	17.7	17.1	17.2	17.8	21	21.7	21.7
RSS	0.17	0.168	0.166	0.166	1.52	1.34	1.32	1.32
p(AIC)	5	7	9	11	5	7	9	11
AIC	-1966.6	-1966.7	-1967	-1964.5	-1087.4	-1134.9	-1134.7	-1133.2

Trial 3 (10242019, Figure S35c)

q	B <sub>+</sub>				10 × B <sub>-</sub>			
	1	2	3	4	1	2	3	4
C / %	19.4 ± 0.3	19.4 ± 0.3	19.4 ± 0.3	19.4 ± 0.3	38.1 ± 0.7	38.0 ± 0.7	38.0 ± 0.7	38.1 ± 0.7
T / hr	20.37 ± 0.16	20.43 ± 0.16	20.40 ± 0.15	20.41 ± 0.15	19.62 ± 0.47	19.98 ± 0.42	19.95 ± 0.41	19.91 ± 0.41
A <sub>1</sub> / %	-10.3 ± 0.4	-10.4 ± 0.4	-10.4 ± 0.4	-10.4 ± 0.4	8.9 ± 1.0	9.4 ± 0.9	9.4 ± 0.9	9.4 ± 0.9
φ <sub>1</sub> / hr	2.41 ± 0.37	2.26 ± 0.37	2.33 ± 0.37	2.31 ± 0.37	2.96 ± 1.13	2.22 ± 1.00	2.28 ± 0.99	2.38 ± 0.99
A <sub>2</sub> / %	-	-0.5 ± 0.4	-0.5 ± 0.4	-0.5 ± 0.4	-	3.6 ± 0.9	3.6 ± 0.9	3.6 ± 0.9
φ <sub>2</sub> / hr	-	-2.60 ± 1.35	-2.54 ± 1.23	-2.56 ± 1.20	-	0.01 ± 1.11	0.09 ± 1.11	0.20 ± 1.11
A <sub>3</sub> / %	-	-	0.5 ± 0.4	0.5 ± 0.4	-	-	-0.3 ± 0.9	-0.3 ± 0.9
φ <sub>3</sub> / hr	-	-	0.91 ± 0.83	0.86 ± 0.87	-	-	-1.09 ± 3.98	-0.83 ± 3.44
A <sub>4</sub> / %	-	-	-	-0.2 ± 0.4	-	-	-	-0.5 ± 0.9
φ <sub>4</sub> / hr	-	-	-	0.40 ± 1.58	-	-	-	-0.08 ± 1.85
A <sub>peak-to-peak</sub> / %	20.7	20.7	20.7	20.7	17.8	22.6	22.7	23
RSS	0.27	0.267	0.262	0.261	1.92	1.66	1.66	1.66
p(AIC)	5	7	9	11	5	7	9	11
AIC	-1780	-1781.4	-1785.2	-1782.3	-994.64	-1047.9	-1044.2	-1041.2

#### 4 References for Supporting Information

- (1) Chow, G. K.; Chavan, A. G.; Heisler, J. C.; Chang, Y.-G.; LiWang, A.; Britt, R. D. Monitoring Protein–Protein Interactions in the Cyanobacterial Circadian Clock in Real Time via Electron Paramagnetic Resonance Spectroscopy. *Biochemistry* **2020**, *59* (26), 2387-2400. DOI: 10.1021/acs.biochem.0c00279.
- (2) Freed, J. H.; Bruno, G. V.; Polnaszek, C. F. Electron spin resonance line shapes and saturation in the slow motional region. *J. Phys. Chem.* **1971**, *75* (22), 3385-3399. DOI: 10.1021/j100691a001.
- (3) Cohon, J. L. Multiobjective Programming and Planning. In *Mathematics in Science and Engineering*, Academic Press: New York, 1978; Vol. 140.
- (4) Hansen, P. C.; O’Leary, D. P. The Use of the L-Curve in the Regularization of Discrete Ill-Posed Problems. *SIAM J. Sci. Comput.* **1993**, *14* (6), 1487-1503. DOI: 10.1137/0914086 (accessed 2020/08/07).
- (5) Cohan, B. E.; Hewitt, J. N.; de Weck, O. The Design of Radio Telescope Array Configurations using Multiobjective Optimization: Imaging Performance versus Cable Length. *Astrophys. J. Suppl. Ser.* **2004**, *154* (2), 705-719. DOI: 10.1086/422356.
- (6) Welkie, D. G.; Rubin, B. E.; Chang, Y. G.; Diamond, S.; Rifkin, S. A.; LiWang, A.; Golden, S. S. Genome-wide fitness assessment during diurnal growth reveals an expanded role of the cyanobacterial circadian clock protein KaiA. *Proc. Natl. Acad. Sci. USA* **2018**, *115* (30), E7174-E7183. DOI: 10.1073/pnas.1802940115.
- (7) Koda, S. I.; Saito, S. An alternative interpretation of the slow KaiB-KaiC binding of the cyanobacterial clock proteins. *Sci. Rep.* **2020**, *10* (1), 10439. DOI: 10.1038/s41598-020-67298-7.
- (8) Chang, Y. G.; Kuo, N. W.; Tseng, R.; LiWang, A. Flexibility of the C-terminal, or CII, ring of KaiC governs the rhythm of the circadian clock of cyanobacteria. *Proc. Natl. Acad. Sci. USA* **2011**, *108* (35), 14431-14436. DOI: 10.1073/pnas.1104221108.
- (9) Chang, Y. G.; Tseng, R.; Kuo, N. W.; LiWang, A. Rhythmic ring-ring stacking drives the circadian oscillator clockwise. *Proc. Natl. Acad. Sci. USA*. **2012**, *109* (42), 16847-16851. DOI: 10.1073/pnas.1211508109.
- (10) Heisler, J.; Chavan, A.; Chang, Y. G.; LiWang, A. Real-Time In Vitro Fluorescence Anisotropy of the Cyanobacterial Circadian Clock. *Methods Protoc.* **2019**, *2* (2), 42. DOI: <https://doi.org/10.3390/mps2020042>.
- (11) Delaglio, F.; Grzesiek, S.; Vuister, G. W.; Zhu, G.; Pfeifer, J.; Bax, A. NMRPipe: a multidimensional spectral processing system based on UNIX pipes. *J. Biomol. NMR* **1995**, *6* (3), 277-293. DOI: 10.1007/BF00197809.
- (12) Czoch, R. Quantitative EPR — Sensitivity to experimental conditions and optimal setting of recording parameters. *Appl. Magn. Reson.* **1996**, *10* (1), 293-317. DOI: 10.1007/BF03163115.
- (13) Polimeno, A.; Freed, J. H. Slow Motional ESR in Complex Fluids: The Slowly Relaxing Local Structure Model of Solvent Cage Effects. *J. Phys. Chem.* **1995**, *99* (27), 10995-11006. DOI: 10.1021/j100027a047.
- (14) Stoll, S.; Schweiger, A. EasySpin, a comprehensive software package for spectral simulation and analysis in EPR. *J. Magn. Res.* **2006**, *178* (1), 42-55, Article. DOI: 10.1016/j.jmr.2005.08.013.

- (15) Belge, M.; Kilmer, M. E.; Miller, E. L. Efficient determination of multiple regularization parameters in a generalized L-curve framework. *Inverse Probl.* **2002**, *18* (4), 1161–1183.
- (16) Terauchi, K.; Kitayama, Y.; Nishiwaki, T.; Miwa, K.; Murayama, Y.; Oyama, T.; Kondo, T. ATPase activity of KaiC determines the basic timing for circadian clock of cyanobacteria. *Proc. Natl. Acad. Sci. USA* **2007**, *104* (41), 16377-16381. DOI: 10.1073/pnas.0706292104.